Astrophysical Collisionless Shock modeled with Large-scale Laser-produced Plasmas

(大型レーザーによる宇宙無衝突衝撃波の模擬実験)

Taichi Morita

Department of Earth and Space Science

Graduate School of Science

Osaka University

Toyonaka, Osaka 560-0043, Japan

January, 2011

Abstract

The aim of the research is to reproduce collisionless shocks observed in supernova remnants and to find the physics of collisionless shocks. This also aims at the physics of particle accelerations relating to the origin of cosmic rays. In the present thesis, I would like to show a part of the whole story by mainly focusing on the electrostatic (ES) shock formation in counter-streaming plasmas [T. N. Kato and H. Takabe, Phys. Plasmas **17**, 032114 (2010)] produced by a high-power laser irradiation without external magnetic field.

Nearly four times density jump observed in the experiment shows a high Mach-number shock (chapter 3). This large density jump is attributed to the compression of the downstream plasma by momentum transfer by ion reflection of the upstream plasma. Particle-in-cell (PIC) simulation shows the production of a collisionless high Mach-number ES shock with counter-streaming interaction of two plasma slabs with different temperatures and densities, as pointed out by Sorasio *et al*. [Phys. Rev. Lett. **96**, 045005 (2006)]. It is speculated that the shock discontinuity is balanced with the momentum of incoming and reflected ions and the predominant pressure of the electrons in the downstream with PIC simulation. We also observed collisionless shocks generated by a collimated plasma jet (chapter 5). The jet formation has been investigated by Kuramitsu *et al*. in the same experimental setup [Astrophysical Journal Letters, **707**, L137 (2009)]. The shock formation is confirmed by a sudden emission change at the shock discontinuity in the time evolution of self-emission measurements. It is found that the shock is created due to counter-streaming collisionless interactions and no shock is created without a counter flow. This shock affects plasma expansion and is essential for plasma jet collimation. The plasma temperatures and densities at the shock surface are evaluated by the emission from plasmas. Plasma temperatures were measured with optical pyrometer systems which is based on the self-emission measurements: Gated Optical Imager (GOI) and Streaked Optical Pyrometer (SOP). In both detectors, the intensity of the self-emission from laser-produced plasmas at the

wave length of 450 nm was measured. They were calibrated to determine the brightness temperatures and electron temperatures with different methods and both results agreed each other within 30 % (chapter 4). Using the jump condition in densities and temperatures at the shock and evaluating the emission intensity from bremsstrahlung radiation, we obtain the plasma temperatures and densities at the upstream and downstream regions of the shock.

Contents

Chapter 1

Introduction

In this chapter, we show the motivation of the research on collisionless shock formation using high-power laser systems. First, we explain the particle accelerations and their relation to collisionless shocks in the universe. The physics of particle accelrfation is not studied experimentally in this thesis but the author's final target is to clarify such physcs experimentally. Therefore, we need to keep in mind such physics during the present research. Second, we show possibilities of collisionless shock formation without magnetic field, and the experiment in laboratories using high-power laser systems. Third, we have an overview of previous experiments in laboratories. Finally, we show the goal of this research and future work.

1.1 Particle acceleration in the universe

High energy nuclei (cosmic rays) such as proton, helium, carbon, and iron are observed by balloons[1, 2] and satellites[3, 4], and on the earth[5, 6, 7]. The reason why cosmic rays are accelerated up to high energy is still a major unresolved probrem in astrophysics.

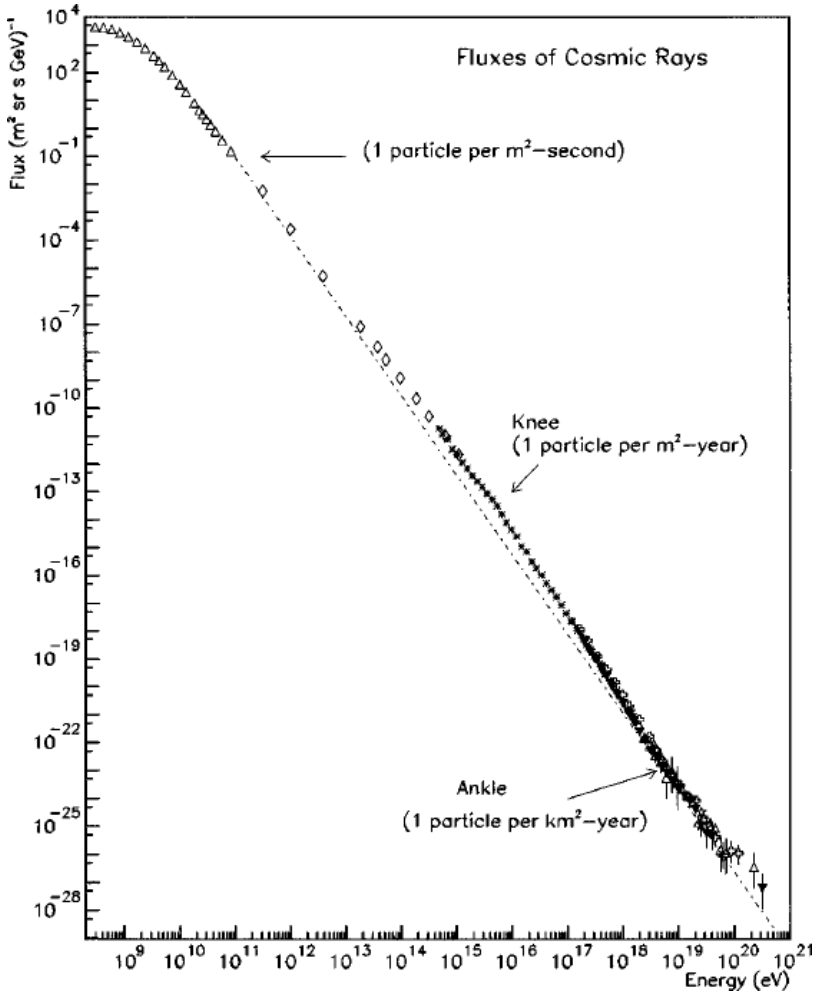

Figure 1.1: The energy spectrum of cosmic rays greater than 100 MeV. [8]

1.1.1 Observations of accelerated particles

Figure 1.1 shows the energy spectrum of cosmic rays of all kinds of nuclei[8]. The flux of high energy particles does not depend on the direction and time, and it can be expressed as a function of only energy and the kinds of nuclei. The energy spectrum is expressed with a simple power functions as $dN/dE = E^{-\alpha}$. As shown in Fig. 1.1, the power α changes at

$E \sim 5 \times 10^{15}$ eV $= E_{\rm knee}$ and $E \sim 6 \times 10^{19}$ eV $= E_{\rm ankle}$.

$$\frac{dN}{dE} \propto \begin{cases} E^{-2.5\text{–}2.7} & (E < E_{\rm knee}) \\ E^{-3.1} & (E_{\rm knee} < E < E_{\rm ankle}) \end{cases} \tag{1.1}$$

In the energy range below $E_{\rm knee}$, primary cosmic rays are detected by balloons and satellites. The origins of cosmic rays are thought to be shock waves in our galaxy because the Larmor radius in magnetic fields ($B \sim$ a few μG) in interstellar spaces is less than $\sim$1 pc which is much smaller than typical distance between the earth and supernova remnants (SNRs) ($\sim$ kpc) and cosmic rays can not travel to outside of our galaxy. This Lamor radius $\sim$1 pc is comparable to the typical size of SNRs, and this means that the energy $E_{\rm knee}$ is nearly the maximum for acceleration at SNRs in our galaxy. At the energy above $E_{\rm knee}$, the flux suddenly decreases. This is probably due to the effects of escaped cosmic rays from the galaxy. In the energy range larger than $E_{\rm ankle}$, the Larmor radius is comparable to or larger than the scale of the galaxy, and cosmic rays can not be confined in the galaxy any more. This indicates that such extremely high-energy cosmic rays come from the external objects. However, such high-energy cosmic rays reduce their energy due to interactions with cosmic background radiation[9, 10] ($p+\gamma \to p+\pi_0$ and $p+\gamma \to n+\pi^+$). Therefore, their origins should be located within $\sim$50 Mpc from our galaxy. Cosmic rays which have energies of around $E_{\rm ankle}$ have been observed by detecting cascade particles caused by a primary cosmic ray with the Haverah Park surface array in England[5] and AGASA in Japan[6], and by detecting fluorescence photons produced by shower particles with the Fly's Eye fluorescence detector in Utah, USA[7].

1.1.2 The origin of Cosmic rays

Though cosmic rays were discovered about 100 years ago, the origin of cosmic rays has been a longstanding problem in astrophysics. As we described in the previous section,

the acceleration mechanisms for cosmic rays whose energies are below $E_{\rm knee}$ is thought to be shock waves in SNRs. This idea was first proposed by E. Fermi (section A.4.1). His idea is based on the particle acceleration by scattering by magnetized clouds. However, multiple scattering by magnetic field in SNR shock is more efficient mechanism[11] (section A.4.2). Recently, alternative mechanisms for particle acceleration have been discussed: direct acceleration due to the energy release by magnetic reconnection[12] and the electron shock surfing process. Energetic particles are often observed in magnetotail by satellite observations[3, 4], and it suggests these energetic particles are related to magnetic reconnection. The possible causes for acceleration of extremely high-energy particles ($E > E_{\rm ankle}$) are relativistic shocks produced at gamma-ray bursts (GRBs), active galactic nuclei (AGN), and cluster of galaxies. In many cases, collisionless shocks are essential for particle acceleration.

1.2 Collisionless shock formation in the universe

In this section, we show some examples of collisionless shocks in the universe which play important roles in particle acceleration, and especially explain collisionless shocks produced by SNRs due to the interaction between exploding supernova (SN) and interstellar medium (ISM).

1.2.1 Observations

In interplanetary shocks, energetic particles which have energy of 1 keV to 1 MeV are often observed by satellites[13, 14]. They are accelerated at collisionless shocks. Figures 1.2(a) and 1.2(b) show the counts of accelerated ions and phase velocity densities for accelerated electrons, respectively[15]. These results clearly suggest nonthermal particle accelerations at the interplanetary collisionless shocks.

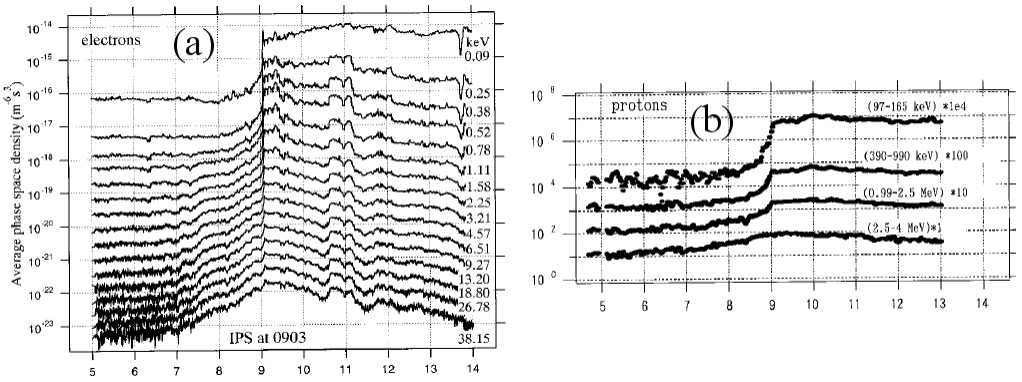

Figure 1.2: (a) Average phase space densities of electrons which have energy less than $\sim$40 keV and (b) omnidirectional counts for ions which have energy less than 4 MeV[15].

Collisionless shocks in SNRs are clearly observed with X-ray by satellites. In the subsection 1.2.3, we will show the clear X-ray images by the satellites XMMS-Newton and Chandra. Observed shock structures in SNRs are thin and such filamentary structures show the collisionless shock generation.

GRBs are flashes of high-energy gamma-rays which last only for a few minutes and arrive about once per a day at random times from different directions in the sky. They were first detected by a Vela satellite[16] in 1967. The sources of GRBs are not known well, however they are related to some relativistic explosions which is result from collapses of neutron stars or so-called hypernovae. If their source expand with relativistic velocities, relativistic shocks are produced in ISM. Astrophysical jets observed at such as AGNs and protostars also generate collisionless shocks in ISM. Their velocity is relativistic and they might be sources of high-energy cosmic rays.

1.2.2 Supernova explosion

SN is one of the most brilliant phenomena in the universe. In the last 2000 years, SNe which were bright enough to be seen from the Earth have occurred at least 7 times[17]. According to records in China, Egypt, Switzerland, and Japan, a brightest star appeared in

the constellation Lupus, on 1 May 1006, which can be seen with the naked eyes (SN1006). On 23 February 1987, a SN has appeared in the Large Magellanic Cloud (SN1987A).

There are basically two types of SNe known as type Ia and type II[18]. SNe are classified with their emission spectra, for example, SN1006 and SN1987A are classified as type Ia and type II, respectively. In type Ia SNe, there are remarkable lacks of hydrogen in their spectra. The emission intensity rises quickly in $\sim$2 weeks and decline exponentially with a time scale of $\sim$55 days. In type II SNe, the emission increases slowly, and they keep the maximum emission intensity longer than type Ia. These differences come from the mechanisms for SNe and their progenitors.

In both types, the explosion can be caused because of the energy release at the end of the life of a star. When a white dwarf, in which the mass is as much as that of the sun and the size is as much as that of the Earth, is in binary system, the mass can be transferred from the other star. When the mass becomes larger than the Chandrasekhar limit $1.44M_{\odot}$, where $M_{\odot}$ is the mass of the sun, the gravity overcomes the electron degeneracy pressure inside the white dwarf to raise collapse. In this sequence, a huge energy $\sim 10^{52}$ erg is released in nuclear fusion reactions. This explains the quick increase of the emission energy in type Ia.

On the other hand, if the progenitor of SN has the mass larger than $\sim 10M_{\odot}$, the evolution process is different. At the early stage of the development, hydrogen is fused into helium in the core of the star. When the pressure and temperature are high because of the gravity, helium is fused to carbon and oxygen. And finally, the core becomes iron and it is surrounded by lighter materials. Iron is stable and no more fusion can occur in the core. The core is compressed by gravitational force and the temperature increases to decompose the irons into lighter nuclei, resulting in the pressure decrease and the reactions $p+e \rightarrow n+\nu_e$ occur. As a result, the core collapses by gravitational force to produce a neutron star. The neutrinos are detected on the Earth with the Kamiokande[19] at Kamioka, Japan, the

Irvine-Michigan-Brookhaven (IMB)[20] at Cleveland, USA , and the Baksan[21] in Russia at the same time.

1.2.3 Supernova remnants

There are three phases in explosion process of SNR: (1) free expansion phase, (2) Sedov-Taylor phase, and (3) radiative phase. After the collapse of a star, the ejected materials expand and sweep up the surrounding materials. The mass of swept-up materials is negligible compared to the ejecta, and the ejecta expands with a constant velocity: free expansion phase. After that, the mass of the swept-up materials become larger than that of the ejecta: Sedov-Taylor phase. The rapidly moving ejecta makes two shock waves in the ISM (forward shock) and in the ejected gas (reverse shock). The boundary between the downstream regions of two shocks is called contact discontinuity. First both shocks travel outward with different velocities and, after the swept-up materials exceed the original ejecta, the reverse shock begins to travel inward[22]. Figure 1.3 shows the schematic view of a SNR in the Sedov-Taylor phase. forward and reverse shocks are generated in ISM and expanding ejecta, respectively. ISM is thermalized at the downstream region shown as "swept-up ISM" in Fig. 1.3, and expanding ejecta is also thermalized at the downstream region of the reverse shock. Two regions which have different densities have separated by a contact discontinuity.

Shocks have been observed with radio and X-ray observations[24]. These observation have shown a clear evidence that particles are accelerated to relativistic energies by the first order Fermi acceleration (subsection A.4.2). In SNRs, thermal emission from hot gas thermarized by forward shocks has been observed. And there are also nonthermal X-ray emissions by the synchrotron radiation of high-energy electrons. The synchrotron

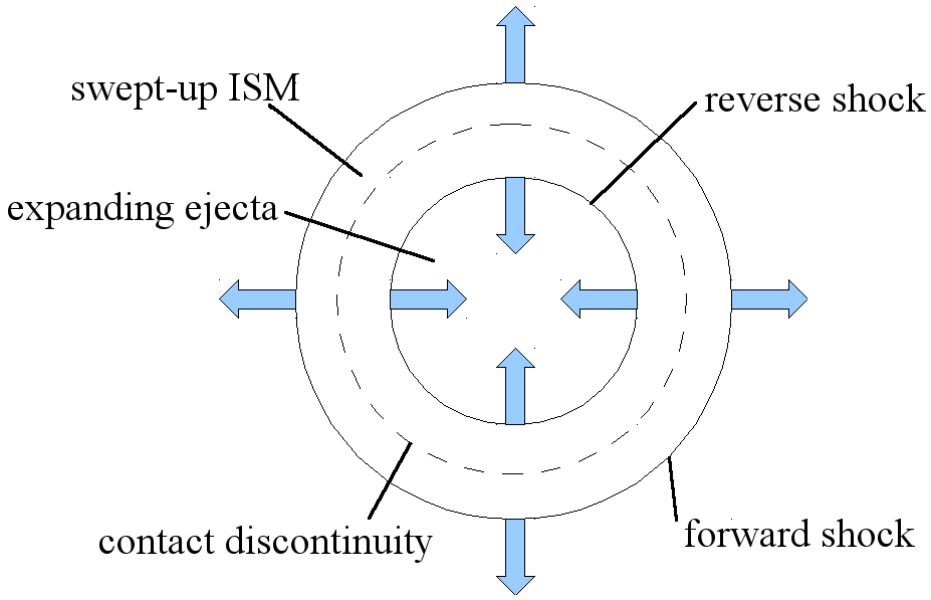

Figure 1.3: The schematic view of a SNR in the Sedov-Taylor phase. Forward and reverse shocks are generated in ISM and expanding ejecta, respectively. Two downstream regions of both shocks are separated by a contact discontinuity.

frequency is written as [25]

$$\omega_c = \gamma^2 \frac{eB}{m_e c} = \left(\frac{E}{m_e c^2}\right)^2 \frac{eB}{m_e c}, \tag{1.2}$$

where γ is the Lorentz factor of the electron, E is the electron energy, and B is the magnetic field. A typical photon energy detected in SNRs is $\hbar\omega_c \sim 10$ keV, which corresponds to the frequency of 2.4×10^{19} Hz. Assuming the magnetic field $B \sim 10^{-5}$ G, the electron energy is $E \sim 500$ TeV. This means electrons are accelerated at the shocks in SNRs up to high energies. There are also the circumstantial evidence of ion acceleration at the shock with X-ray observation[26, 27]. Shock waves observed in SNRs are collisionless shocks because the thicknesses (W) of the shocks are much smaller than the collision mean-free-path (λ), for example, $W \sim 0.04$ pc[23] and $\lambda \sim 13$ pc for protons in SN1006. Figure 1.5 shows the profiles of the emission intensity in different energy ranges. Filamentary structures are observed at the edges of SNR emissions and their transition widths are much

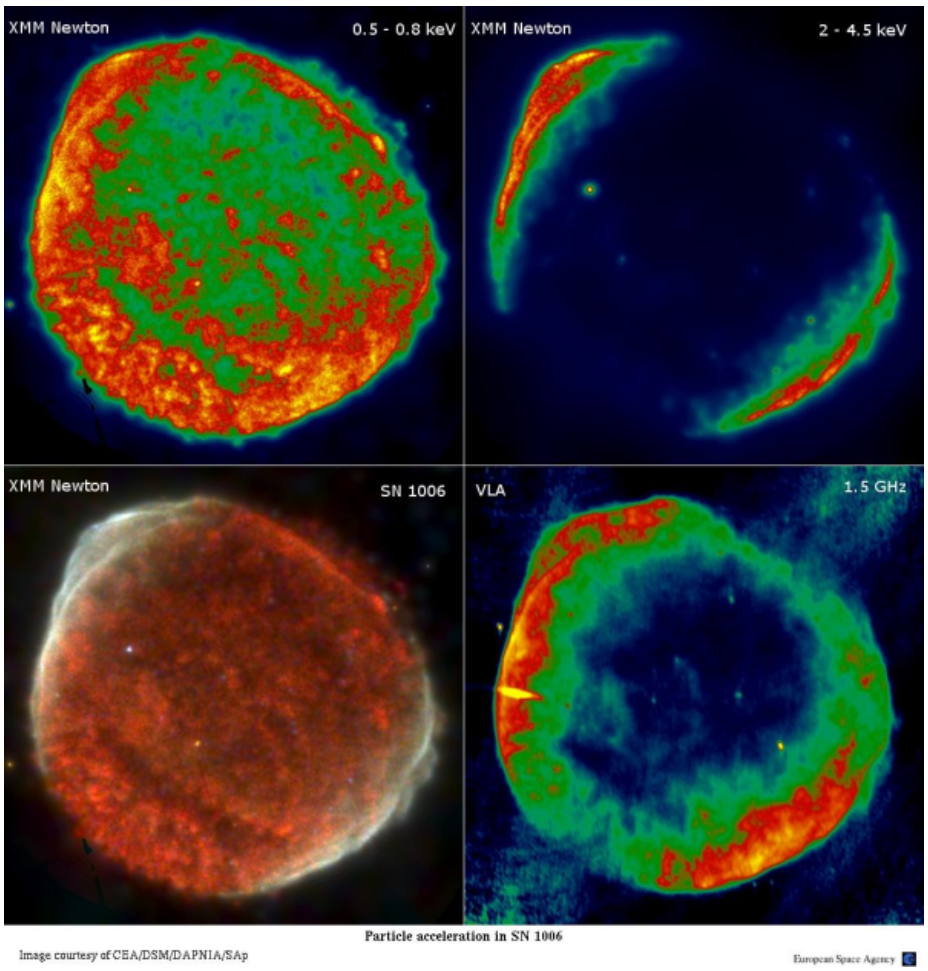

Figure 1.4: X-ray images of the SNR (SN1006) by the satellite XMM-Newton in various energy ranges. [Image courtesy of CEA/DSM/DAPNIA/SAp]

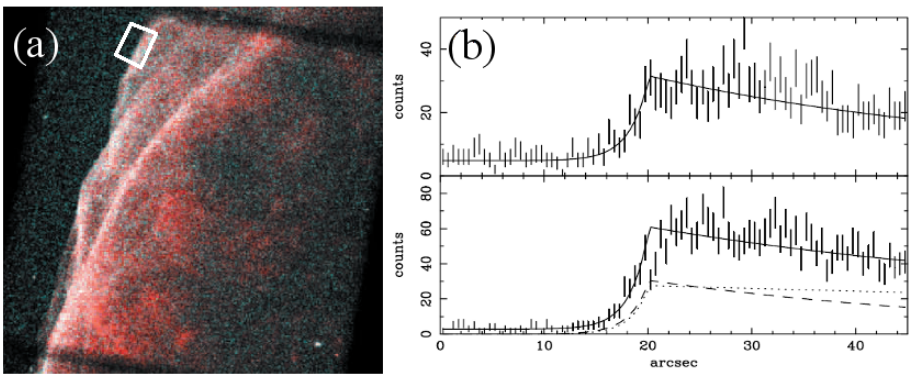

Figure 1.5: (a) X-ray image of SN1006 observed by the satellite Chandra. (b) Intensity profiles at the region shown with white square in (a) in hard (2.0–10.0 keV: upper panel) and soft (0.4–0.8 keV: lower panel) bands. [23]

smaller than ion-ion mean-free-path.

In ISM in the universe, there are magnetic field with the strength of a few μG and, in the magnetic field, shock solutions can be obtained due to dispersion relations as discussed in the subsection A.2.2. In this case, Alfvén speed v_A and Alfvén Mach-number $M_A = v_0/v_A$ should be used in stead of the sound speed c_s and Mach-number $M = v_0/c_s$, respectively. As a result, the transition width of shock wave is comparable to electron inertial length $\lambda_{\rm e} = c/\omega_{\rm pe}$ not to the Debye length $\lambda_{\rm D} = \sqrt{\epsilon_0 k_{\rm B} T_{\rm e}/n_{\rm e} e^2}$, where $\omega_{\rm pe} = \sqrt{n_{\rm e} e^2/m_{\rm e}\epsilon_0}$ is the electron plasma frequency. As just described above, the magnetic field plays an important role in collisionless shock generation in the universe.

1.3 Possibility of collisionless shocks without magnetic field

As shown in the previous section, collisionless shocks are generated in an external background magnetic field. However, recent researches with Particle-in-cell (PIC) simulations have shown the possibility of shock generations due to Weibel instability without an external magnetic field or with a weak magnetic field[28, 29].

1.3.1 Weibel-mediated shocks with Particle-in-cell simulation

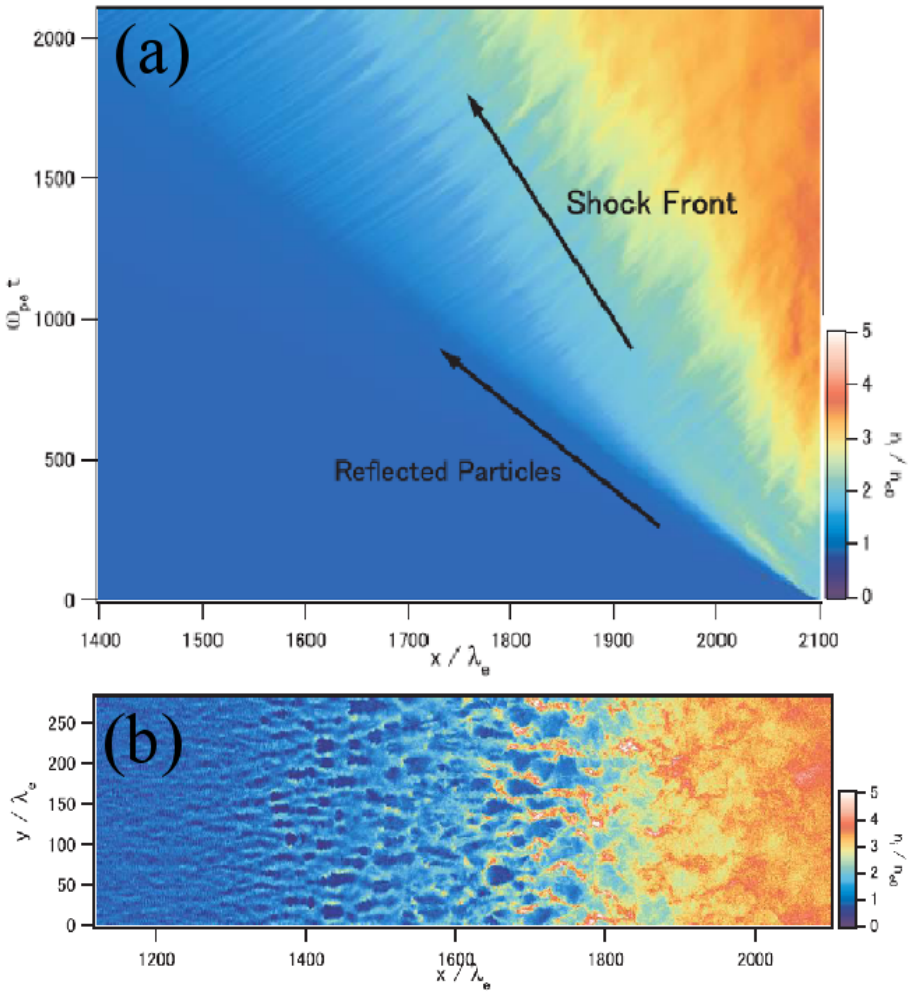

Figure 1.6: (a) The time evolution of the ion density for the bulk velocity $V = 0.45c$ and (b) the ion density at $\omega_{\rm pe}t = 2100$. Weibel-mediated shock was formed with PIC simulation in an unmagnetized electron-ion plasma. [30]

Recently it has been pointed out that collisionless shocks can be produced without an external magnetic field; it is a universal phenomenon that the shocks are produced when a high-velocity flow travels over any space in the universe filled with a rarefied gas[31]. Figure 1.6(a) shows Weibel-mediated collisionless shock propagation and Fig. 1.6(b) shows the ion density in the shock transition region by particle-in-cell (PIC) simulation[32, 30]. Weibel instability can be driven in counter-streaming plasmas and it generate strong mag-

netic field[33]. In the PIC simulations[30], the Weibel instabilities develop in the interacting region between counter-streaming flows and they can be seen as filamentary structures as shown in Figure 1.6(b).

The shock width W is about 100 times the ion inertial length, $W \sim 100\lambda_{\rm i} = 100c/\omega_{\rm pi}$, where $\omega_{\rm pi} = \sqrt{n_{\rm i}(Ze)^2/m_{\rm i}\epsilon_0}$ is the ion plasma frequency, and is independent of shock velocity. The ion inertial length is the distance an ion has to travel to trigger or experience collective plasma effects.

1.3.2 Electrostatic shocks and instabilities

In early stage of "Weibel-mediated" shock formation, an electrostatic (ES) shock can be generated and destroyed by ion–ion instability which propagates obliquely to the shock surface. Figure 1.7 shows the time evolution of electric field calculated by PIC simulation[34]. ES shock is generated and destroyed due to ES ion-ion instabilities in front of the shock. After the ES shock is destroyed, Weble instability gradually grows and a shock is generated. It is likely to say that the ES shock can be generated in the earty stage of supernova explosion and in later time, shocks are generated due to Weibel instability.

1.4 Possibility of Laser experiment

It is impossible to measure the physical quantities in the astrophysical high-energy phenomena, such as electric or magnetic fields, for example, in supernova remnants (SNRs) and astrophysical jets, however, laboratory experiments can be alternative ways to investigate the astrophysical phenomena. Laboratory experiments can be scaled to the astrophysical phenomena considering the dimensionless parameters[35].

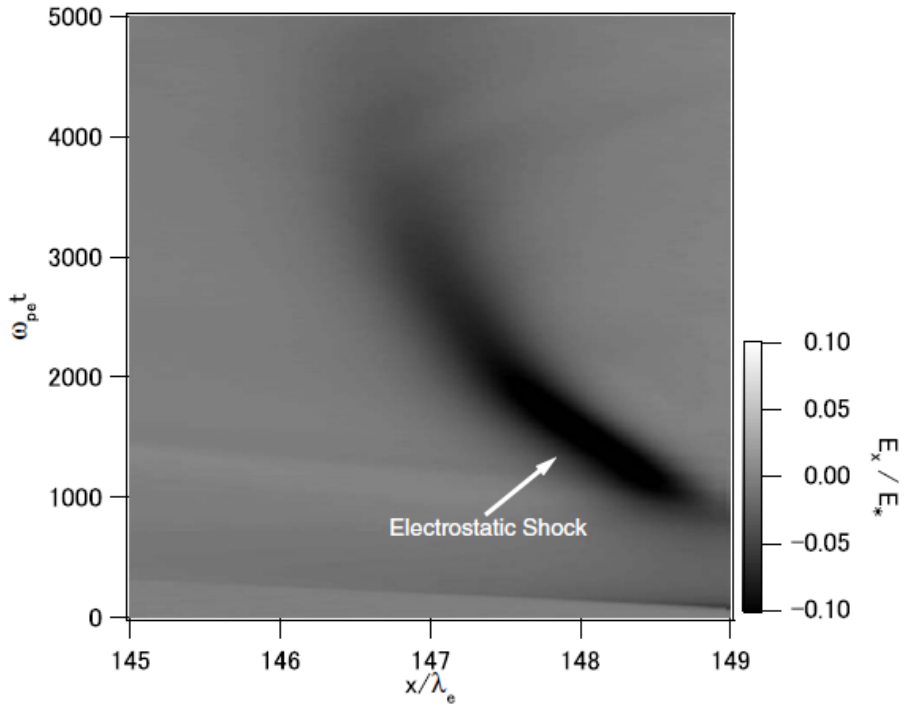

Figure 1.7: The time evolution of electric field calculated by PIC simulation. [34]

1.4.1 Collisionality in counter-streaming plasmas

In laser experiments, high-velocity counter-streaming plasmas are required to obtain collisionless interaction between two plasmas. The ion-ion mean-free-path in thermal equilibrium plasmas is ordinary expressed with the electron temperature T_{e},

$$\lambda_{\mathrm{ii}} = \frac{18\pi\epsilon_0^2 (k_{\mathrm{B}} T_{\mathrm{e}})^2}{n_{\mathrm{i}} Z_1^2 Z_2^2 e^4 \ln\Lambda}. \tag{1.3}$$

However, in counter-stream plasmas the ion-ion collision mean-free-path is estimated by equation (A.47) using relative velocity of counter-streaming plasmas u_0. Using equation (A.47), $\lambda_{\mathrm{ii}} \simeq 1.6$ mm for $n_{\mathrm{e}} = 1 \times 10^{21}$ cm^{-3}, and $\lambda_{\mathrm{ii}} \simeq 14$ mm for $n_{\mathrm{e}} = 1 \times 10^{20}$ cm^{-3} assuming the electron temperature $T_{\mathrm{e}} = 100$ eV and plasma relative velocity $u_0 = 2000$ km/s.

1.4.2 Scaling law from PIC

Possibility of Weibel shock with laser-produced plasmas

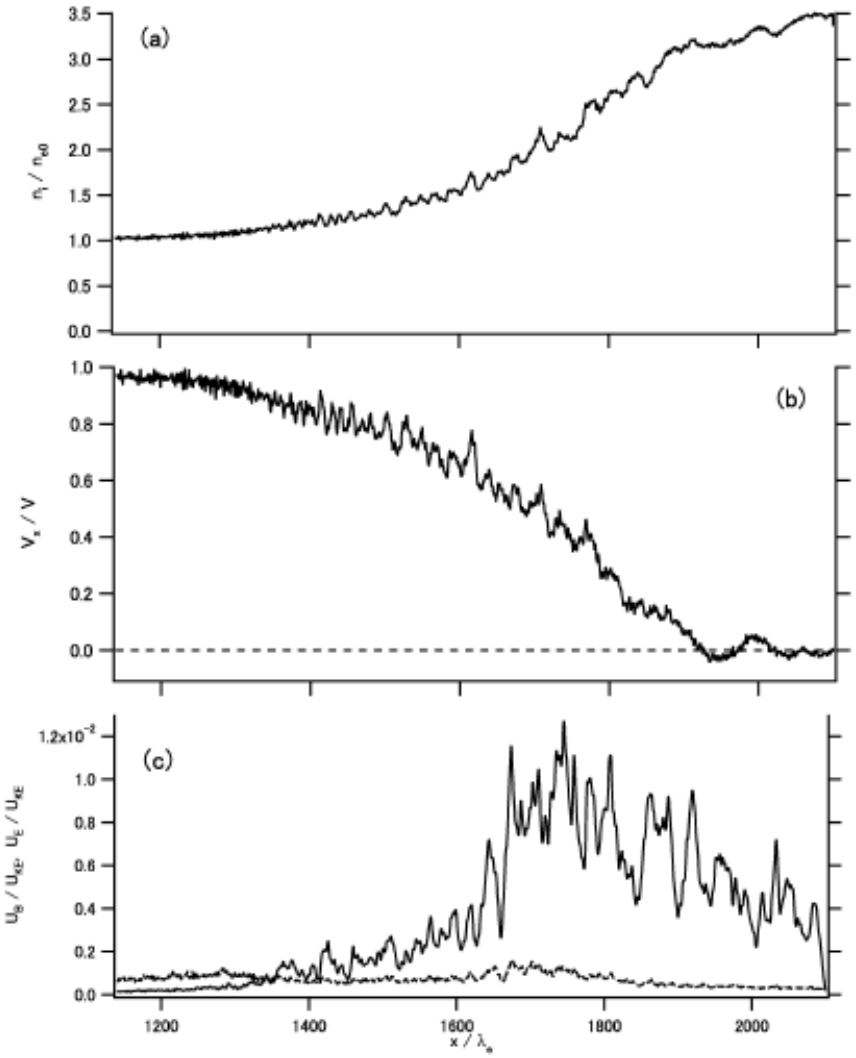

Figure 1.8: Profiles of (a) ion number density, (b) mean velocity in x direction, and (c) the energy of magnetic (solid line) and electric (dotted line) fields. [30]

PIC simulations were preformed with different upstream bulk velocities v and ion to electron mass ratios $m_{\rm i}/m_{\rm e}$. Figures 1.8(a), 1.8(b), and 1.8(c) show the profiles of ion density, mean velocity, and magnetic and electric field energy densities, respectively. The

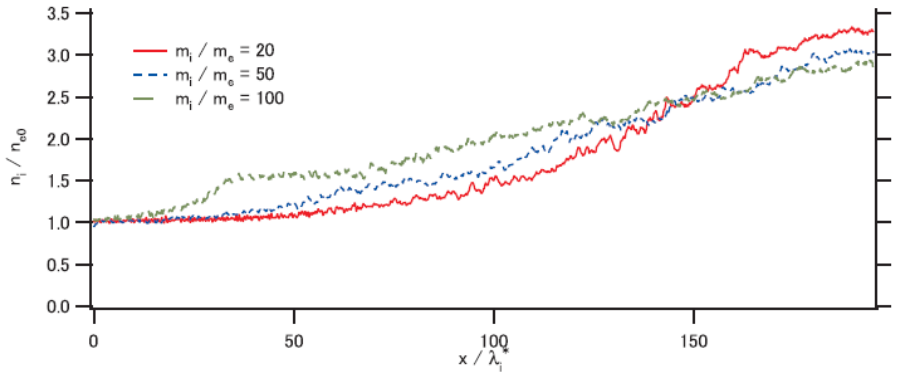

Figure 1.9: Profiles of ion densities for different mass ratios. [30]

width of the shock transition region W is $W \sim 100c/\omega_{\rm pi}$. The energy densities of magnetic fields are typically 1–2% of upstream bulk kinetic energy densities and independent of the velocities. In Figure 1.9, the profiles of ion densities for different mass ratios ($m_{\rm i}/m_{\rm e}$ = 20, 50, and 100) are shown. The widths of the transition regions are also $W \sim 100c/\omega_{\rm pi}$ in all cases, and this suggests that the shock width W is independent of the mass ratio. To observe Weibel-mediated shock in laser-produced plasmas, a small shock width is better to diagnose. Using above formula, in laser experiments, W is estimated as $W = 10$ mm for $n_{\rm e} = 1 \times 10^{19}$ cm^{-3}, 3 mm for $n_{\rm e} = 1 \times 10^{20}$ cm^{-3}, and 1 mm for $n_{\rm e} = 1 \times 10^{21}$ cm^{-3}.

From Fig. 1.6(a), shock is formed and propagates after $\omega_{\rm pe}t \sim 500$ for the flow velocity $v = 0.45c$. From the results of PIC simulations with mass ratios $m_{\rm i}/m_{\rm e} = 20$ and 100, and different flow velocities $v/c = 0.9$, 0.45, 0.2 and 0.1, we obtained a scaling law for shock formation time as $t \propto m_{\rm i}/m_{\rm e}$ for the mass ratio and $t \propto v^{-1}$ for the flow velocity dependence. Therefore, we obtain the following formula for real mass ratio

$$\omega_{\rm pe}t \sim 1700 \times \left(\frac{1836}{20}\right)\left(\frac{A}{Z}\right)\left(\frac{0.1c}{v}\right) \tag{1.4}$$

$$= 1.56 \times 10^4 \times \left(\frac{A}{Z}\right)\left(\frac{c}{v}\right), \tag{1.5}$$

using the shock formation time $\omega_{\rm pe}t = 1700$ for $m_{\rm i}/m_{\rm e} = 20$ and $v/c = 0.1$, where Z

is the degree of ionization and A is the mass number. In laser experiments, the shock formation time is evaluated as 4.9 ns for $n_{\rm e} = 10^{21}$ cm^{-3} and 15 ns for $n_{\rm e} = 10^{20}$ cm^{-3}, assuming $Z = 3.5$, $A = 6.5$, and $v = 1000$ km/s (relative velocity: 2000 km/s). Therefore, considering the shock width, formation time, and collision mean-free-path, $n_{\rm e} = 1 \times 10^{20}$–$1 \times 10^{21}$ cm^{-3} and $v = 1000$ km/s (relative velocity: 2000 km/s) are roughly required for experiment of Weibel-mediated shock formation in laboratory.

Scaling for ES shock from PIC

For electrostatic shocks, shock width and formation time is much smaller than that of Weibel-mediated shock[34]. The shock width W and formation time t of ES shock can be evaluated in Ref. [34] as $W \sim c/\omega_{\rm pe}$ and $\omega_{\rm pe}t \sim 1000$, respectively. These values are compared to experimental results in the chapter 3.

1.4.3 Requirements in diagnostics

To observe shocks in counter-streaming plasmas, plasma densities and temperatures have to be observed in the upstream and downstream regions at a shock. We have performed the laser experiments using interferometry for density measurement (chapter 3 and 5), and self-emission detection from laser-produced plasmas for temperature measurement (chapter 4 and 5). Ion and electron temperatures in plasmas can be measured precisely by detecting Thomson-scattering of incident probe laser.

For the plasma velocity, we used the streaked interferometry or streaked self-emission measurement using streak cameras (chapter 5) in which the time-evolution of one-dimensional images are recorded in CCD cameras.

Moreover, electric and magnetic field strengths should be measured in shock regions. Proton beams are used as probes of electric and magnetic fields. In previous experiments, we observed radiography with protons generated due to interactions of high-intensity laser

and materials[36]. In future experiments using National Ignition Facility (NIF), we will use monoenergetic protons produced by an implosion. However, it is difficult to separate the effects of magnetic and electric fields, because protons can be deflected by both effects. Magnetic field can also be measured by observing the angle of Faraday rotation of incident probe laser. In Faraday rotation method, density and probe laser intensity should be measured precisely.

In future experiments, we will measure magnetic field strength with Faraday rotation method and will measure precise temperature with Thomson scattering of probe laser.

1.5 Mach-number in ES collisionless shocks

Collisionless shocks have been studied for many years theoretically and numerically[37, 38, 39, 40, 41, 42, 43]. In the subsection A.2.2, we simply argued the formation of ion acoustic solitons and shocks, and their solutions can be expressed using Sagdeev potential in equation (A.24). If a solition exists, the Mach-number satisfy $1 < M < 1.6$ and the shape of the potential is shown in Fig. A.2 like a potential well. If the energy dissipated in the motion of solition, the solitary solution is converted to shock solution. This effect is shown by including friction term such as Landau damping, or allowing ion reflections in front of a shock or ion trappings behind a shock. In such cases, Mach-number can be larger than the upper limit argued above $M < 1.6$. PIC simulations are suitable for such high Mach-number shocks including ion reflection or ion trapping in a shock.

In a recent paper, a new theory is proposed and it is concluded that a very strong ES shock can be generated when counter-streaming plasma flows with different temperatures and densities interact each other[31]. Figures 1.10(a) and 1.10(b) show the ES potential at the shock and the maximum Mach-number of the shock produced due to counter-streaming interaction, respectively. The maximum Mach-number is expressed as a function of the temperature ratio of right to left plasma. Apparently, very high Mach-number ES shock is

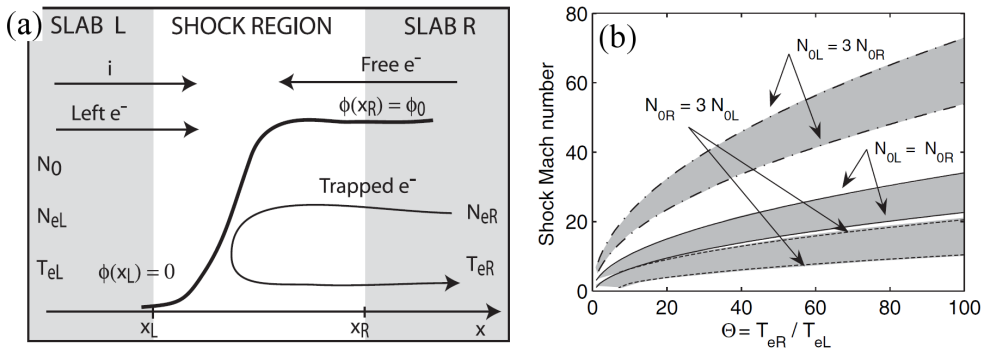

Figure 1.10: (a) ES potential at a shock and (b) maximum Mach-number of the shock as a function of the electron temperature ratio. [31]

generated in counter-streaming plasmas with different temperatures and densities.

1.6 Laboartory experiments in 1970s

Collisionless shocks have been studied experimentally using a double-plasma device[44, 45, 46] since 1970s. Double-plasma device was first developed by R. J. Taylor[47]. In this device, plasmas are separated by a negative biased grid. Applying various potential to one plasma with respect to the other, it is possible to generate large ion beams, large ion waves, and large amplitude ion acoustic shocks.

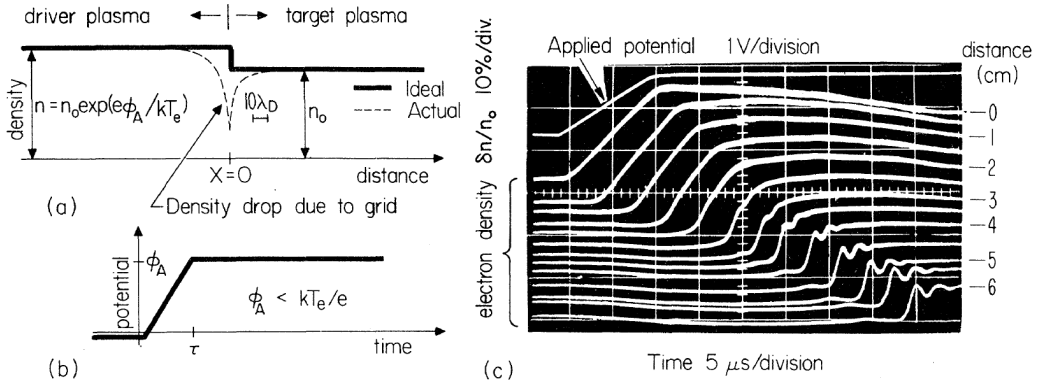

Figure 1.11: (a) The initial electron density profile. (b) The potential applied between two plasmas. (c) The plots of electron density versus time with distance as parameter. [44]

Figure 1.11(a) shows the initial electron density profile. In a double-plasma device, a potential is applied between two plasmas as shown in Fig. 1.11(b). Figure 1.11(c) shows the plots of electron density versus time at different positions. The density profiles clearly show a shock generation and propagation with a sharp density jump.

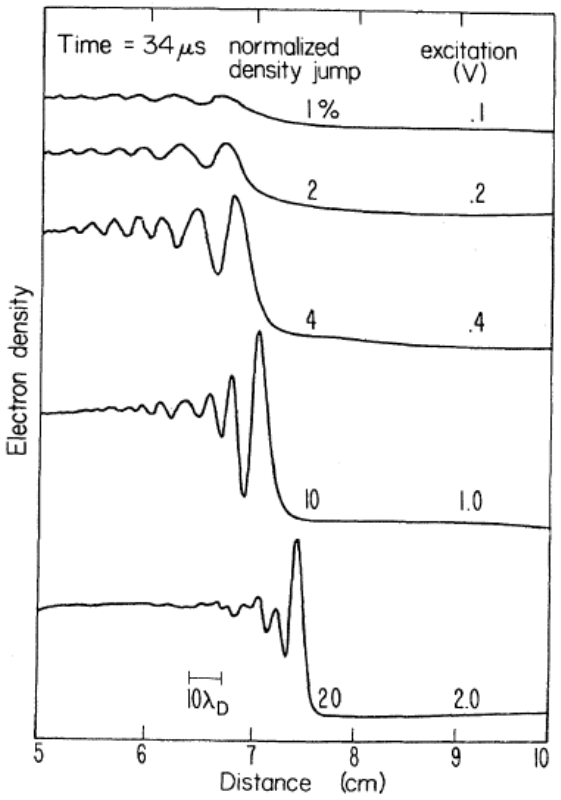

Figure 1.12: Electron density profiles in different excitation voltages at a fixed time. [44]

Figure 1.12 shows the electron density profiles for different excitation voltages at a fixed time. As the excitation voltage increases, shock amplitude increases, the shock velocity increases, shock width decreases, observed wave trains becomes short, and shock is attenuated more. These results suggest that the observed shock is related to a solition and shock structures are created due to energy dissipation such as ion reflections as argued in the subsection A.2.2.

1.7 Previous experiments with laser

Several experiments with long-pulse (> 10 ps) laser systems ($\simeq 10^{14}$–10^{15}W/cm^2) have been performed[48, 49, 50, 51, 50] to study collisionless shocks.

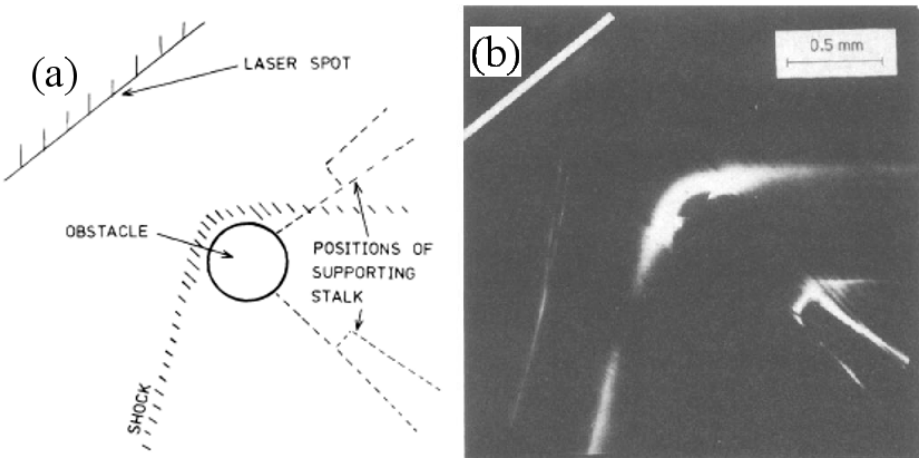

Figure 1.13: (a) The experimental setup and (b) the obtained schlieren image. [48]

A bow shock was demonstrated in the laboratory with a laser-produced plasma with an external magnetic field[48]; a spherical obstacle was exposed to a high-velocity plasma flow as shown in Figure 1.13(a), and a collisionless shock was generated around the obstacle as shown in Figure 1.13(b). The collisionless interaction was studied in counter-streaming laser-produced plasmas with an external magnetic field to demonstrate the shocks of SNRs as shown in Figure. 1.14[49, 51]. The plasma density profiles were different between data taken with and without magnetic field, but there was no evidence of shock generation. Romagnani *et al.* have studied collisionless shocks observed in an interaction between laser-produced ablating plasma and an ambient low-density plasma[50]. Nilson *et al.* have reported the experimental generation of a high Mach-number shock into the surrounding gas in a high-intensity laser-plasma interaction[52]. In these experiments[50, 52], although the shock generation was observed, the density profiles of the shocks were not measured.

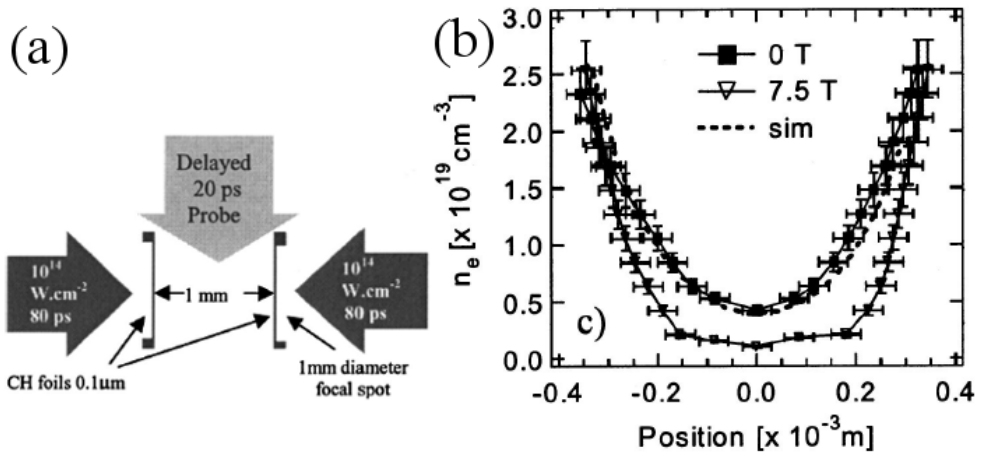

Figure 1.14: (a) The experimental setup and laser direction and (b) the density profiles obtained in counter-streaming collisionless plasmas with and without magnetic field. [49]

1.7.1 Particle acceleration with high-intensity laser

Particle acceleration in underdense plasmas created by short-pulse (< 1 ps) and high-intensity ($> 10^{19}$W/cm^2) laser systems has been measured[53, 54, 55]. The energy spectra of neutrons were compared with two-dimensional PIC simulation[55, 53]. The mechanism of neutron production is explained by nuclear reactions due to the energetic deuterons accelerated at the laser-irradiated surface. To understand the ion acceleration and resultant energy spectra, two-dimensional PIC simulations were performed. These results indicated that ions were accelerated at the shock front formed in the interaction between a high-intensity laser and an underdense plasma.

1.8 The goal of this research

In this thesis, we focus on collisionless ES shocks which are observed in an early stage of Weibel-mediated shock formation in large-scale laser-produced plasmas without an external magnetic field. We need longer time to observe the instabilities to destroy ES shock and the development of Weibel instability.

The possibility of Weibel-mediated shocks is argued in chapter C. We need higher density and velocity plasmas for Weibel-mediated shock generation in laboratories. This experiments can be performed using the laser system of national ignition facility (NIF). Collisionless shocks are generated in counter-streaming high-speed plasmas generated by high-power laser systems.

1.9 Outline

In chapter 2, we illustrate the principles of plasma diagnostics which have been used in laser-plasma experiments: shadowgraphy, interferometry, gated optical imager (GOI), and streaked optical pyrometer (SOP).

In chapter 3, we show the results of high Mach-number collisionless shock formation performed with Shenguang-II laser system. When two counter-streaming plasmas have different properties such as temperatures, densities, and velocities, a high Mach-number ES shock can be generated[31]. The result of this chapter is summarized in papers [T. Morita *et al*., Journal of Physics: Conference Series, 244, 042010 (2010)] and [T. Morita *et al*., Physics of Plasmas, 17, 122702 (2010)].

In chapter 4, we analyze the self-emission from laser-produced plasmas using a GOI and SOP to estimate brightness temperature and electron temperature. These results are applied to the experimental data performed using Gekko-XII HIPER laser system. This chapter is summarized in a paper [T. Morita *et al*., Astrophysics and Space Science, in press (2010)].

In chapter 5, we present the collisionless shock generation associated with the plasma jet collimation. This experiment was performed with Gekko-XII (GXII) HIPER laser system. This chapter is based on a paper [T. Morita *et al*, Physics of Plasmas, submitted]. In chapter 6, we summarize and conclude this thesis.

Chapter 2

Diagnostics

In this chapter, we focus on the diagnostics which are used in laser-produced plasma detection with high-power laser systems. First, the probe diagnostics to detect the electron density or density deviation are shown: interferometry and shadowgraphy. Second, the self-emission measurements are shown. In these diagnostics the self-emission intensity in a certain wavelength is measured using gated CCD cameras or streak cameras.

2.1 Interferometry

Interferometry is widely used to measure the density not only in plasma experiments but also in other fields such as astronomical observation, noncontact measurements of gas flows and so on, and is applied to many techniques: autofocus cameras, phase microscope, and fiber-optic gyroscopes. In plasma measurements, electron density n_{e}, is one of the most important parameter. In this thesis, n_{e} is measured with short-pulse laser (~ 100 ps) in the experiment with Shenguang-II laser system (chapter 3) or with long-pulse laser (~ 10 ns) and gated intensified charge coupled device camera (ICCD camera) (120–250 ps in FWHM) in the experiment with GXII HIPER laser system (chapter 5).

Interferometry measures phase differences of light between rays which pass through

plasmas and vacuum.

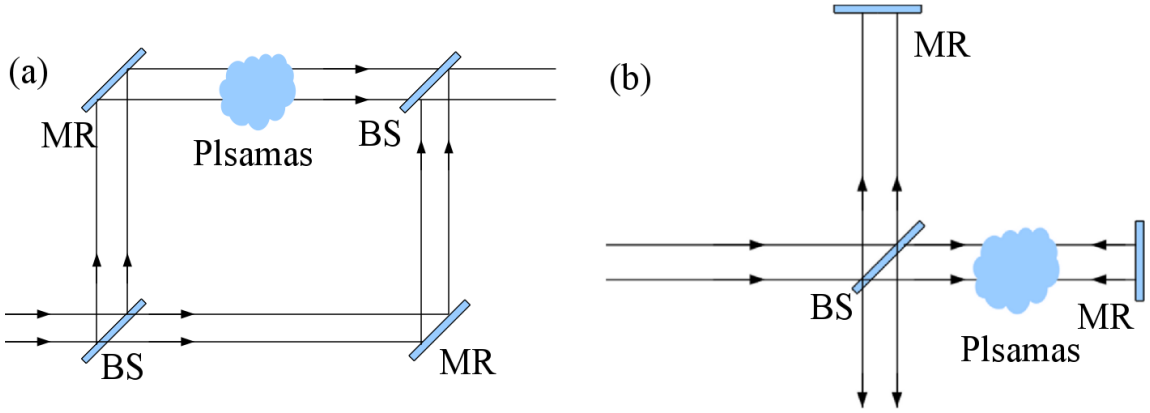

Figure 2.1: The basic arrangements of (a) Mach-Zender and (b) Michelson interferometry. BS and MR mean beam splitter and mirror, respectively.

There are some kinds of interferometry methods, such as Mach-Zender, Michelson, and Nomarski. In Mach-Zender and Michelson interferometries, one beam is devided to two beams before passing through plasmas: one passes through plasmas and the other passes through vacuum as shown in Figs. 2.1(a) and 2.1(b). On the other hand, in Nomarski interferometry, we use one beam before passing through plasma.

2.1.1 Nomarski interferometry

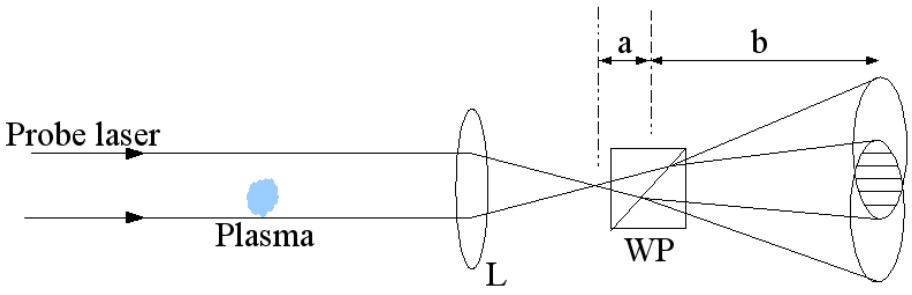

Figure 2.2: The basic arrangements of Nomarski interferometry. A probe beam is divided with Wollaston prism (WP).

Figure 2.2 shows a typical configuration of Nomarski interferometry. A probe beam is

divided into two rays with a Wollaston prism to interfere each other. A wollaston prism divides a beam into two beams which are orthogonally polarized with a certain small angle θ (i.e. 1°, 3°, or 5° in our experiments). The fringe separation δ can be evaluated with the distance between the prism and the focal spot of a lens a, and the distance between the prism and a detector b,

$$\delta \sin\theta = \lambda \frac{b}{a} \tag{2.1}$$

$$\delta = \frac{b\lambda}{a \sin\theta} \simeq \frac{b\lambda}{a\theta}, \tag{2.2}$$

where λ is the wavelength of the probe laser.

In plasmas, the refractive index μ is expressed as

$$\mu = \sqrt{1 - n_{\rm e}/n_{\rm c}}, \tag{2.3}$$

where $n_{\rm c}$ is the critical density. Phase difference $\delta\theta$ between two rays (one passes through plasmas and the other passes through vacuum) is expressed by an optical path length l as

$$\begin{aligned} \delta\theta &= (\omega/c)(l\mu - l) && (2.4)\\ &= \frac{\omega}{c}\int(\sqrt{1 - n_{\rm e}/n_{\rm c}} - 1)dl && (2.5)\\ &\simeq -\frac{\omega}{2n_{\rm c}c}\int n_{\rm e} dl, && (2.6) \end{aligned}$$

where ω is the frequency of the probe beam and c is the speed of light. Here, we assumed $n_{\rm e}$ is sufficiently smaller than $n_{\rm c}$.

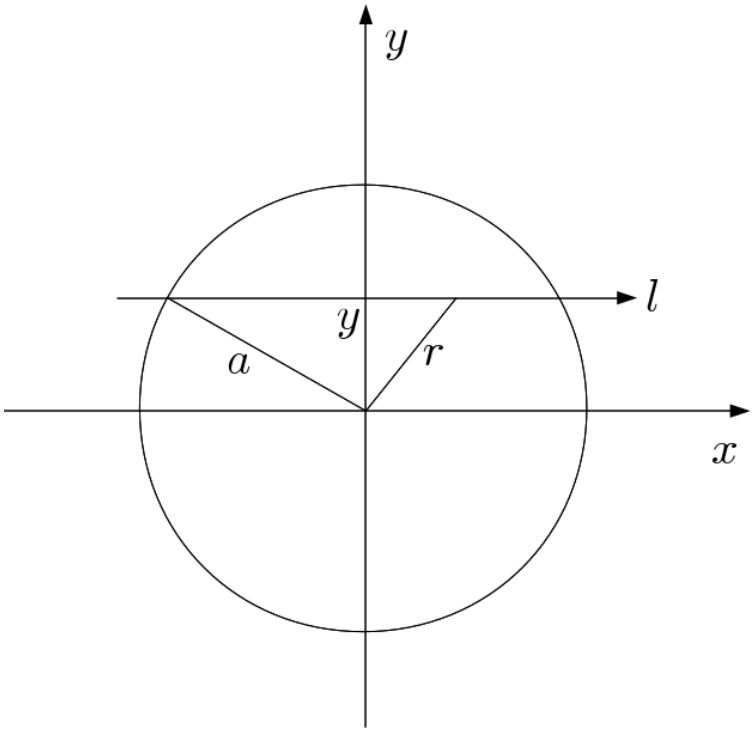

Figure 2.3: The cross-section view of laser-produced plasmas. A probe laser passed from left to right as shown with l.

2.1.2 Abel inversion

Assuming that plasmas are created with an axial symmetry, $\delta\theta$ is expressed using the parameters shown in Fig. 2.3,

$$\delta\theta = -\frac{\omega}{n_c c}\int_0^{\sqrt{a^2-y^2}} n_e(r)dx \tag{2.7}$$

$$= -\frac{\omega}{n_c c}\int_y^a \frac{n_e(r)rdr}{\sqrt{r^2-y^2}}. \tag{2.8}$$

Figure 2.3 shows the cross-section view of an plasmas. l is the path of a probe laser, a is the radius of the axially symmetrical plasma, and y, r, and x are defined in Fig. 2.3. Applying the Abel inversion method to equation (2.8), we obtain n_e with the phase difference $\delta\theta$,

$$n_e(r) = \frac{2n_c c}{\pi\omega}\int_r^a \frac{d(\delta\theta)}{dy}\frac{1}{\sqrt{y^2-r^2}}dy. \tag{2.9}$$

If experimental data are noisy, the derivative $d(\delta\theta)/dy$ can be very large and can not be smooth. To avoid the discontinuity of $d(\delta\theta)/dy$ in experimental data, we can use the following formula by integrating equation (2.9) by parts,[56]

$$n_e(r) = \frac{2n_c c}{\pi\omega}\left[\frac{\delta\theta(y)}{\sqrt{y^2-r^2}}\bigg|_{y=r}^{y=a} + \int_r^a \frac{ydy}{(y^2-r^2)^{3/2}}\right]. \tag{2.10}$$

In this thesis, Abel inversion is calculated with Bockasten's method[57, 58] and derivative-free inversion[56] shown in equation (2.10).

2.1.3 Application to experimental data

2.2 Shadowgraphy

The difference between an interferometry and a shadowgraphy is whether a probe laser is divided into two or not. In a shadowgraphy, we can measure, roughly, the second derivative of the electron density in plasmas while the interferometry is sensitive to the absolute density. In this section we briefly explain the shadowgraph technique.

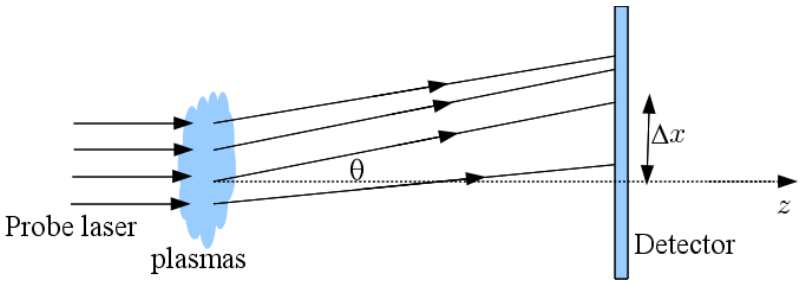

Figure 2.4: Schematic view of a shadowgraphy. Rays in a probe laser are deflected by plasmas

Figure 2.4 shows the side view of a shadowgraphy. The incident beam is diffracted when it propagates in plasmas, and the diffracted angle θ is expressed with the refractive index μ,

$$\theta_x \simeq \int \frac{d^2x}{dz^2} dz = \int \frac{1}{\mu} \frac{\partial \mu}{\partial x} dz, \tag{2.11}$$

$$\theta_y \simeq \int \frac{d^2y}{dz^2} dz = \int \frac{1}{\mu} \frac{\partial \mu}{\partial y} dz, \tag{2.12}$$

where z is the axis of the probe laser. Here, we define the initial intensity $I_{\mathrm{i}}(x, y)$ is the light intensity with no plasmas, and the detected intensity $I^{'}(x^{'}, y^{'})$ with plasmas, where $x^{'}$

and $y^{'}$ are new coordinates,

$$x^{'} = x + \Delta x = x + \theta_x l = x + l \int \frac{1}{\mu} \frac{\partial \mu}{\partial x} dz, \tag{2.13}$$

$$y^{'} = y + \Delta y = y + \theta_y l = y + l \int \frac{1}{\mu} \frac{\partial \mu}{\partial y} dz. \tag{2.14}$$

The relationship between the initial intensity $I(x, y)$ with no plasmas and the detected intensity $I^{'}(x^{'}, y^{'})$ with plasmas is expressed:

$$I(x, y)dxdy = I^{'}(x^{'}, y^{'})dx^{'}dy^{'} \tag{2.15}$$

and if we neglect the product of Δx and Δy, we obtain

$$\left| \frac{\partial(x^{'}, y^{'})}{\partial(x, y)} \right| \simeq 1 + \frac{\partial \Delta x}{\partial x} + \frac{\partial \Delta y}{\partial y}. \tag{2.16}$$

$I^{'}$ is expressed using I and the coordinates (x, y),

$$\frac{I}{I'} = 1 + l \int \left(\frac{\partial}{\partial x} \left(\frac{1}{\mu} \frac{\partial \mu}{\partial x} \right) + \frac{\partial}{\partial y} \left(\frac{1}{\mu} \frac{\partial \mu}{\partial y} \right) \right) dz, \tag{2.17}$$

$$\frac{I - I'}{I'} = l \int \left(\frac{\partial^2}{\partial x^2} + \frac{\partial^2}{\partial y^2} \right) (\ln \mu)\, dz. \tag{2.18}$$

Equation (2.18) indicates that the change of light intensity roughly expresses the second derivative of the refractive index μ.

2.3 Self-emission measurements

The intensity of the self-emission from plasmas gives information of the electron temperature and/or density. In an optically thick plasma, it can be regarded as a blackbody radiator, and $T_{\rm b} = T_{\rm e} = T_{\rm i}$, where $T_{\rm b}$, $T_{\rm e}$, and $T_{\rm i}$ are a brightness temperature, an electron tempera-

ture, and an ion temperature, respectively. On the other hand, in an optically thin plasma, $T_{\rm e}$ should be much larger than $T_{\rm b}$, and $T_{\rm e}$ can be estimated from thermal bremsstrahlung emission. In our experiments, the plasmas created by high-power laser systems were mainly optically thin, and $T_{\rm e}$ should be much larger than $T_{\rm b}$. Nevertheless the measurement of $T_{\rm b}$ in optically thin plasma is important because it depends on both $n_{\rm e}$ and $T_{\rm e}$, and a sudden $T_{\rm b}$ change shows $n_{\rm e}$ and/or $T_{\rm e}$ jump. Evaluating the bremsstrahlung emission, we can estimate $T_{\rm e}$ from the intensity of self-emission from laser-created plasmas.

In the experiments, both time variation and two-dimensional spacial information were measured by a streaked optical pyrometer (SOP) and gated optical imager (GOI).

2.3.1 Blackbody radiation

When a body is in thermal equilibrium at the temperature T and it is optically thin, photons obey the Bose-Einstein statistics. The partition function Z is defined as

$$Z = \sum_{i=0}^{\infty} e^{-E_i/k_{\rm B}T} = \sum_{i=0}^{\infty} e^{-\beta i h\nu} \tag{2.19}$$

$$= \frac{1}{1-e^{-\beta h\nu}}, \tag{2.20}$$

where $\beta = 1/k_{\rm B}T$, E_i is the i-th energy state, and h is the Planck constant. The possibility for a photon in the energy state $E_i = ih\nu$ is

$$\frac{e^{i\beta h\nu}}{Z}, \tag{2.21}$$

and therefore, the average energy is calculated as follows.

$$\begin{aligned} \langle E \rangle &= \sum_i \frac{E_i e^{-\beta E_i}}{Z} && (2.22) \\ &= -\frac{\partial}{\partial \beta} \left(\ln Z \right) && (2.23) \\ &= \frac{h\nu}{e^{\beta h\nu} - 1} && (2.24) \end{aligned}$$

In a phase space, the number of state in a volume $4\pi p^2 dp$ is calculated considering spin 1 for photon,

$$n_{\mathrm{s}} = \frac{2 \times 4\pi \left(h\nu/c \right)^2 d \left(h\nu/c \right)}{h^3} = \frac{8\pi\nu^2}{c^3}. \tag{2.25}$$

As a result, the energy emitted per unit area per unit time per unit solid angle $B(T)d\nu$ is calculated from equations (2.24) and (2.25).

$$\begin{aligned} B_\nu(T)d\nu &= \frac{c}{4\pi} \langle E \rangle n_{\mathrm{s}} && (2.26) \\ &= \frac{2h\nu^3/c^2}{\exp\left(h\nu/k_{\mathrm{B}}T \right) - 1} d\nu. && (2.27) \end{aligned}$$

The function $B_\nu(T)$ is called the Planck law. If we calculate the Planck law in terms of the wavelength λ, we obtain $B_\lambda(T)$

$$B_\lambda(T) = \frac{2hc^2/\lambda^5}{\exp(hc/\lambda k_{\mathrm{B}}T)}. \tag{2.28}$$

2.3.2 Thermal bremsstrahlung

When an electron passes by an ion, its orbit is bended and it emits bremsstrahlung radiation. Consider one electron passes by an ion with an impact parameter b. The emission intensity

in unit angular frequency is calculated as[59]

$$\frac{dW}{d\omega} = \begin{cases} \frac{e^2}{6\pi^2\epsilon_0 c^3} |\Delta v|^2 & (\omega \ll v/b) \\ 0 & (\omega \gg v/b), \end{cases} \tag{2.29}$$

where Δv is the change of the electron velocity during the collision. The change of the electron momentum is calculated by multiplying the force perpendicular to the orbit by the interaction time:

$$\Delta p = m\Delta v = \int_{-\infty}^{\infty} \frac{bZe^2}{4\pi\epsilon_0(x^2+b^2)^{3/2}} \tag{2.30}$$

$$= \frac{ze^2}{2\pi\epsilon_0 vb}. \tag{2.31}$$

$$\tag{2.32}$$

Therefore,

$$\Delta v = \frac{ze^2}{2\pi\epsilon_0 mvb}. \tag{2.33}$$

The emission intensity in plasmas in unit volume unit time is calculated using equations (2.29) and (2.33), n_e, and ion density n_i,

$$\frac{dW}{d\omega dV dt} = n_\mathrm{e} v n_\mathrm{i} \int_{b_\mathrm{min}}^{b_\mathrm{max}} \frac{dW}{d\omega} 2\pi b db \tag{2.34}$$

$$= \frac{Z^2 e^6 n_\mathrm{e} n_\mathrm{i}}{12\sqrt{3}\pi^2\epsilon_0^3 m^2 c^3 v} g_{ff}, \tag{2.35}$$

where $g_{ff} = \ln(b_\mathrm{max}/b_\mathrm{min})$ is the Gaunt factor.

When T_e is high, electrons moving with thermal velocity emit bremsstrahlung radiation, that is, the thermal bremsstrahlung radiation. Assuming T_e distribution is Maxwellian, the

total emission intensity in the plasma is obtained by taking the average of equation (2.35),

$$\frac{dW(T)}{d\omega dV dt} = \frac{\int_{v_{\min}^{\infty}} \frac{dW}{d\omega dV dt} v^2 \exp(-\frac{mv^2}{2k_{\rm B}T}) dv}{\int_0^{\infty} v^2 \exp(-\frac{mv^2}{2k_{\rm B}T}) dv} \tag{2.36}$$

$$= \frac{Z^2 e^6 n_{\rm e} n_{\rm i}}{6\sqrt{3}\pi^{5/2}\epsilon_0^3 m^2 c^3} \sqrt{\frac{m}{2k_{\rm B}T}} \exp\left(-\frac{mv_{\min}^2}{2k_{\rm B}T}\right) g_{ff}. \tag{2.37}$$

We obtain the emission intensity in terms of the frequency $\nu = \omega/2\pi$,

$$\epsilon_\nu^{ff} = \frac{dW(T)}{dV dt d\nu} = \frac{Z^2 e^6 n_{\rm e} n_{\rm i}}{3\sqrt{3} m c^3 \epsilon_0^3 \pi^{3/2}} \frac{1}{\sqrt{2mk_{\rm B}T}} \exp\left(-\frac{h\nu}{k_{\rm B}T}\right) g_{ff} \tag{2.38}$$

$$\propto \frac{n_{\rm e}^2}{\sqrt{T}} \exp\left(-\frac{h\nu}{k_{\rm B}T}\right) \tag{2.39}$$

Equation (2.38) or (2.39) shows that the emission intensity does not strongly depend on $T_{\rm e}$ but on $n_{\rm e}$ especially in high-temperature plasmas.

2.3.3 Optical thickness

When a ray passes through plasmas, the emission and absorption have the following relationship

$$\frac{dI_\nu}{ds} = -\alpha_\nu I_\nu + j_\nu, \tag{2.40}$$

where α_ν and j_ν are the coefficients of the absorption and emission, respectively, and I_ν is the intensity of the light. Using a variable τ_ν, which is defined by

$$\tau_\nu = \int_{s_0}^{s} \alpha_\nu ds, \tag{2.41}$$

equation (2.40) becomes

$$\frac{dI_\nu}{d\tau_\nu} = -I_\nu + S_\nu, \tag{2.42}$$

where S_ν is the source function defined by the emission and absorption coefficients: $S_\nu = j_\nu/\alpha_\nu$. We can easily solve the above equation.

$$I_\nu = I_\nu(0) + \int_0^{\tau_\nu} \exp(\tau_\nu^{'} - \tau_\nu) S_\nu(\tau_\nu^{'}) d\tau_\nu^{'} \tag{2.43}$$

When S_ν is constant at any places in the plasmas,

$$I_\nu(\tau_\nu) = I_\nu(0) e^{-\tau_\nu} + S_\nu(1 - e^{-\tau_\nu}). \tag{2.44}$$

Here, we define the mean–free–path for photons l_ν

$$\alpha_\nu l_\nu = \langle \tau_\nu \rangle = \int_0^\infty \tau_\nu e^{-\tau_\nu} d\tau_\nu = 1. \tag{2.45}$$

If l_ν is much larger than the plasma size, for example in low-density and high-temperature plasmas, the thermal bremsstrahlung emission can be observed. On the other hand, when l_ν is small, the emission is expressed with the blackbody radiation.

2.3.4 Gated optical imager (GOI) and Streaked optical pyrometer (SOP)

Self-emission from laser-produced plasmas is detected by an ICCD camera or a streak camera. In our experiments, we observe the emission using band-pass filters which have the central wavelength of ~ 450 nm. When we use the ICCD camera as a GOI, we observe a two-dimensional image of the emission at a certain time. On the other hand, when we use the streak camera as a SOP, we observe the time evolution of an one-dimensional image. In chapter 4, we show the calibration methods of the GOI and SOP, and also the experimental

data. In chapter 5, we analyze the SOP to determine $T_{\rm e}$ and $n_{\rm e}$.

Chapter 3

High Mach-number collisionless electrostatic shock generation

3.1 Introduction

Recently, PIC simulations have shown the possibilities for generation of collisionless shocks in counter-streaming plasmas without an external magnetic field[34, 30, 32, 31]. In Ref. [30], a collisionless shock was formed by the Weibel instability in counter-streaming plasmas. The possibility for an experiment with a high-power laser system was discussed in Ref. [32]. In a series of PIC simulations to study collisionless shock formation in such counter-streaming plasmas, an ES shock is produced in the early stages before the final electromagnetic-field-mediated shock is formed. It is found that the appearance of the ES shock is a transitional phenomenon and it disappears in a short time[34]. We have tried to measure this ES shock formation in counter-streaming plasmas, and were able to measure a large density jump that represents a shock. As a result, it is identified from the jump condition that the ES shock is strong, namely high Mach-number ($M > 10$), and the physical mechanism for the shock formation was proposed in Ref. [31]. In order to clarify the physical mechanism, we also carried out PIC simulations and found that ion reflection by the electrostatic

potential towards upstream region was essential to the formation of the shock.

In this chapter, we focus on the measurement and analysis of this ES shock, to investigate whether its theoretical model can be reproduced in the experiment in a two-boundary expanding plasma assumed in Ref. [31]. We show the measured data of a density jump which represents a collisionless shock in counter-streaming plasmas created by a high-power and long-pulse (1 ns) laser system without an external magnetic field. The density jump is about 3.9, which represents a high Mach-number shock generation. Quasi-one-dimensional PIC simulations show the excitation of a collisionless high Mach-number ES shock through the counter-streaming interaction of two plasma slabs with different temperatures and densities.

3.2 Experimental setup

The experiment was performed at the Shenguang-II laser facility in Shanghai, China. There are eight main beams with 260 J/beam, the wavelength is 351 nm (3ω) and pulse width is 1 ns. Figure 4.6(a) shows the top view of the experimental setup. Our targets consist of two thin plastic (CH) foils. The size of each foil is 2 mm $\times$ 2 mm $\times$ 100 μm, and the two foils are separated by 4.5 mm. Four beams were focused on the inner surface of one of the CH foils (first CH) with the incident angle of 60 degrees from the target normal direction, with a focal spot 150 μm in diameter, giving an intensity of $\simeq 6 \times 10^{15}$W/cm^2. A short-pulse laser with pulse width of 70 ps and wavelength of 527 nm (2ω) was used for a probe laser. In the experiment, plasma expansion was measured with Nomarski interferometry and shadowgraphy. The interferometry is sensitive to the electron density, and the shadowgraphy depends on the second derivative of the electron density [60]. In the optical path for Nomarski interferometry, a Wollaston prism was placed near the focal spot of the probe laser. This prism can split incident light into two orthogonal, linearly polarized beams. Two polarizers were placed before the vacuum chamber and

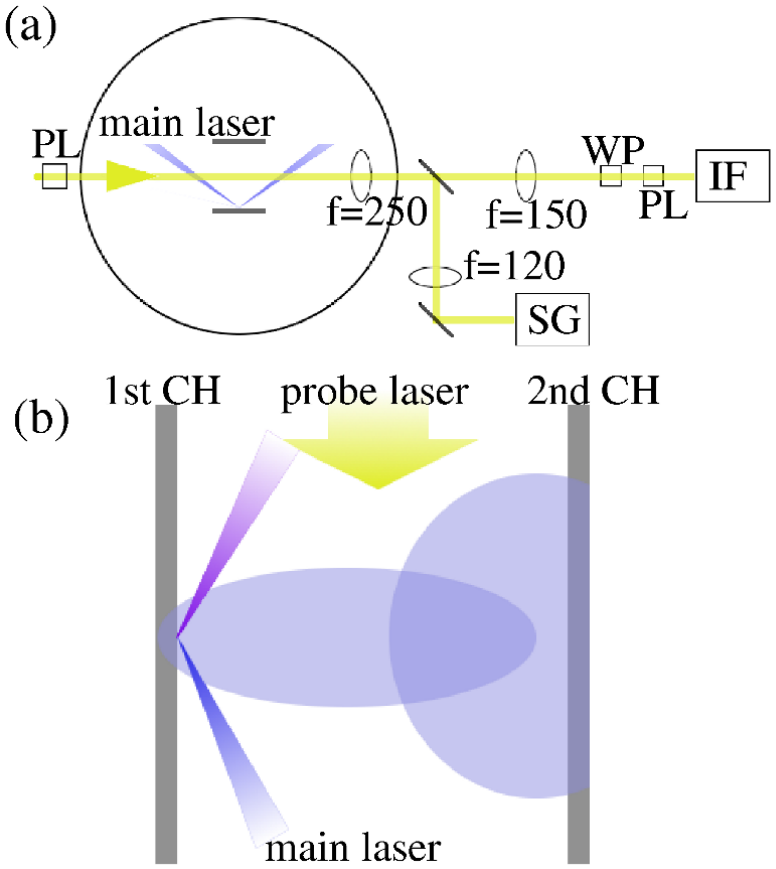

Figure 3.1: (a) The top view of experimental setup. SG and IF represent the ICCD cameras for shadowgraphy and interferometry, respectively, WP is the Wollaston prism and PL is the polarizer. (b) Schematic view of the target design.

after the Wollaston prism so that the two beams interfered at the photoelectric surface of an ICCD camera. In the path of the shadowgraphy, the incident probe beam passed through the plasmas and was directly detected by a second ICCD camera. Figure 4.6(b) shows the schematic view of our target. The plasma flow from the other CH foil (second CH) was produced by the radiation and/or plasma from the first CH. As a result, the counter-streaming plasma flows were created between the two foils and interacted with each other near the surface of the second CH.

The interferograms and shadowgraphs were taken in the same region and timing, and hence the density profile and the derivative of the density gradient can be compared.

3.3 Result

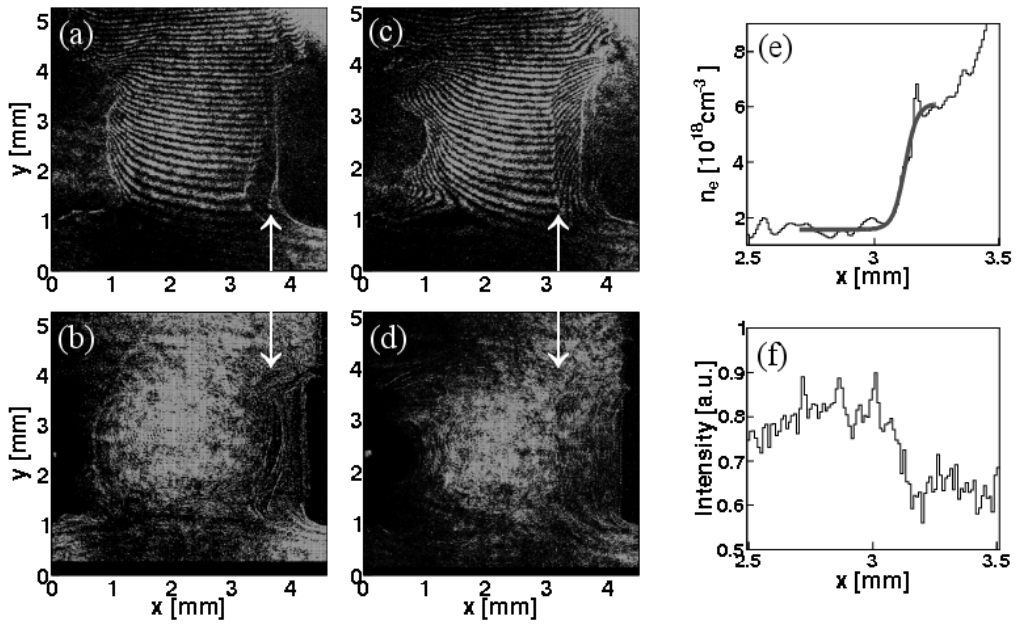

Figure 3.2: (a) The interferogram and (b) shadowgraph measured at $t = 5$ ns. (c) The interferogram and (d) shadowgraph measured at $t = 9$ ns. The horizontal coordinate $x = 0$ and 4.5 mm are the surface of the first and second CH foils, respectively. Four beams were focused on the first CH at $x = 0$ and $y = 2.5$ mm. (e) The density profile measured at $y = 3.5$ mm and $t = 9$ ns. A large density jump is observed at $x \simeq 3.1$ mm. (f) The average intensity profile of Fig. 3.2(d) for y =3.0–4.0 mm.

The phase difference $\delta\theta$ between two rays (one passes through plasmas and the other passes through vacuum) is expressed by an optical path length l as $\delta\theta = \omega/(2n_{\rm c}c)\int n_{\rm e}(l)\mathrm{d}l$, where ω is the frequency of the probe beam, $n_{\rm c}$ is the critical density, $n_{\rm e}$ is the electron density and c is the speed of light. Assuming that plasmas are created axially symmetrically, $n_{\rm e}$ can be calculated by Abel inversion with Bockasten's method[57, 58].

Figures 3.2(a) and 3.2(b) show an interferogram and shadowgraph, respectively, measured at 5 ns after the peak of the main laser ($t = 5$ ns). The horizontal coordinate x represents the distance from the surface of the first CH. Some fine structures vertical to the flow direction are observed near the second CH in Fig. 3.2(b) at $x \simeq 3.6$–3.7 mm. Whereas

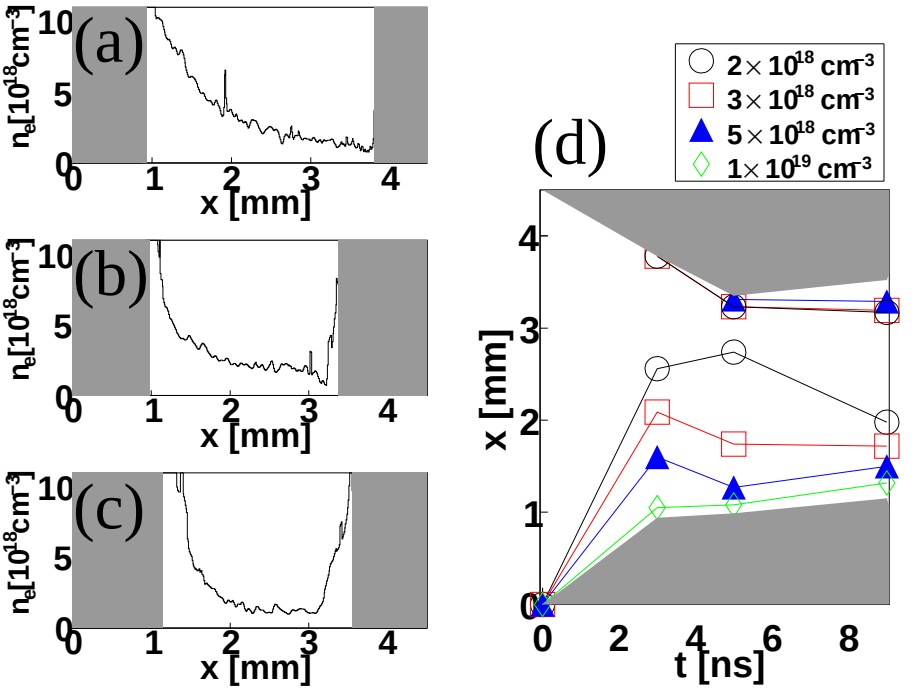

Figure 3.3: The density profiles measured at (a) $t = 3$ ns, (b) $t = 5$ ns, and (c) $t = 9$ ns. These profiles are calculated at the center of the target parallel to the symmetrical axis in each profile used for Abel inversion. (d) The x position of given densities as a function of t. Filled regions in above figures are the regions where the interference fringes cannot be observed and the density cannot be calculated.

the density in this region is too high and the absolute value can not be calculated from the interferogram, there is a very large density gradient. Figures 3.2(c) and 3.2(d) show the interferogram and shadowgraph, respectively, measured at $t = 9$ ns. In Fig. 3.2(c), interference fringes suddenly shift and a large density jump exists near the second CH. Figure 3.2(e) shows the density profile at $y = 3.5$ mm and $t = 9$ ns. This large density jump is estimated with following equation:

$$n_{\mathrm{e}}(x) = a + b\tanh((x - x_{\mathrm{s}})/W), \tag{3.1}$$

where a, b, x_{s}, and W are the parameters defined by fitting the density profile shown in Fig. 3.2(e). The downstream to upstream density ratio n_1/n_0, the width W, and the

position $x_{\rm s}$ are evaluated as $n_1/n_0 = (a+b)/a = 3.89 \pm 0.85$, $W = 48.6 \pm 34.5$ μm, and $x_{\rm s} = 3.12 \pm 0.02$ mm, respectively. The width W has a large relative error of 71 %, however, it is smaller than ~ 100 μm. Figure 3.2(f) shows the average (y = 3.0–4.0 mm) intensity profile of Fig. 3.2(d). The intensity of the probe beam suddenly changes at the same position that the density jumps ($x \simeq 3.1$ mm). This sudden brightness change represents a large density change. The sharp structure at $x \simeq$ 3.6–3.7 mm in Fig. 3.2(b) moved to $x \simeq$ 3.1 mm as shown in Fig. 3.2(d) in 4 ns. This means that the observed density discontinuity propagates from right to left slowly ($v \simeq$ 130 km/s). The range of $n_{\rm e}$ calculated from the interferogram is about 1×10^{18}–5×10^{19} cm^{-3}.

Figures 3.3(a)–3.3(c) show the average ($y \simeq$ 2.3–2.7 mm in Fig. 3.2) density profiles at $t = 3$ ns (not shown), 5 ns, and 9 ns, respectively. Figure 3.3(d) shows the x position of given densities as a function of t derived from Figs. 3.3(a)–3.3(c). Assuming that the plasmas start moving at t = 0 with constant velocities, the flow velocity $v_{\rm first}$ of the plasma with $n_{\rm e} \simeq 2 \times 10^{18}$ cm^{-3} from the first CH is estimated as $v_{\rm first} = \Delta x/\Delta t \simeq 2.5$ mm$/3.0$ ns $\simeq$ 830 km/s, and the velocity from the second CH ($n_{\rm e} \gtrsim 2\times10^{18}$ cm^{-3}) is $v_{\rm second} = \Delta x/\Delta t \simeq 0.7$ mm$/3.0$ ns $\simeq$ 230 km/s.

The ion-ion mean-free-path $\lambda_{\rm ii}$, for the counter-streaming plasmas, is expressed as $\lambda_{\rm ii} = 2\pi\epsilon_0^2 m_{\rm i}^2 v^4/(n_{\rm i} Z^4 e^4 \ln\Lambda)$ [61], where $m_{\rm i}$ is the average ion mass $m_{\rm i} \simeq A m_{\rm p}$ (average mass number $A = 6.5$, $m_{\rm p}$ is the proton mass), v is the relative velocity of the counter-streaming plasmas, the average degree of ionization $Z = 3.5$ (C^{6+}, H^+), the average ion density $n_{\rm i} = n_{\rm e}/Z$, e is the elementary charge, and $\ln\Lambda$ is the coulomb logarithm. The coulomb logarithm is calculated with the following formula with reduced mass $m_{\rm r} = (1/m_{\rm first} + 1/m_{\rm second})^{-1} = m_{\rm i}/2$, $\ln\Lambda = \ln(4\pi\epsilon_0\lambda_{\rm D} m_{\rm r} v^2/(Z^2e^2))$, where $m_{\rm first}$ and $m_{\rm second}$ are the ion masses coming from the first and second CH, respectively, and $\lambda_{\rm D}$ is the Debye length. From the values of relative velocity $\simeq 1060$ km/s at $t = 3ns$ and electron density $n_{\rm e} = 8 \times 10^{18}$ cm^{-3}, $\lambda_{\rm ii}$ is calculated as $\lambda_{\rm ii} = 35$ mm for the electron temperature $T_{\rm e} = 1$ eV and 25

mm for $T_{\rm e} = 1000$ eV. At $t = 9$ ns, a simple estimation gives $v = 4.5$ mm/9 ns $= 500$ km/s and $\lambda_{\rm ii} = 1.7$ mm for $T_{\rm e} = 1$ eV and 1.2 mm for $T_{\rm e} = 1000$ eV. It is difficult to estimate $T_{\rm e}$ in our diagnostics, however $\lambda_{\rm ii}$ does not strongly depend on $T_{\rm e}$. Since the width of the measured density jump at $t = 9$ ns ($\simeq 100\mu$m) was much shorter than $\lambda_{\rm ii}$, the counter-streaming plasmas created in our experiment are collisionless, and this density jump is due to collisionless interaction.

3.4 Simulation

3.4.1 Collisionless shock formation

We performed a quasi-one-dimensional PIC simulations to investigate the ES shock formation and propagation in counter-streaming plasma flows[34]. The simulation is two-dimensional but we take 8 grids in the y direction, which is small compared with 8192 grids in x direction, so that the simulation is essentially one-dimensional in x direction. The ratio of the ion mass to the electron mass is 1836. The ratios of the electron to ion temperatures are 4 in both plasma flows. Such a temperature difference between the ion and electrons is commonly seen in one-dimensional laser plasma hydrodynamic codes, for example, ILESTA-1D[62]. Therefore, such initial conditions for the PIC simulation is appropriate in the case of laser ablated plasmas.

Figures 3.4(a) and 3.4(b) show the phase-space plots of ions at $\omega_{\rm pe}t = 800$ and 2000, respectively. The vertical axis is the ion velocity and the horizontal axes are the length in units of the electron inertial length $\lambda_{\rm e} = c\omega_{\rm pe}^{-1}$ at the top and that in μm at the bottom. Figures 3.4(c) and 3.4(d) show the corresponding ion density distributions. The shocks are generated at about $\omega_{\rm pe}t \sim 800$ and they propagate toward $\pm x$ directions. The electron temperature, density, and flow velocity are 50 eV, 2×10^{18} cm^{-3}, and 800 km/s for the left-plasma, and 750 eV, 6×10^{18} cm^{-3}, and 200 km/s for the right-plasma. The temperature

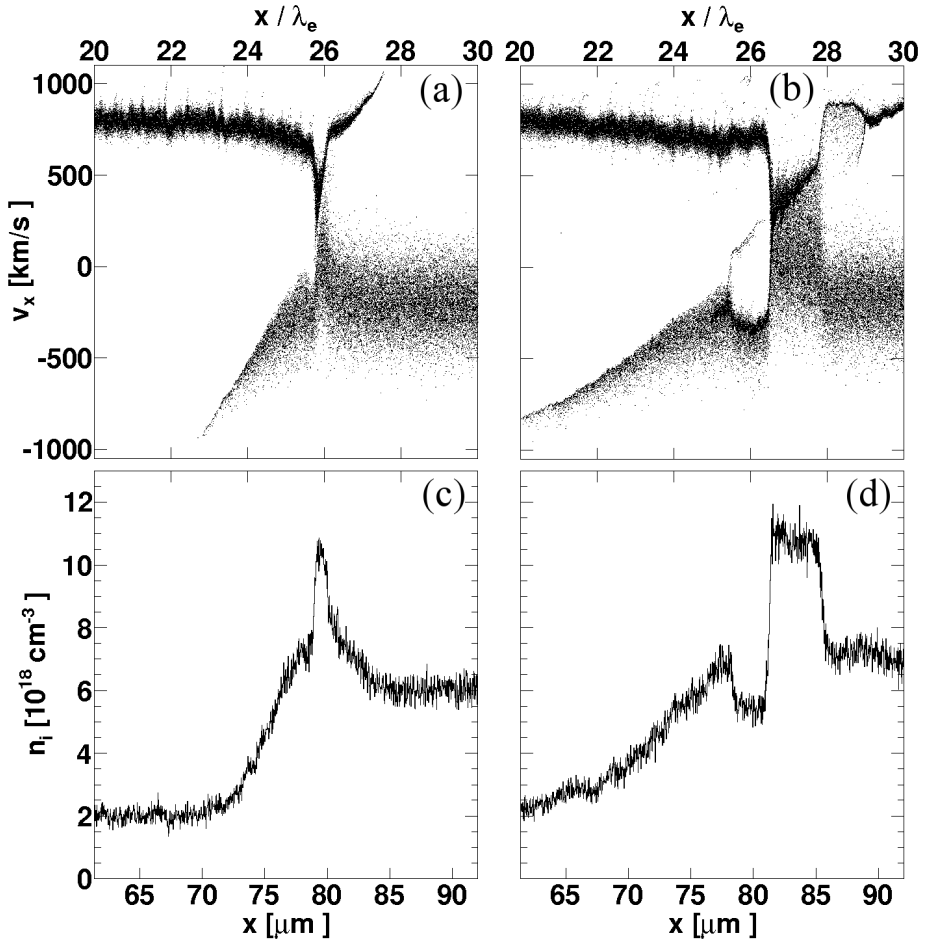

Figure 3.4: The phase-space plots and corresponding ion density profiles at $\omega_{\rm pe}t = 800$ [(a) and (c)] and 2000 [(b) and (d)].

of the left-plasma is much higher than the right one at the laser timing. As time passes, the left-plasma is cooled down and the second CH is ablated by the radiation from the left-plasma or by the left-plasma itself. The kinetic energy of the left-plasma is converted to the thermal energy of the right-plasma near the second CH. Hence, after the laser timing, the temperature of the right-plasma is relatively higher than the left-plasma especially near the second CH.

Here, the measured values are used for the electron densities and flow velocities. It is clear that the incoming ions are slowed down or reflected at two shock fronts: $x/\lambda_e = 26.5$

and 27.8 ($x = 81.3$ and 85.3 μm) in Figs. 3.4(b) and 3.4(d), respectively. The density ratio of the left-side shock is about 5. It is clearly observed that there are reflected ions in the upstream region and the ion density is relatively higher than the initial density. The velocity of the left-side shock is about $v_{\rm s} = 600$ km/s in the upstream rest frame, and a sound velocity in the upstream region is $C_{\rm s} = 69$ km/s, therefore, the Mach-number of the left-side shock is ~ 8.7.

3.4.2 Time evolution of shock generation

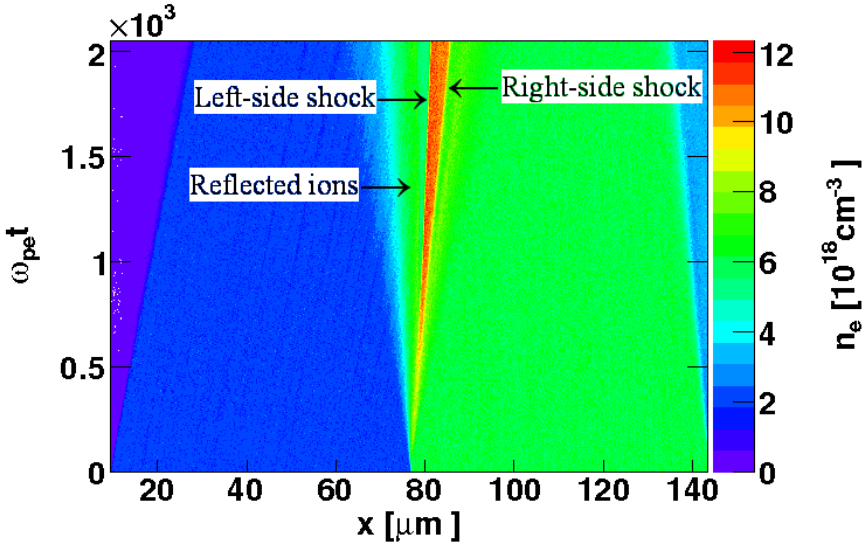

Figure 3.5: The time evolution of the ion densities. The profiles at $\omega_{\rm pe}t \sim 800$ and 2000 are shown in Figs. 3.4(c) and 3.4(d), respectively.

Figure 3.5 shows the time evolution of the ion density profile. The parameters are same as those shown in Fig. 3.4. At $\omega_{\rm pe}t = 0$, counter-streaming flows start to interact each other and two shocks propagete. The density increases in front of the left-side shock because of the reflected ions.

Figures 3.6(a)–3.6(h) show the phase-space plots of electrons [(a), (c), (e), and (g)], and of ions [(b), (d), (f), and (h)] at $\omega_{pe}t = 0$, 5, 65, and 135, respectively. Figures 3.6(a)

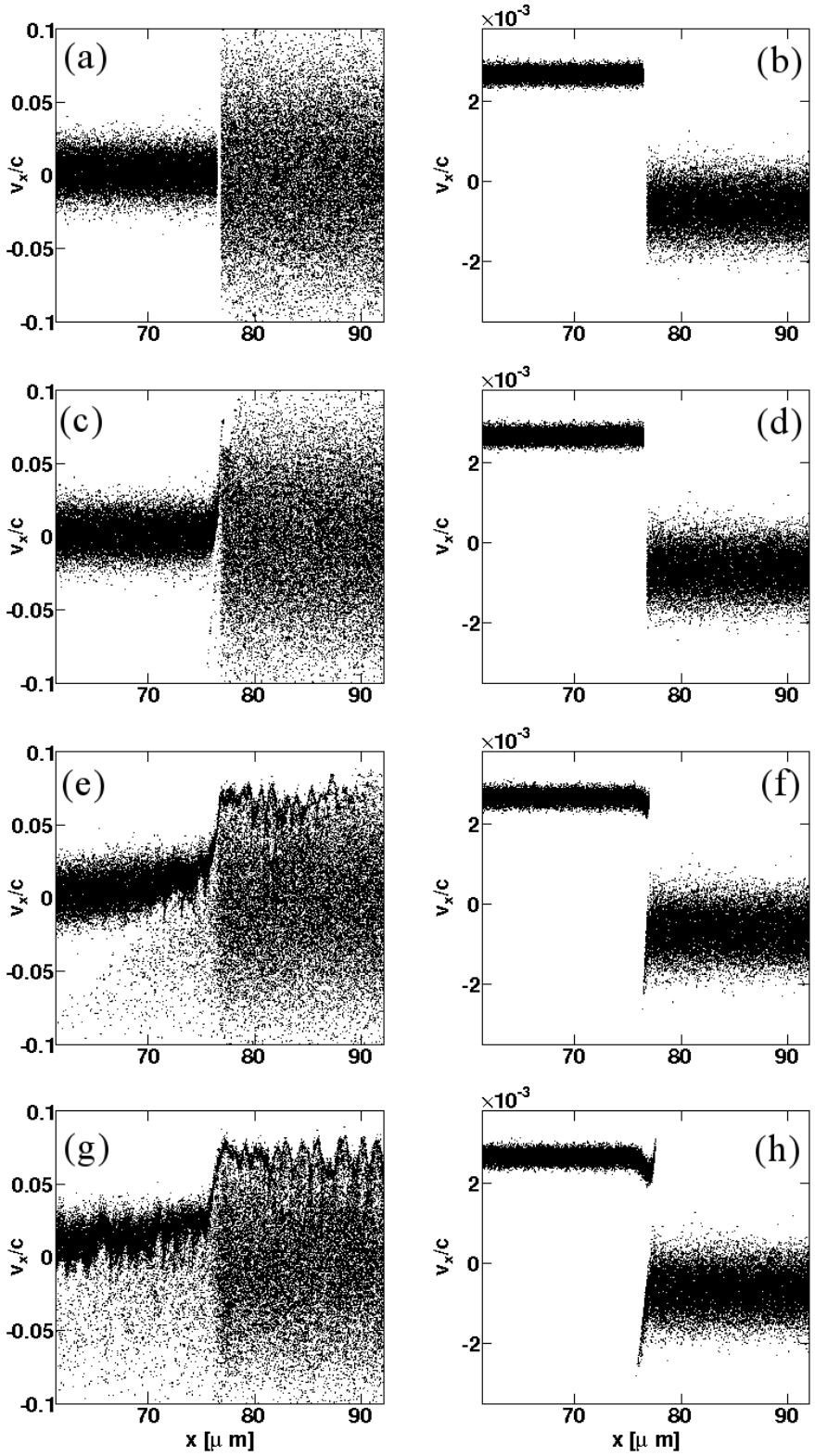

Figure 3.6: The phase-space plots of electrons [(a), (c), (e), and (g)], and of ions [(b), (d), (f), and (h)] at $\omega_{pe}t = 0$, 5, 65, and 135.

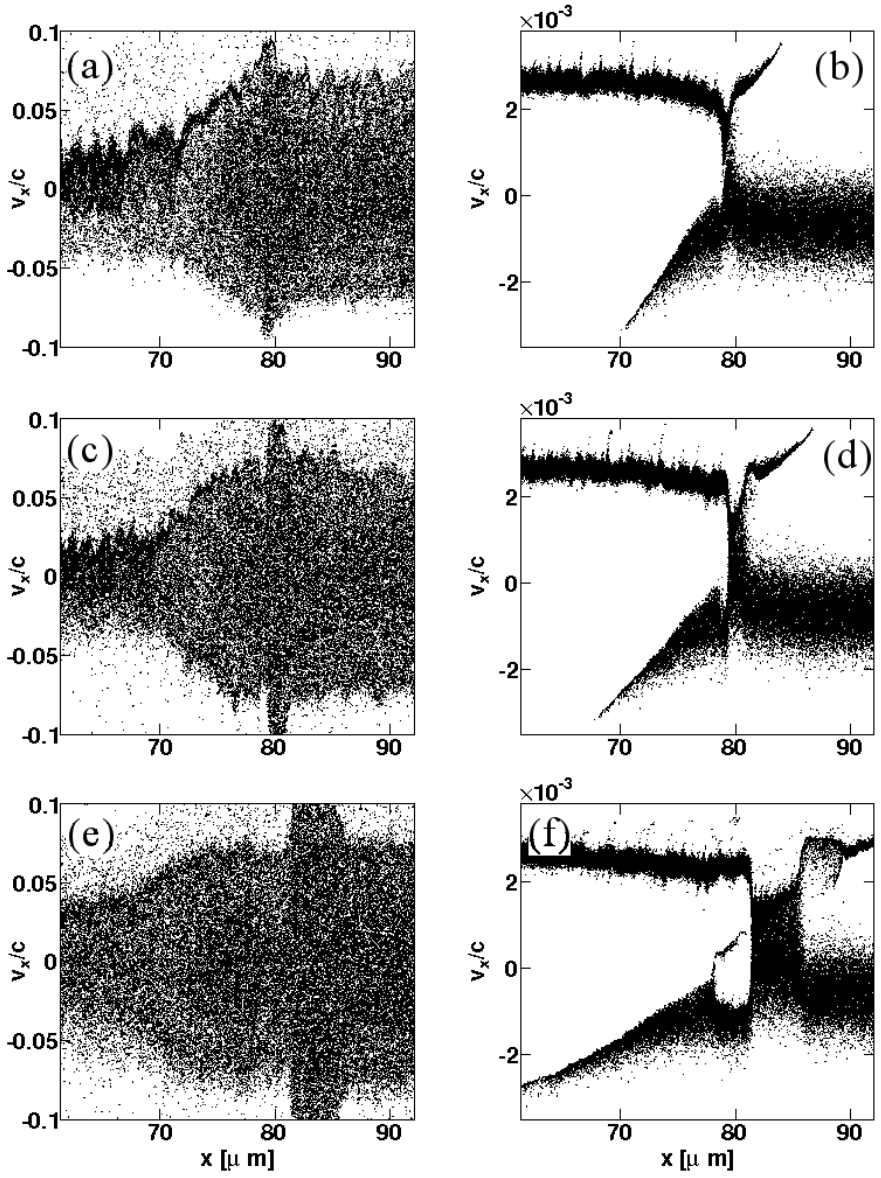

Figure 3.7: The phase-space plots of electrons [(a), (c), and (e)], and of ions [(b), (d), and (f)] at $\omega_{pe}t = 750$, 1000, and 2050, respectively.

and 3.6(b) show the initial velocities of electrons and ions. Early in time at $\omega_{pe}t = 5$ (Figs. 3.6(c) and 3.6(d)), electrons are accelerated by an electrostatic potential at $x \simeq 76$ μm while ions seem to be stable. At $\omega_{pe}t = 65$ (Fig. 3.6(f)), ions are decelerated by the electrostatic potential. At $\omega_{pe}t = 135$ (Fig. 3.6(h)), however, some of the ions are accelerated due to the electrostatic force between accelerated electrons and ions. As time passes, most ions are decelerated and shocks are generated as shown in Figs. 3.7(a)–3.7(f). Some of the decelerated ions are reflected at the shock as shown in Fig. 3.7(d), and these reflected ions and ions with initial velocities from left-side form the counter-streaming condition. Some of the reflected ions are also decelerated in front of the left-side shock as shown in Fig. 3.7(f) at $x \simeq 77$ μm.

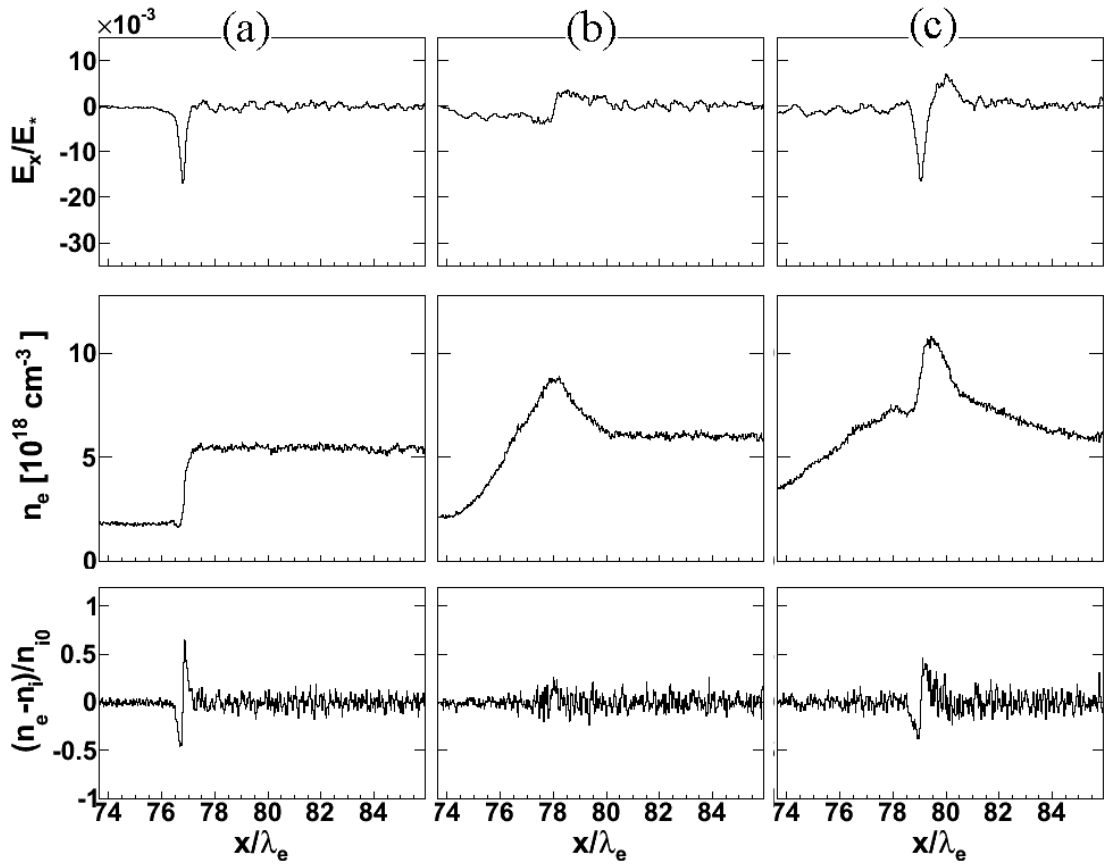

Figure 3.8: The electric field (top), electron density (middle), and the difference between the electron and ion densities (bottom) at (a) $\omega_{\rm pe}t = 25$, (b) 350, and (c) 800.

Figure 3.8 shows the profiles of the electric field E_x/E_*, n_e, and the difference between n_e and n_i (i.e. $(n_\mathrm{e} - n_\mathrm{i})/n_\mathrm{i0}$), where $E_* = c(n_\mathrm{e0} m_\mathrm{e}/\epsilon_0)^{1/2}$ and n_i0 is the initial ion density from the left plasmas, at (a) $\omega_\mathrm{pe} t = 25$, (b) 350, and (c) 800. At the begining of the two-plasma interaction, a large negative ambipolar electric field is generated between electrons and ions in the right-side plasmas as shown in Fig. 3.8(a) since the plasma density is higher in the right-side plasma. As time passes, the electric field becomes small because right-side ions begin to move to negate the charge difference as shown in Fig. 3.8(b). When the initial electric field is sufficiently large, however, ions in left-side plasmas are decelerated by the electric field even if it becomes weak, and it grows as shown in Fig. 3.8(c). As a result, the electric field becomes large to decelerate and reflect ions, and the shocks are generated.

3.4.3 Parameter dependence on shock formation

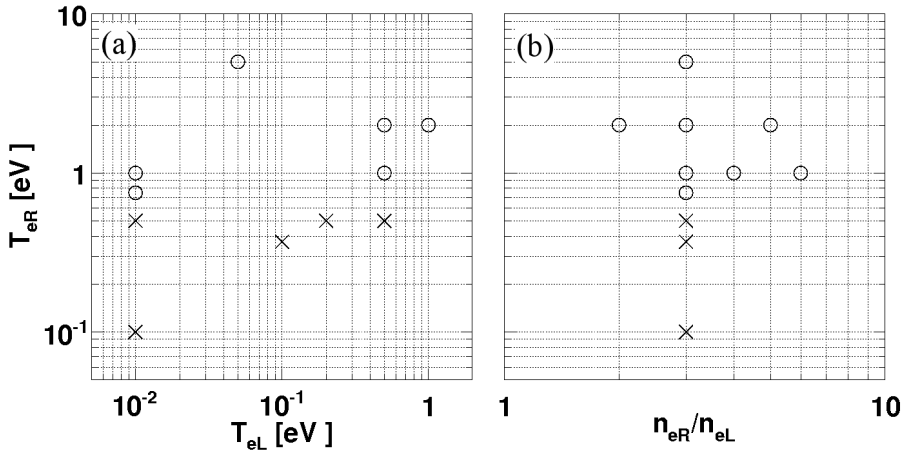

Figure 3.9: Simulation results (a) in various electron temperatures of left– and right–side of a shock, and (b) in various right–side temperatures and density ratios of right–side to left–side. Circles show simulations results in which collisionless shocks were generated, and cross marks show the results in which no shock were generated.

In the previous subsection, we observed the high-Mach number shock formation, however, shock formation mainly depends on the temperature of right plasmas. Figures 3.9(a)

and 3.9(b) show that no collisoinless shocks are generated if the temperature of right–side plasma is low.

The propagation velocity of the left-side shock in the simulation frame is slow compared with the initial flow velocity as discussed in the previous subsection. Other simulations in which shocks are generated show similar results, and this explains that high Mach-number ES shock can be generated when a high-temperature (> 600 eV) plasma flow collides with a low-temperature (~ 10 eV) plasma flow.

3.5 Discussion

The Abel inversion is expressed as the summation of discrete values instead of integral of phase difference; $n_{\rm e}(j) = 1/r_0 \sum_{k=0}^{n-1} a_{jk}(\delta\theta)_k$, where a_{jk} are coefficients, n is the number of pixels in the cylindrical symmetry and r_0 is the radius of symmetry. At the center of the axis of cylindrical symmetry, the noise in the phase accumulate in the summation[57]. Since the phase profile was smoothed before Abel inversion to reduce the noise, the rapid density change became moderate, and the width in Fig. 3.2(e) should be shorter ($W < 100$ μm). In Fig. 3.2(b), the interference fringes suddenly change at $x \simeq 3.1$ mm in 50 μm. In the interferogram, the spatial resolution was defined by the width of the smallest fringes and the resolution of the ICCD camera. Considering the smallest fringe ($\simeq 50$ μm) and the resolution of ICCD camera ($\simeq$ 39–52 μm)[63] including the magnification of our diagnostics ($\simeq 1$), an observed fringe shift of $\simeq 50$ μm was almost the minimum value.

Shock formation in the interaction of two plasmas is commonly observed in space plasmas and also in the universe, for example, co-rotational interaction regions (CIRs), SNRs, and astrophysical jets. ES collisionless shocks have been generated and investigated by PIC simulations using counter-streaming plasmas[38, 64, 31, 34]. Moreover, Sorasio *et al.* reported high Mach-number electrostatic laminar shock formation by the collision of slabs of plasmas with different properties (temperatures, densites). The quasi-one-dimensional

PIC simulation shown in Figs. 3.4(a)–3.4(d) represents an ES shock formation in counter-streaming collisionless plasmas in the similar conditions as the experiment such as the densities and flow velocities. Different from the experiment, the PIC simulation was carried out under idealistic conditions, consequently the density jump of ~ 5 is affected by strongly reflected ions. We think, however, this shock is a strong one and comparable to the experimental density jump quantitatively. Because of the large spacial resolution of IF ($\sim 50\ \mu m$), it is difficult to measure the calculated fine structures of the ES shock, such as the shock width of few μm and the contribution of reflected ions as shown in Fig. 3.4(d). Considering the width of the density jump, the time scale, and the conditions of counter-streaming plasmas in the experiment and the PIC simulation, it is appropriate to regard the density discontinuity in the experiment as a collisionless shock.

It is clear that the two different kinds of shocks are possibly produced in different times from not only the PIC simulation[34], but also the theoretical work[31] in counter-streaming plasmas. One is ES shock and the other is "Weibel-mediated" shock. In the latter case, the dissipation mechanism is provided by the magnetic field generated by the Weibel instability. In order to identify the observed shock wave is different from the Weibel-mediated shock, we have used mainly the difference of the shock widths predicted by the PIC simulation results[34, 30, 32]. The "Weibel-mediated" shock should create filamentary structures in the shock transition region[30] which is not observed in our experiment. The width of density transition region is evaluated as $W \simeq 100c/\omega_{\rm pi}$, where $\omega_{\rm pi}$ is the ion plasma frequency[30]. In the experiment, $c/\omega_{\rm pi}$ is evaluated as $\simeq 110\ \mu$m for $n_{\rm e} = 8\times10^{18}$ cm^{-3}, and $W \simeq 11$ mm which is much larger than the observed structure. In the case of the ES shock, the width of transition region is much shorter than that of "Weibel-mediated" shock, and evaluated as $0.5c/\omega_{\rm pe}$[34]. The electron inertial length $\lambda_{\rm e} = c\omega_{\rm pe}^{-1}$ evaluated from the experiment is $\simeq 2\ \mu$m for $n_{\rm e} = 8 \times 10^{18}$ cm^{-3} which is much smaller than the spatial resolution. The observed shock with the width of $\simeq 50\ \mu$m is not regarded as a

"Weibel-mediated" shock but an ES collisionless shock.

For a shock in a perfect gas, the ratio of the plasma densities is expressed as $n_1/n_0 = v_0/v_1 = (\gamma+1)M^2/((\gamma-1)M^2+2)$, where n_0 (v_0) and n_1 (v_1) are the upstream and downstream density (velocity) under the static system of the shock, respectively[65]. In Fig. 3.2(e), the plasma density at $x > 3.1$ mm ($n_1 \simeq 6.1 \times 10^{18}$ cm^{-3}) is 3–5 times larger than the density at $x < 3.1$ mm ($n_0 \simeq 1.6 \times 10^{18}$ cm^{-3}). In the limiting case of a strong shock ($M \gg 1$), the density ratio is equal to $n_1/n_0 = (\gamma+1)/(\gamma-1) = 4$ with $\gamma = 5/3$ for a monoatomic gas. The experimental result is consistent with the case of the strong shock. If we regard the density jump of $n_1/n_0 = 3.9$ is due to the shock and the effective specific heat ratio $\gamma = 5/3$ is assumed, the Mach-number is very large $M \sim 11$ which is above the prediction of the classical theories for ES shocks.

As shown in quasi-one-dimensional simulations (Fig. 3.4), the high Mach-number ES shocks are created and propagate steadily in counter-streaming flows which have different temperatures and densities. We speculate that the shock is kept steady state due to the pressure balance between the pressure of the ion from the upstream enhanced by the contribution of the reflected ion component and that of the electrostatic field stemming from the high-temperature electrons in the downstream. In Ref. [34], however, two-dimensional PIC simulation shows that the ES shock is destroyed due to the electrostatic ion-ion instability in front of the shock, and much later, the electromagnetic (EM) Weibel instability develops. The time scale of the ES shock disappearance is $\omega_{\rm pe}t \sim 5000$, that is $t \sim 5000/\omega_{\rm pe} \sim 30$ ps in the experiment for $n_{\rm e} = 8 \times 10^{18}$ cm^{-3}. This value is too small compared with the experimental results $t = 5$ or 9 ns. However, when the shock propagates in the plasma whose density is decreasing, like laser-produced plasmas or the surface of SNRs, the strength or energy of the shock increases infinitely[66]. In laser-produced plasmas or ablated plasmas by radiation, the plasma density is not uniform and have a large gradient. The generated ES shock can become stronger and have larger energy propagating in the ablated plasmas

and hence, the shock can be strong and keep steady state such a long time. In a recent paper, a new theory is proposed and it is concluded that a very strong ES shock can be generated when counter-streaming plasma flows with different temperatures and densities interact each other[31]. This is the case of our experiment, and we think we have observed such a strong shock in the present experiment.

3.6 Conclusion

We have reported strong ES collisionless shock generation in high-speed counter-streaming plasma flows without an external magnetic field. A large density jump is observed both in the interferogram and shadowgraph at the same position. The width of the density jump is much shorter than the ion-ion mean-free-path, and hence the measured density jump is a collisionless shock. This shock is not an EM shock but an ES shock because the shock width is much shorter than the prediction of the PIC simulation[30]. This high Mach-number shock can be generated in counter-streaming plasmas that have different temperatures and densities, as shown theoretically in Ref. [31], and numerically by quasi-one-dimensional PIC simulation. The PIC simulation shows that the high Mach-number ES shock is maintained by the balance between the pressure of upstream ions enhanced by reflected ions and that of the electrostatic field stemming from high-temperature electrons in the downstream.

Chapter 4

Temperature measurements in collisionless shock experiments

As we described in section 2.3, the streaked optical pyrometer (SOP) shows the time variation of an one-dimensional brightness distribution through the slit of streak camera, and the gated optical imager (GOI) shows a two-dimensional spacial information of plasma structures. The sensitivities of two detectors are calibrated by different methods, and both detectors show nearly identical brightness temperatures at the same time and position.

In this chapter, we will show the first experimental observation of jet collimation in collisionless counter-streaming plasma flows with shadowgraphy, and evaluate the brightness temperature and electron temperature with the GOI and SOP. Y. Kuramitsu *et al*. reported the observation of jet collimation in counter-streaming plasma flows with shadowgraph techniques[67]. In this chapter, we will estimate the plasma temperatures using optical pyrometers. First, we show the calibration methods of two detectors to determine $T_{\rm b}$ of the laser-produced plasmas, and next, the experimental results which was performed with Gekko-XII HIPER laser system (GXII) at Institute of Laser Engineering, Osaka University. The calibration results of two detectors agree with each other within 20–30 %. After that, we will estimate $T_{\rm e}$ of the laser-produced plasmas in the jet experiments concerning the

bremsstrahlung emission.

4.1 Calibration

To determine the temperature of plasmas produced with a high-power laser system is important[68], in the shock experiments[48, 49, 69, 70, 71] and the jet experiments[67]. A brightness temperature (T_b) is derived by assuming that the brightness of the emission from a plasma at a certain wave length is equal to that of the blackbody radiation at the same wave length as $I_\lambda = B_\lambda(T_b)$, where I_λ is the brightness of the emission and $B_\lambda(T)$ shows the Plank's law. The radiative transfer equation is expressed by absorption (α_λ) and emission (j_λ) coefficients as $dI_\lambda/ds = -\alpha_\lambda I_\lambda + j_\lambda$, where s is the length along the ray. This equation takes simple form using the optical path length $\tau_\lambda = \int_{s_0}^{s} \alpha_\lambda(s')ds'$, $dI_\lambda/d\tau_\lambda = -I_\lambda + S_\lambda$, where the source function S_λ is defined as the ratio of the emission coefficient to the absorption coefficient: $S_\lambda = j_\lambda/\alpha_\lambda$. Assuming that S_λ is constant and the initial intensity $I_\lambda(0) = 0$, above equation can be solved easily as

$$I_\lambda(s) = S_\lambda(1 - e^{-\tau_\lambda}). \tag{4.1}$$

From Kirchhoff's law for thermal emission, the thermal transfer equation is shown as [59]

$$I_\lambda(s) = B_\lambda(1 - e^{-\tau_\lambda}). \tag{4.2}$$

In the case of optically thick plasmas, $\tau_\lambda \gg 1$ and the intensity of brightness is blackbody intensity; $B_\lambda(T_b) = I_\lambda = B_\lambda(T)$ and $T = T_b$. On the other hand, if the plasma is optically thin, $\tau_\lambda \ll 1$, and then $B_\lambda(T_b) = I_\lambda \simeq \tau_\lambda B_\lambda(T)$ and $T \gg T_b$. The absolute intensity of the self-emission from laser-produced plasmas at the wave length of 450 nm was measured with the GOI and SOP. The T_b is calculated from the intensity of the self-emission from

a plasma and, therefore, it is necessary to calibrate the sensitivity of detectors and the transmittance of all optics.

The total energy detected by the detectors in the GXII experiment is estimated by assuming the blackbody radiation from a single-wavelength light, with the Plank function $L(\lambda, T)$, the transmittance of all optics $Tr(\lambda)$, the source size which corresponds to a pixel in the camera Δx, the exposure time Δt, solid angle of a first lens from the target $\Delta\Omega$ and sensitivity of the detector $\eta(\lambda)$,

$$E(T) = \int L(\lambda, T) Tr(\lambda) (\Delta x)^2 \Delta t \Delta\Omega \frac{\eta(\lambda_0)}{\eta(\lambda)} d\lambda, \tag{4.3}$$

where λ_0 is the wavelength of the center of the bandpass filter.

4.1.1 GOI

The relationships between an incident energy and digital outputs of the GOI or SOP are calibrated. After the calibration, the energy can be derived from the digital outputs of the detectors, and also can be converted to $T_{\rm b}$.

The ICCD camera (DH734, Andor) was used as the GOI and calibrated using a standard lamp (CL6_H, Bentham). This lamp was pre-calibrated at a certain distance from the light source. Figure 4.1 shows the setup for the calibration of the GOI. We measured the digital output of the ICCD camera by changing the distance between the lamp and the camera. l_0 is the position of virtual light source assuming that the light is coming from a point source considering the spread angle. l_1 is the pre-calibrated position and l_2 is the surface of cathode of the ICCD camera. Using l_0, l_1, l_2, and calibrated energy density measured at $l = l_1$, the energy density at $l = l_2$ is calculated as $E_2 = E_1(l_1 - l_0)^2/(l_2 - l_0)^2$. Figure 4.2 shows the obtained relation between input energy and output counts. The result shows good linearity up to 8×10^8 counts ($\sim$ 2000 counts / pixel) which are enough to apply to

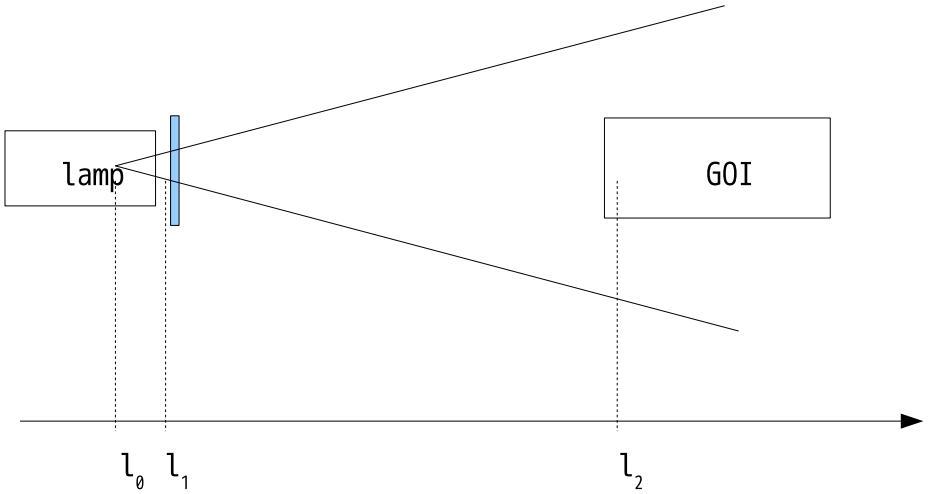

Figure 4.1: Calibration setup of the GOI. l_0 is virtual light source position calculated back from the spread angle of light, l_1 is the pre-calibrated position, and l_2 is the position of the cathode in the GOI.

the experimental data which is within 100–400 counts.

4.1.2 SOP

Figure 4.3(a) shows the calibration setup for the SOP. A Picosecond Laser Pulser (PLP-10, Hamamatsu) was used as a short-pulse light source and the emitted light was focused through two lenses on the slit of the streak camera (SOP) and an energy probe (RjP-465, Laser Probe Inc.). Figure 4.3(b) shows the CCD image taken by the streak camera. The vertical axis shows the time ($\sim$ 30 ns / 1024 pixels), and the horizontal axis shows the spacial position on the slit in front of the streak camera. Figures 4.3(c) and 4.3(d) show the integrated profiles on x– and y–axis, respectively. Integrating signals in Fig. 4.3(a), total digital counts can be obtained. To determine the real signal, we separated the total CCD image into two regions: “signal region” and “background region”. “signal region” is the region that contains signal of light pulse nearly at the center of the CCD. The expected

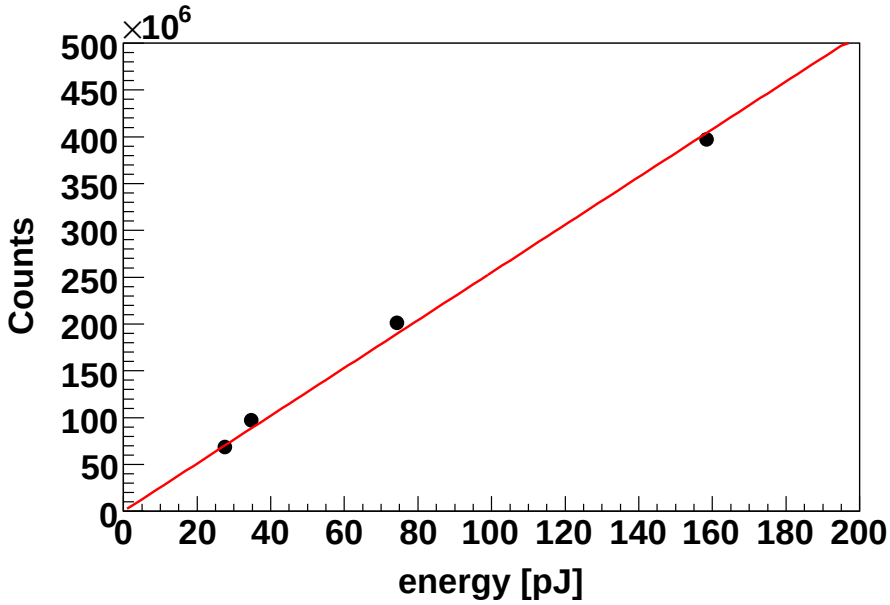

Figure 4.2: The relationship between input energy and output counts. The typical statistical errors are 2.3 % in the energies and 0.12 % in the counts.

signal position s_x and s_y were calculated by following formula

$$s_{x_i} = \frac{\sum_i x_i C(x_i)}{\sum_i C(x_i)}, \tag{4.4}$$

where x_i represents x or y, and $C(x_i)$ is the digital counts obtained at position x_i in Fig. 4.5(a). The signal region is defined by the distribution of Figs. 4.5(b) as $s_{x_i} - 5\sigma_{x_i} \leq x_i \leq s_{x_i} + 5\sigma_{x_i}$, where σ_{x_i} is the standard deviation of the distribution of Figs. 4.5(a) and 4.5(b),

$$\sigma^2_{x_i} = \frac{\sum_i (x_i - s_{x_i})^2 C(x_i)}{\sum_i C(x_i)}. \tag{4.5}$$

The "background region" is the whole region which excludes the "signal region". The average signal in a pixel $C_{\mathrm{avr,bk}}$ is estimated by taking average in the "background region"

$$C_{\mathrm{avr,bk}} = \frac{\sum_{\mathrm{background}} C(x,y)}{\sum_{\mathrm{background}} 1}, \tag{4.6}$$

and the estimated signal is obtained with $C_{\rm avr,bk}$ by integrating in the "signal region"

$$C_{\rm sig} = \sum_{\rm signal} (C(x,y) - C_{\rm avr,bk}). \tag{4.7}$$

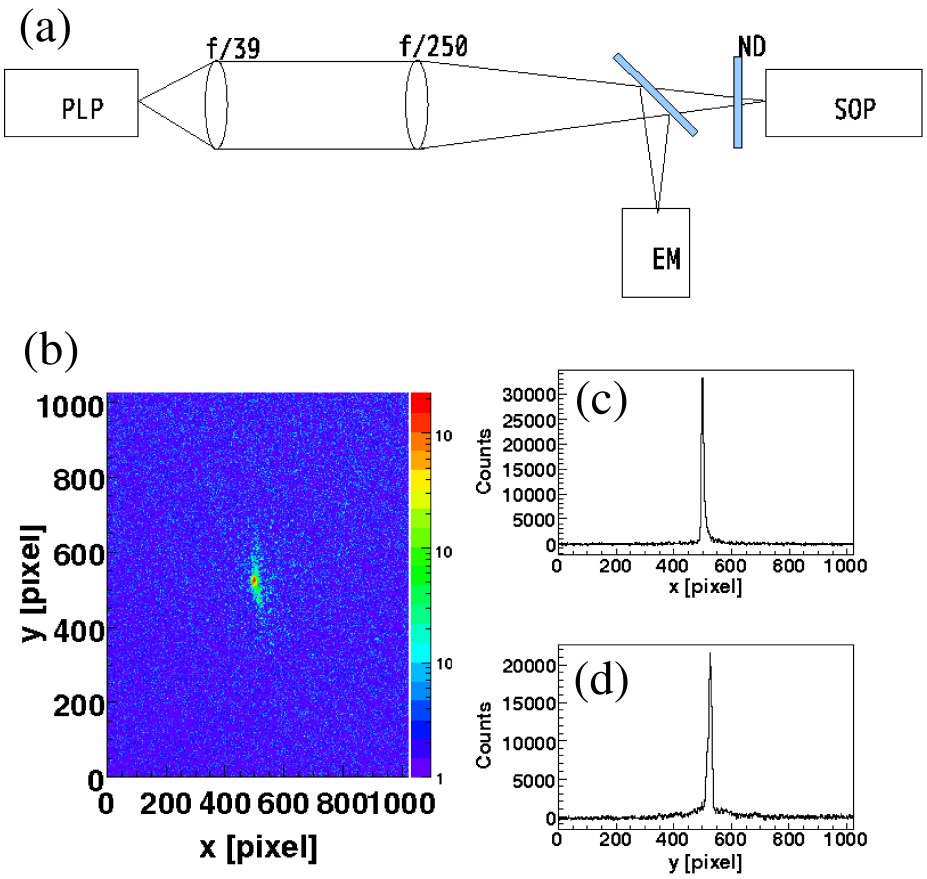

Figure 4.3: (a) The experimental setup for the calibration of the SOP. A light pulse was used as a light source, and about the half of total energy was detected by the energy probe. (b) The example of a CCD image of the streak camera. The vertical axis shows the time ($\sim$ 30 ns in 1024 pixels), and the horizontal axis shows the spacial position in the slit in front of the streak camera. The integrated profiles along (c) x axis and (d) y axis, respectively.

In the calibration of the SOP, we used the light pulse which has a single-wavelength ($\sim$ 672 nm). In the GXII experiment, the plasma self-emission is, however, detected at $\sim$ 450

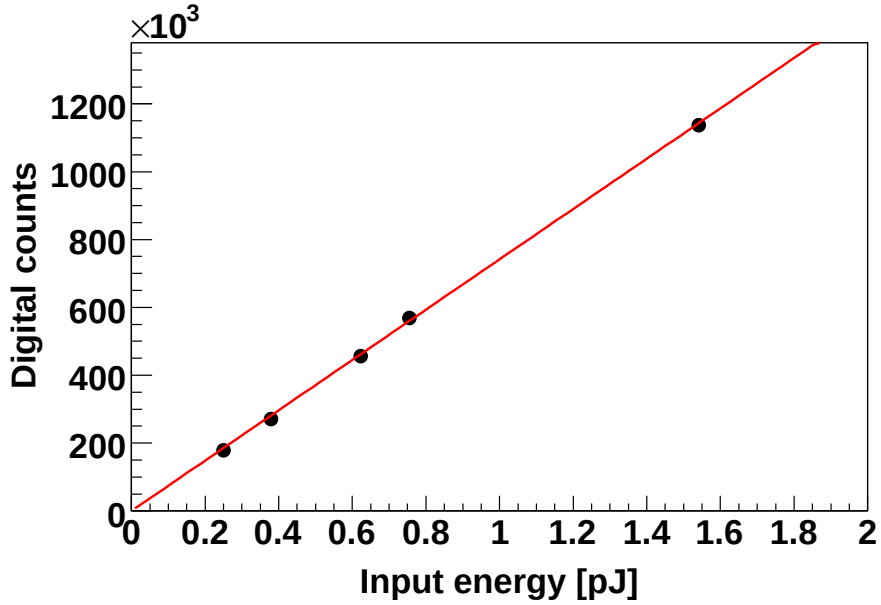

Figure 4.4: The relation between the input enegy and the output digital counts. The typical statistical errors are 0.33 % in the energies and 1 % in the counts, respectively.

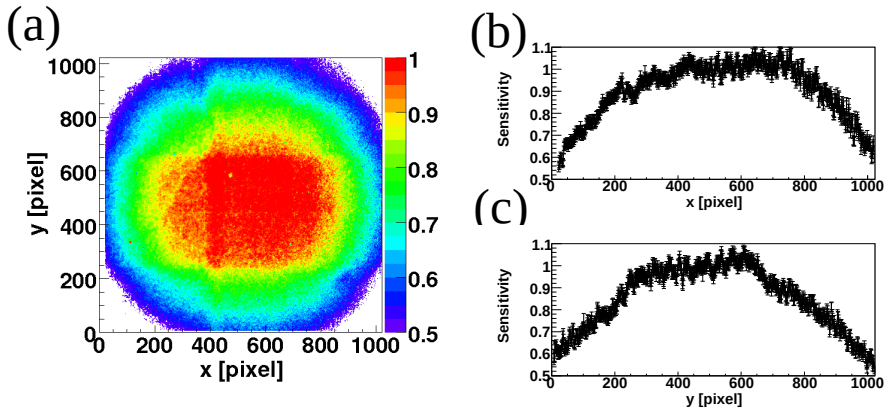

Figure 4.5: (a) The image of the uniform light. The profiles at the center of Fig. 4.5(a) along (b) x axis and (c) y axis.

nm wavelength (λ_0 in equation (4.3)), and the digital counts $C(x_i)$ is corrected as

$$C_{\rm crr}(x_i) = C(x_i) \cdot \frac{\eta(\lambda_0)}{\eta(\lambda_1)}, \tag{4.8}$$

where η is the sensitivity of the SOP, λ_0 is the wavelength of the center of the bandpass filter, and λ_0 is the wavelength of the PLP.

Figure 4.4 shows the relation between the input energy of the estimated signals and the digital counts which is obtained by the streak camera assuming $\lambda = \lambda_0$. The linearity is satisfied up to 1.1×10^6 counts ($\sim$ 1400 counts / pixel). This value is larger than typical experimental values $\sim$ 100–500 counts / pixel.

Moreover, the sensitivity of the CCD camera in the streak camera is not uniform; at the edge of the CCD camera it decreases to less than 50 % of that at the center. This non-uniformity was measured with a Xe lamp which has an uniform spacial distribution. Figure 4.5(a) shows the contour of the CCD image of the spacially uniform lamp. Figures 4.5(b) and 4.5(c) show the projections on x– and y– axis, respectively. They show that the sensitivity at the edge of the cathode of the CCD camera decreases rapidly. This effects mainly results from the lense between "Streak tube" which consists of photo-cathode, deflection plates to apply the sweeping voltage, and phosphor screen, and the CCD camera.

4.2 Application to GXII experiment

The jet formation experiment was performed with GXII HIPER laser system. Figure 4.6(a) shows the schematic view of the target. Our target consists of two thin plastic (CH) foils which have the thickness of 10 and 60 μm, respectively. They are separated by 4.5 mm and 10 μm-foil (first foil) is irradiated by laser pulses to create plasma flows at the rear-surface of the first foil. The other foil (second foil) is ablated by the radiation from the plasma and/or laser pulses which transmit an underdense plasmas created around the first

foil. The plasmas are created by four laser pulses of energy $\sim$ 120 J/pulse, wave length 351 nm, pulse width 500 ps in FWHM, and spot size of 300 μm diameter in each pulse. The radiation of the created plasma at the rear-surface of the first foil ablate the second foil, resulting in the formation of counter-streaming plasma flows between two foils. Figure 4.6(b) shows the top view of optical diagnostics. The plasmas are diagnosed by a probe laser with the shadowgraphy, interferometry and streaked interferometry, and self-emission measurements with the SOP and GOI.

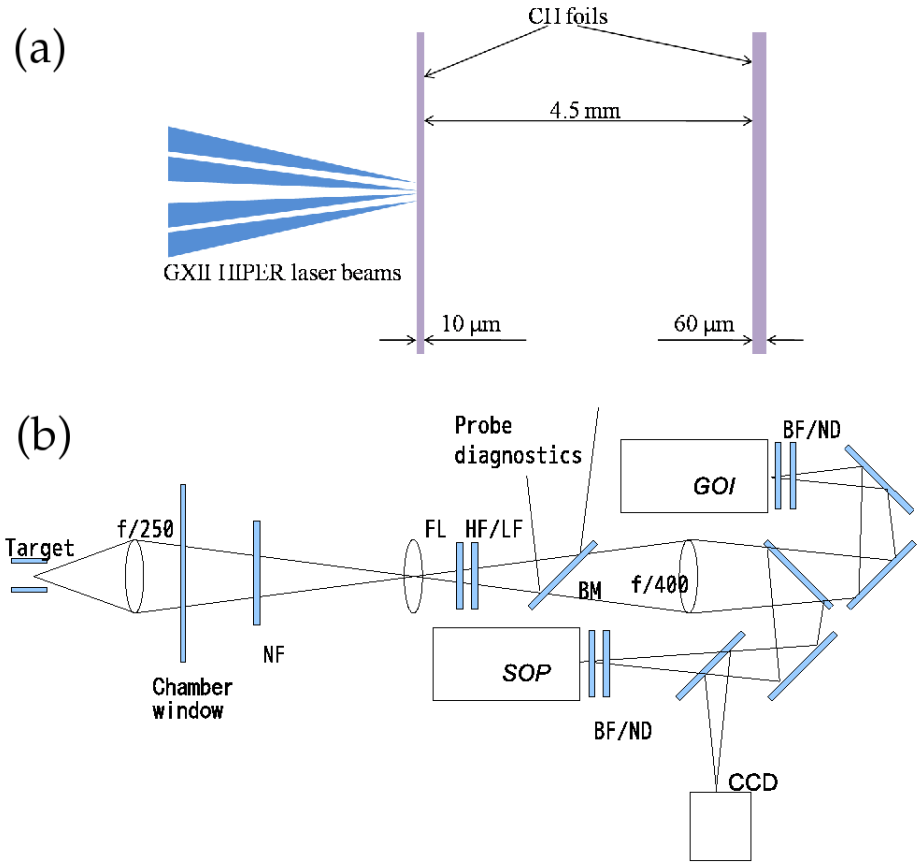

Figure 4.6: (a) Schematic view of the target design. The target consists of two CH foils, and one side of the CH foils is irradiated by the laser pulse. (b) The Top view of the experimental optics. There are two kinds of diagnostics; one is probe diagnostics such as shadowgraphy, interferometry, and streaked interferometry, and the other is the self-emission measurement which includes the SOP and GOI.

Band-pass filters were placed in front of the detectors to measure the intensity of an

emission in a certain wave length; in our experiment, the band-pass filters which have 450 nm central wavelength were used.

It is necessary for the calculation of $T_{\rm b}$ to calibrate the detectors and also to measure the transmittance of all optics. In following section, we will show the transmittance measurements and calculation of $T_{\rm b}$.

4.2.1 Transmittance of optics

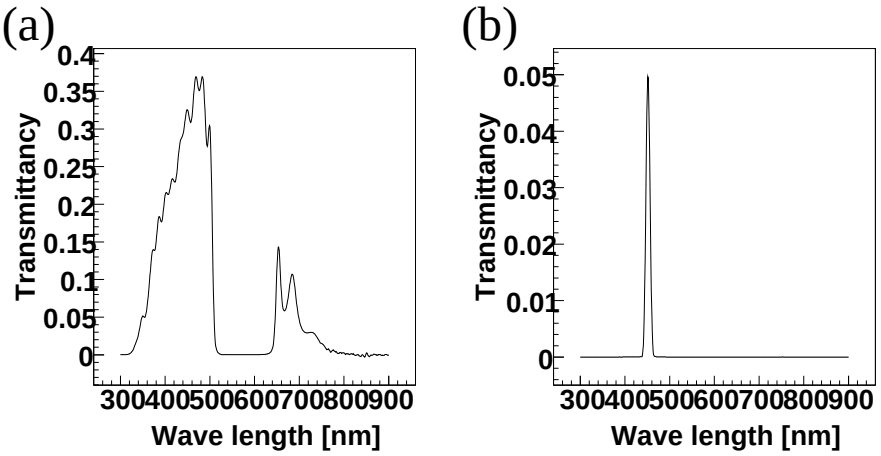

Figure 4.7: (a) Transmittance of a chamber window, super notch filter, and high– and low–pass filters, and (b) that of optics shown in Fig. 4.7 and a band-pass filter.

The transmittances of chamber window, super notch filter, and high– and low–pass filters are measured with a spectral photometer (HITACHI, U4100). Figure 4.7(a) shows the transmittance of the optics including chamber window made of quartz glass, super notch filter, and high– and low–pass filters to cut the main laser pulse (ω, 3ω). Figure 4.7(b) shows the transmittance of of the band-pass filter (SIGMA KOKI, VPF-25C-10-45-45000) and the optics which is shown in Fig. 4.7(a). The transmittances of lenses are measured with the PLP and energy probe, and the reflectivity of all aluminum mirrors (TFAN, SIGMA KOKI) are assumed as ~ 92 %.

The relationship between $E(T_{\rm b})$ and $T_{\rm b}$ in equation (4.3) is shown in Figure 4.8. The

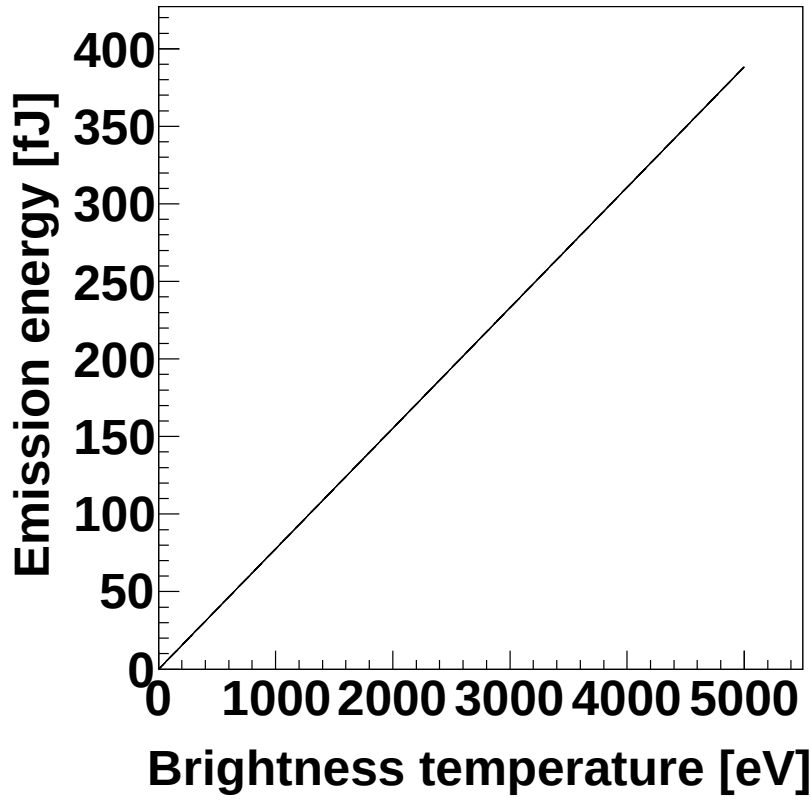

Figure 4.8: The relationship between $E(T_b)$ and T_b in equation(4.3)

emission energies are nearly proportional to the brightness temperatures.

4.2.2 Brightness temperatures

Figures 4.9(a) and 4.9(b) show the profiles of $T_{\rm b}$ after the calibration of the GOI and SOP, respectively. Both results are consistent within 30 % accuracy and they show very similar profiles. Figure 4.9(a) is taken at $t = 25$ ns from laser irradiation. The position of the slit in front of the streak camera is shown in Fig. 4.9(a) with white line. Four lasers irradiate the first foil at $(x, y) = (1.5\ \text{mm}, 3.6\ \text{mm})$ from the left side. Figure 4.9(b) shows the time evolution of the self-emission at the slit position. The vertical axis shows the time after the main laser and the horizontal axis shows the slit region. This figure represents that the

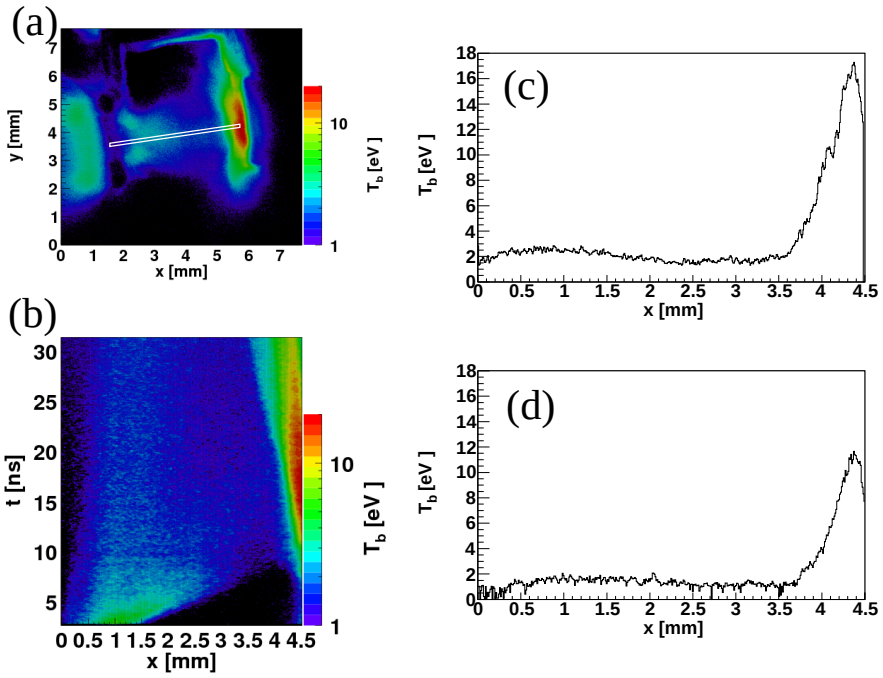

Figure 4.9: The brightness temperature T_b of (a) the GOI and (b) SOP, and the profiles at $t = 25$ ns of (c) the GOI and (d) SOP. The white line in Fig. 4.9(a) shows the slit position where the SOP is measured. The positions $x = 0$ and 4.5 in Fig. 4.9(b) show those of the target surfaces. Figure 4.9(a) and 4.9(b) are taken in the same shot, and 4.9(c) and 4.9(d) show the same timing at the same position. The difference in T_b between two detectors is within 20–30 %.

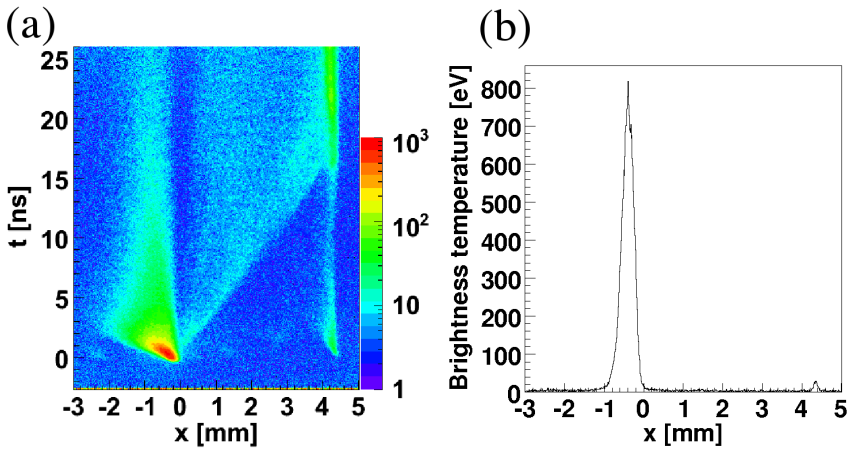

Figure 4.10: (a) The time variation of T_b obtained by the SOP, and (b) the profiles at $t = 0.5$ ns.

counter-streaming plasma flows are created between two foils when one side of the foils is irradiated by a laser pulse. The other foil is ionized by the radiation from the expanding plasma at the first foil almost at the same time as the first foil.

Figure 4.10(a) shows the time variation of $T_{\rm b}$, and Figure 4.10(b) shows the profile which shows the maximum brightness in Fig. 4.10(a) at $t = 0.5$ ns. The maximum value of $T_{\rm b}$ is ~ 800 eV at the laser timing near the surface of the first-foil. Using a flux-limited heat transport model, we can estimate the electron heat flux as $f n_{\rm e} T_{\rm e} \sqrt{T_{\rm e}/m_{\rm e}}$, where $m_{\rm e}$, $n_{\rm e}$, $T_{\rm e}$ are the electron mass, number density, and temperature, respectively. Assuming the half energy is absorbed at lower density than critical, and the rest half energy is absorbed at the critical surface, the electron temperature is evaluated as $T_{\rm e} \sim 1$ keV using the following formula:

$$I/2 = f n_{\rm e} T_{\rm e} \sqrt{T_{\rm e}/m_{\rm e}}, \tag{4.9}$$

where I is the laser intensity, and $m_{\rm e}$ is the electron mass. The derived $T_{\rm b} \sim 800$ eV is more or less the same as rough evaluation of $T_{\rm e} \sim 1$ keV from equation (4.9), and during the laser irradiation, the temperature of plasmas near the critical surface is equal to the brightness temperature.

4.3 Temperature estimation in shock experiment

The SOP and GOI are normally used in optically thick plasmas and these plasmas are regarded as blackbody or greybody radiator. However, in our experiment, the plasma density between two foils is optically thin, because the probe beam coming from the transverse direction of the plasma expansion can be detected in interferometric and shadowgraph diagnostics through the plasmas. In even optically thin plasmas, however, optical pyrometer systems are important because they depend on the electron density and temperature.

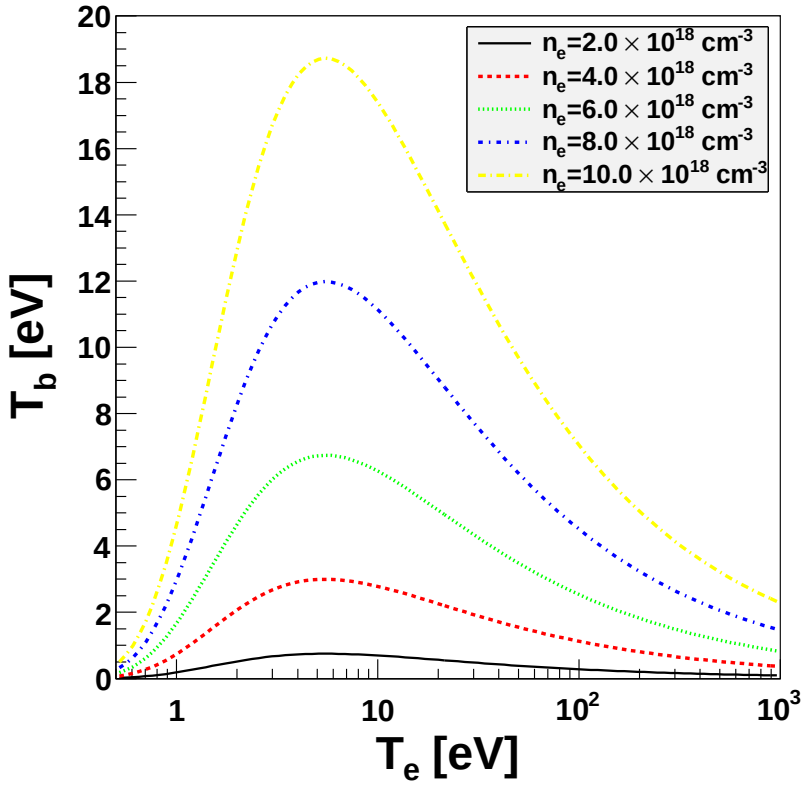

Figure 4.11: The brightness temperatures assuming the bremsstrahlung emission with the plasma size of 1 mm in various electron densities.

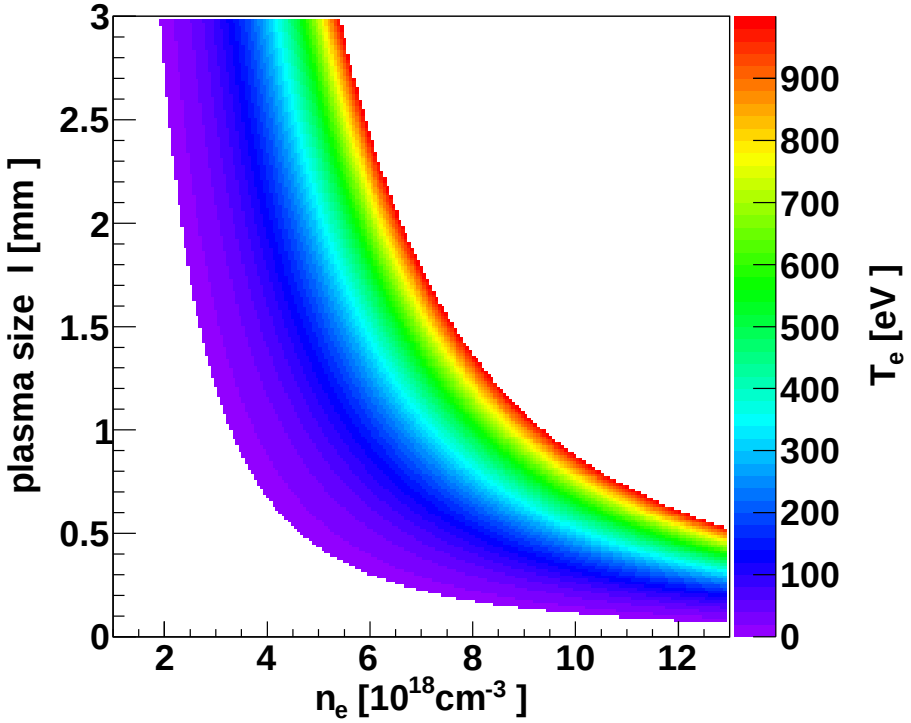

Figure 4.12: Electron temperatures for various values of $n_{\rm e}$ and plasma size in the case of $T_{\rm b} = 2$ eV. In the white region, $T_{\rm b}$ is not expressed by bremsstrahlung emission. The highest $T_{\rm e}$ is set to 1 keV because of the measurable highest brightness temperature ~ 800 eV and the evaluation of the electron temperature ~ 1 keV from flux-limited model.

In optically thin plasmas, $T_{\rm e}$ is much larger than $T_{\rm b}$, and the emission intensity is evaluated by bremsstrahlung emission as below[59] in CGS unit:

$$\epsilon_\lambda^{ff} = \frac{dW}{d\lambda dt dV} = \frac{32\pi e^6}{3mc^2\lambda^2}\sqrt{\frac{2\pi}{3m}}\frac{Z n_{\rm e}^2 e^{-hc/\lambda T_{\rm e}}}{\sqrt{T_{\rm e}}} g_{ff}, \tag{4.10}$$

where ϵ_λ^{ff} is the bremsstrahlung emission per wavelength per unit time per volume, Z is the degree of ionization, h is the Planck constant, $T_{\rm e}$ is the electron temperature in eV unit, and $g_{ff} \sim 1$ is the gaunt factor. Defining the wave length with a band pass filter, ϵ_λ^{ff} depends on the electron density and temperature. The electron density can be measured by the interferometry and the measurable density is about 1×10^{18}–1×10^{19} cm^{-3}. Assuming the electron density $n_{\rm e} = 4 \times 10^{18}$ cm^{-3} and plasma size of 0.1 cm (transverse to the plasma

expansion), the electron temperature can be evaluated using Fig. 4.11 as $T_{\rm e} = 2$ eV for optically thick plasmas, and $T_{\rm e} = 20$ eV for optically thin plasmas. Figure 4.12 shows the electron temperatures with the various plasma sizes and the electron temperatures. In white region at left below, the self-emission intensity can not be explained by bremsstrahlung emission using these parameters, and upper-right region shows the electron temperature which is larger than 1 keV.

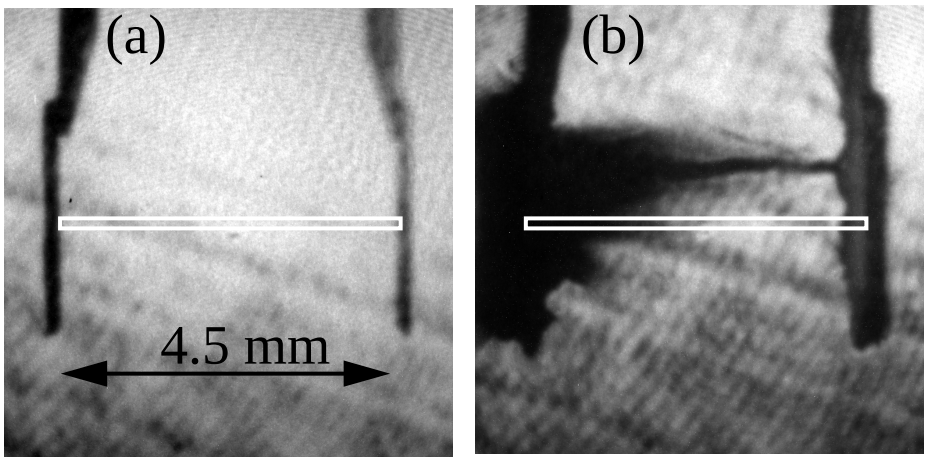

Figure 4.13: The shadowgraphs which are taken (a) before and (b) $t = 15$ ns after the target irradiation with main laser.

Figures 4.13(a) and 4.13(b) show the shadowgraph images obtained before the laser shot and $t = 15.5$ ns later, respectively. The left foil (first foil) was irradiated by four laser beams and the plasma (first plasma) was created at the rear-side of the first foil. The right foil (second foil) was ionized by the radiation from the first plasma, and the plasma which has low density and temperature was created. In counter-streaming plasmas between two foils, the first plasma was collimated because of the existence of an ambient low-density plasma from the second foil. On the other hand, when the single foil was irradiated, no plasma collimation was observed (not shown). This indicates that the collisionless counter-streaming plasma is essential for the plasma jet collimation.

The plasma collimation was observed at $t = 15.5$ ns, and it is also measured by the SOP.

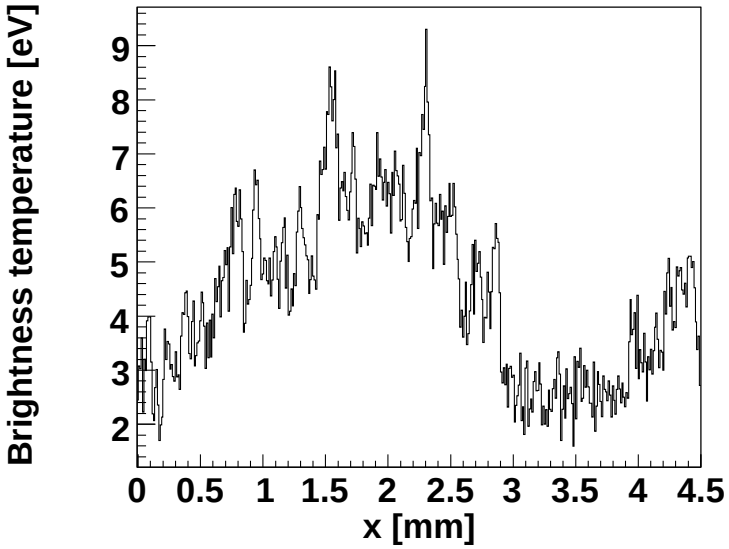

Figure 4.14: The brightness temperatures at $t = 15.5$ ns measured with the SOP. The position $x = 0$ mm is the target surface of the first foil, and $x = 4.5$ mm is the surface of the second foil. The expanding plasma from the first foil has the brightness temperature of ~ 6 eV.

The profile of the brightness temperature is shown in Fig. 4.14. The brightness temperature of the first plasma is ~ 6 eV at $x = 2$ mm, and that of the plasma from the second foil is ~ 2 eV at $x = 3$ mm in counter-streaming plasmas. Assuming the bremsstrahlung emission, the electron temperature at the position $x = 2$ mm is evaluated as $T_{\rm e} = 70$ eV for the plasma size $l = 2$ mm and the electron density $n_{\rm e} = 6 \times 10^{18}$ cm^{-3}, and $T_{\rm e} = 10$ eV for $l = 1$ mm and $n_{\rm e} = 6 \times 10^{18}$ cm^{-3}.

Using the evaluated values of the electron temperature $T_{\rm e} = 70$ eV, the counter-streaming plasma velocity $v_1 = 4.5{\rm mm}/15.5{\rm ns} = 290$ km/s, and the electron density $n_{\rm e} = 6 \times 10^{18}$ cm^{-3}, the ion-ion mean-free-path is calculated as $\lambda_{\rm ii} = 0.5$ mm. This value is less than the scale of our target ~ 4.5 mm, however, this is much larger than the size of the density or temperature changes which are a few hundreds micron. The counter-streaming plasmas are collisionless, and these collisionless plasmas can cause the collimation of the plasma jet.

4.4 Conclusion

We have reported the plasma jet collimation in collisionless counter-streaming plasmas with the shadowgraphy and self-emission measurements. Two self-emission diagnostics (the GOI and SOP) were calibrated with different methods and the results of the brightness temperatures were consistent within 30 %. From the shadowgraphy, the collimation of the plasma jet was observed and the plasma temperatures near the collimating plasma was evaluated by the SOP.

Chapter 5

Collisionless shock associated with plasma jet

5.1 Introduction

Jets in the universe are well collimated as observed in Young stellar bojects (YSOs), in young stellar systems, active galactic nuclei (AGNs), galactic black holes, and gamma-ray bursts (GRBs). The physical mechanisms of jet formations and collimations are, however, not well understood. A lot of studies to investigate such phenomena have been performed theoretically, numerically, and observationally; for example, effects of an ambient medium[72], radiative cooling of a jet[73], presence of an external magnetic field[74], and dynamics of jet propagation in interstellar medium[75]. A high Mach-number jet which propagates into an ambient gas or plasma generates a bow shock as a forward shock in the ambient media, and a reverse shock or rarefaction wave opposite to the propagating jet. This jet is separated from the ambient media by a contact discontinuity, which suppresses transverse expansion of the jet and collimates the jet for a long distance.

Kuramitsu *et al*. have studied plasma jet collimation in counter-streaming plasmas.[67] They suggest that a collisionless shock is one of the possible causes for observed jet con-

finement. However, no clear experimental evidence in favor of this is presented, and the formation of shocks within the experiment is not investigated.

In this chapter we discuss the formation of a collisioless shock within the experiment, showing time evolution data which makes clear the formation of a shock discontinuity within the plasma. The experimental conditions for the generation of the counter-streaming plasmas are given in [67]. A shock is observed in the counter-streaming plasmas, while no shock is observed without a counter flow: It is clarified that the counter-streaming interaction is essential for the generation of a shock. The shock formation is confirmed by the time evolution of self-emission measurements, in which a sudden emission change is observed in space and time. The relative velocity of counter-streaming plasmas is so high that their interaction can be regarded as collisionless and the created shock is a collisionless shock. The formation of the collisionless shock is speculated to generate the effective pressure through the electrostatic field so as to prevent the transverse expansion of the jet produced in the same time.

5.2 Experiment

The experiments were performed with the Gekko-XII (GXII) HIPER laser system at Osaka University, frequency tripled Nd:Glass laser (351 nm) which have the energy of ~ 120 J / beam in 500 ps pulse duration. The focal spot diameter was 300 μm, and four laser beams were focused on a surface of target with a separation of 100–250 μm between each beam to make a inhomogeneous density profile in the plasma flow.

We used two kinds of targets: One is double-plane target that consists of two CH foils which have the thicknesses of 10 μm and 60 μm, and the other is single-plane target that consists of only one 10 μm thick foil. Figure 5.1 shows the schematic view of the double-plane target. Four laser beams were focused on the 10 μm thick foil (first foil) and plasma flows were created at the rear-side of the first foil. The second foil was also ablated by

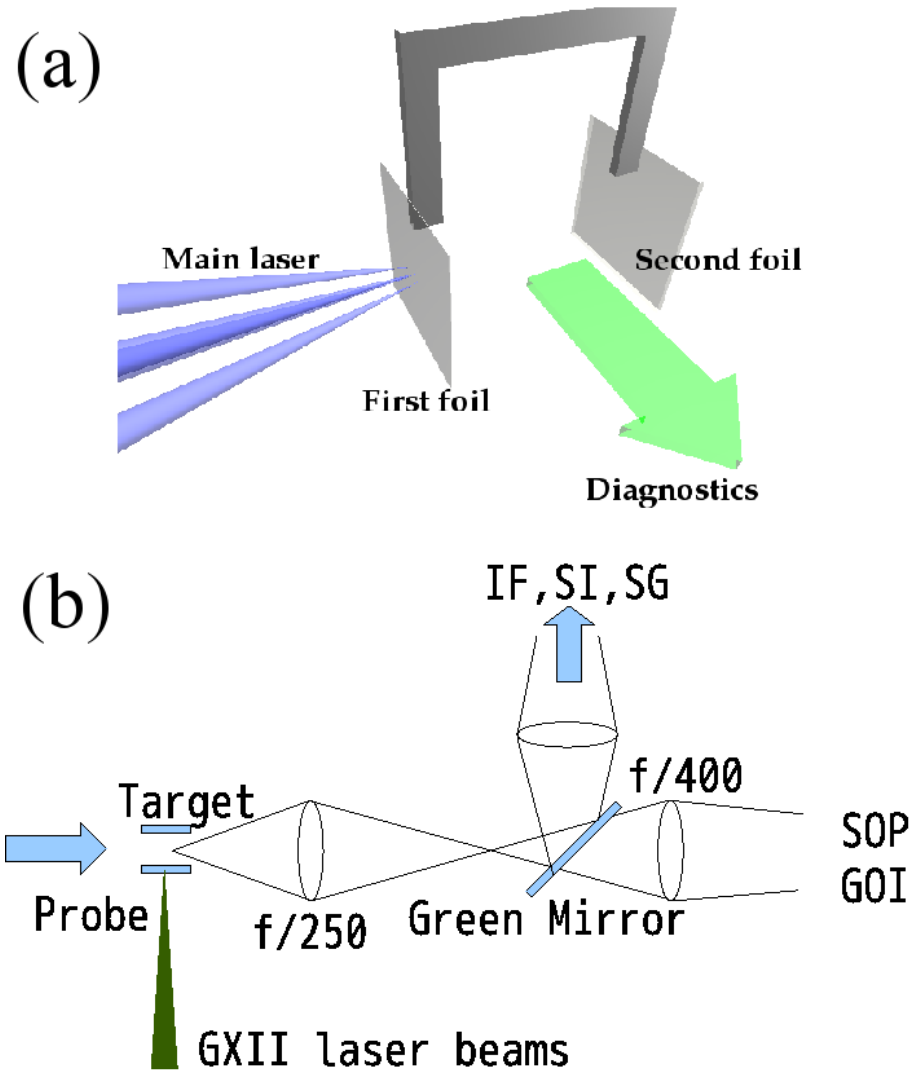

Figure 5.1: (a) A schematic view of double-plane target. We used two kinds of targets. One is double-plane target that consists of two foils which have 10 μm and 60 μm thickness, and the other is single-plane target that consists of only one plane of 10 μm thickness. (b) The Top view of the experimental optics. The probe diagnostics are measured by interferometry (IF), streaked interferometry (SI) and shadowgraphy (SG). The self-emission was measured by a streaked optical pyrometer (SOP) and a gated optical imager (GOI).

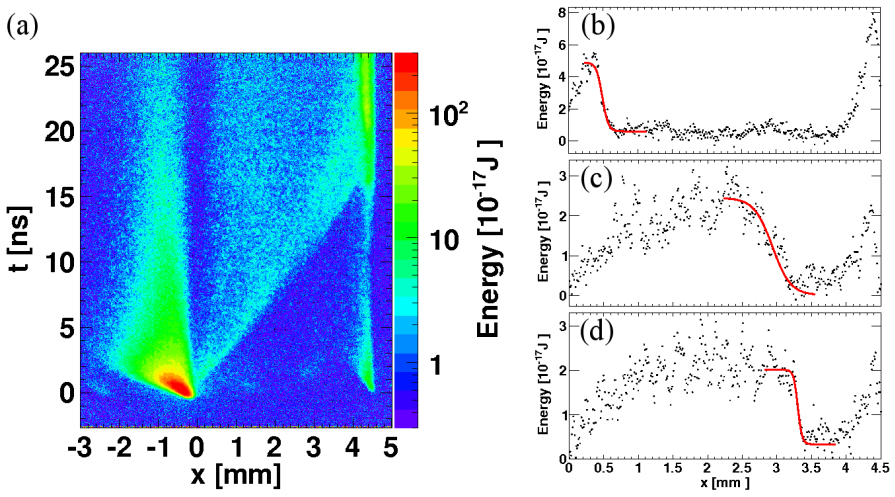

Figure 5.2: (a) The emission energy obtained by the SOP. The vertical axis shows the time variation after laser irradiation and the horizontal axis shows the distance between two foils. The profiles of the emission energy obtained at (b) $t = 2.0$, (c) 11.0, and (d) 12.1 ns after laser pulses, respectively.

the radiation from the plasma of the first foil. As a result, the counter-streaming plasmas were created between the two foils. The single-plane target has only the first foil, and no counter-streaming plasmas were created in this target.

Plasma expansion and shock formation were observed from the transverse to the plasma expanding direction. Self-emission was measured by a streaked optical pyrometer (SOP) and a gated optical imager (GOI). The electron density and the phase difference are measured by an interferometry (IF) and a streaked interferometry (SI). We measured the emission energy from the created plasmas with the SOP and GOI with a bandpass filter which has the central wavelength of 450 nm.[76] The GOI shows the two-dimensional images of the emission energy and the SOP gives the time variation of the one-dimensional emission energy. We used Nomarski interferometry to measure the electron density. The electron density profile was calculated by the IF, and the time variation of the one-dimensional interference images was measured by the SI. A probe laser was a frequency doubled Nd:YAG laser (532 nm) with a pulse width of ~ 14 ns. The gate widths of the ICCD cameras for IF

and shadowgraphy (SG) were 250 ps, and that for the GOI was 1.6 ns.

5.3 Results and Discussion

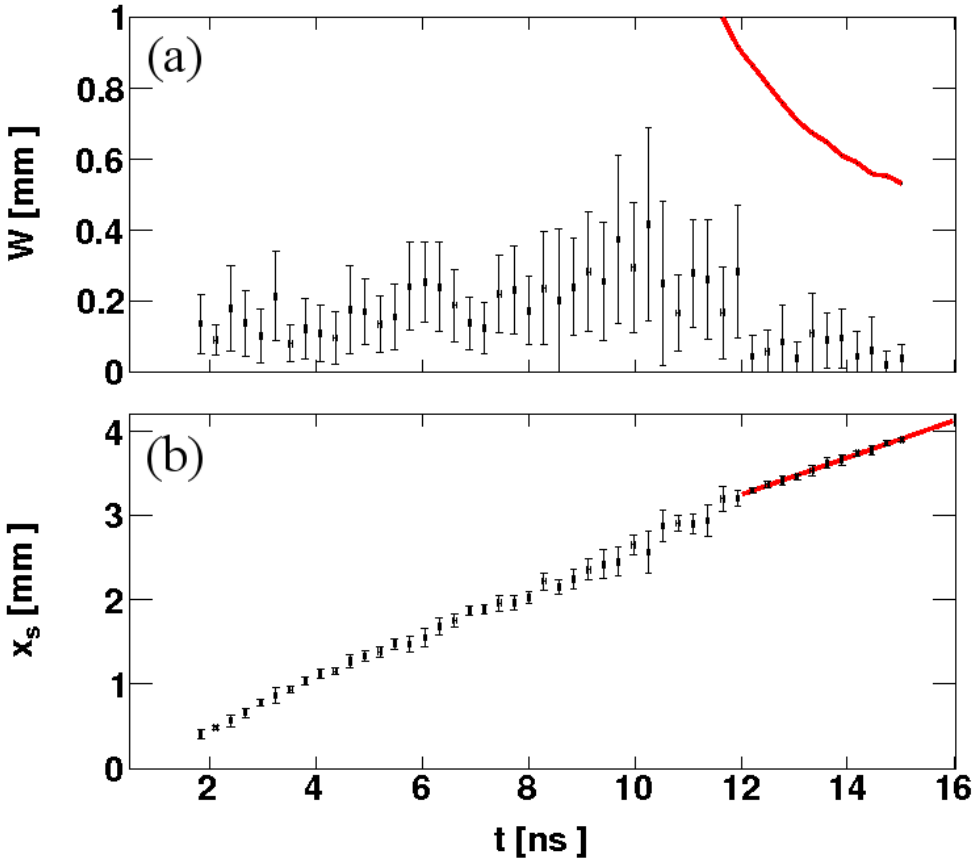

Figure 5.3: The time evolution of (a) the evaluated transition width W (dots with error bars) and (b) the positions of transition and shock $x_{\rm s}$ ($t > 12$ ns) evaluated by fitting the energy profiles with equation (5.1). The red line in (a) shows the calculated ion-ion mean-free-path ($\lambda_{\rm ii}$) assuming the maximum calculable electron density $n_{\rm e} \sim 1 \times 10^{19}$ cm^{-3}. The red line in (b) is the result of linear fit. The shock velocity is evaluated as 220 ± 8 km/s.

Figure 5.2 shows the result of the SOP. The positions $x = 0$ and 4.5 mm are the surfaces of two foils, and $t = 0$ ns shows the laser timing. The plasmas created by the laser beams begin to propagate at $t = 0$ ns and $x = 0$ mm, and arrive at the second foil at $t = 15$ ns and $x = 4.5$ mm. After that, the second foil is ablated and heated by the plasmas from the

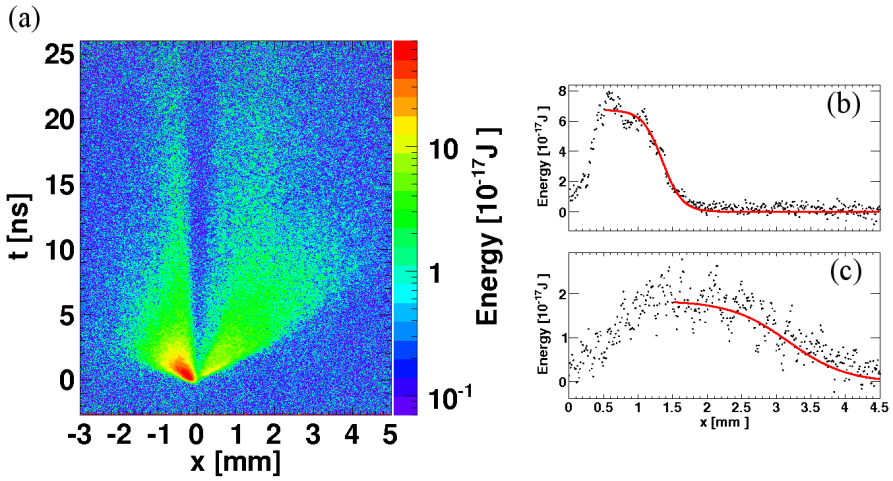

Figure 5.4: (a) The emission energy of the single-plane target obtained by the SOP. The vertical axis shows the time variation after laser irradiation and the horizontal axis shows the distance between two foils. The profiles of the emission energy obtained at (b) $t = 2.0$, (c) 7.4 ns after laser pulses, respectively.

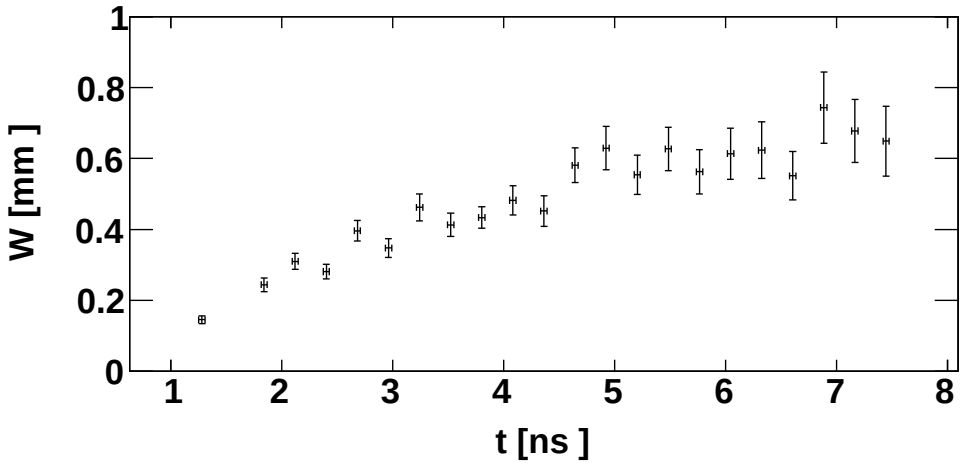

Figure 5.5: The time evolution of the transition width W (dots with error bars) evaluated by fitting the energy profiles with equation (5.1) for the single-plane target.

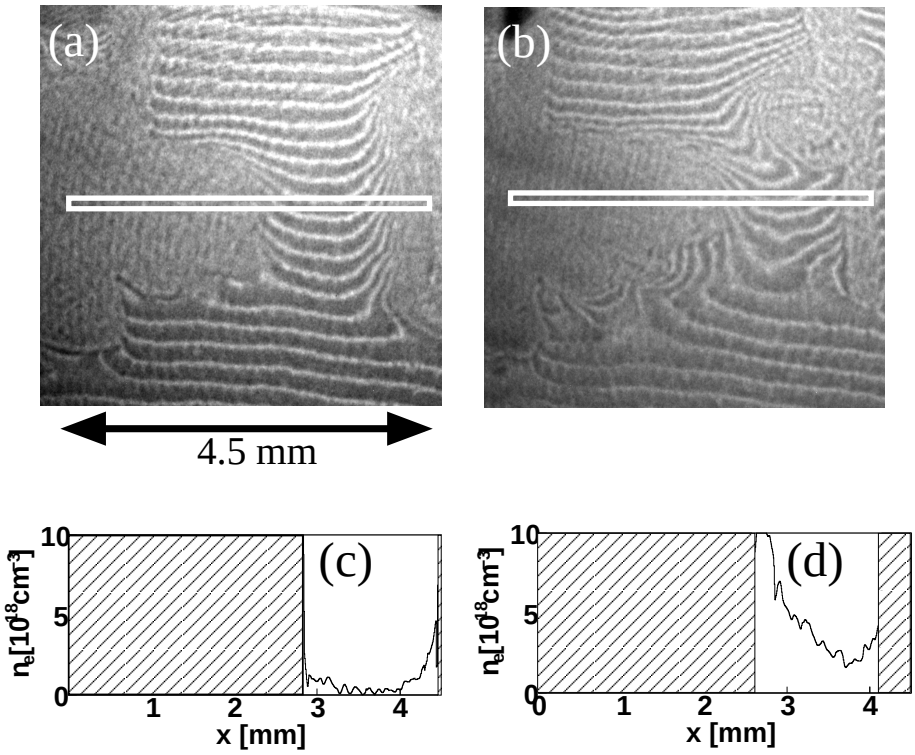

Figure 5.6: IF data obtained at (a) $t = 3.5$ and (b) 5 ns. Figures (c) and (d) show the corresponding density profiles of (a) and (b), respectively.

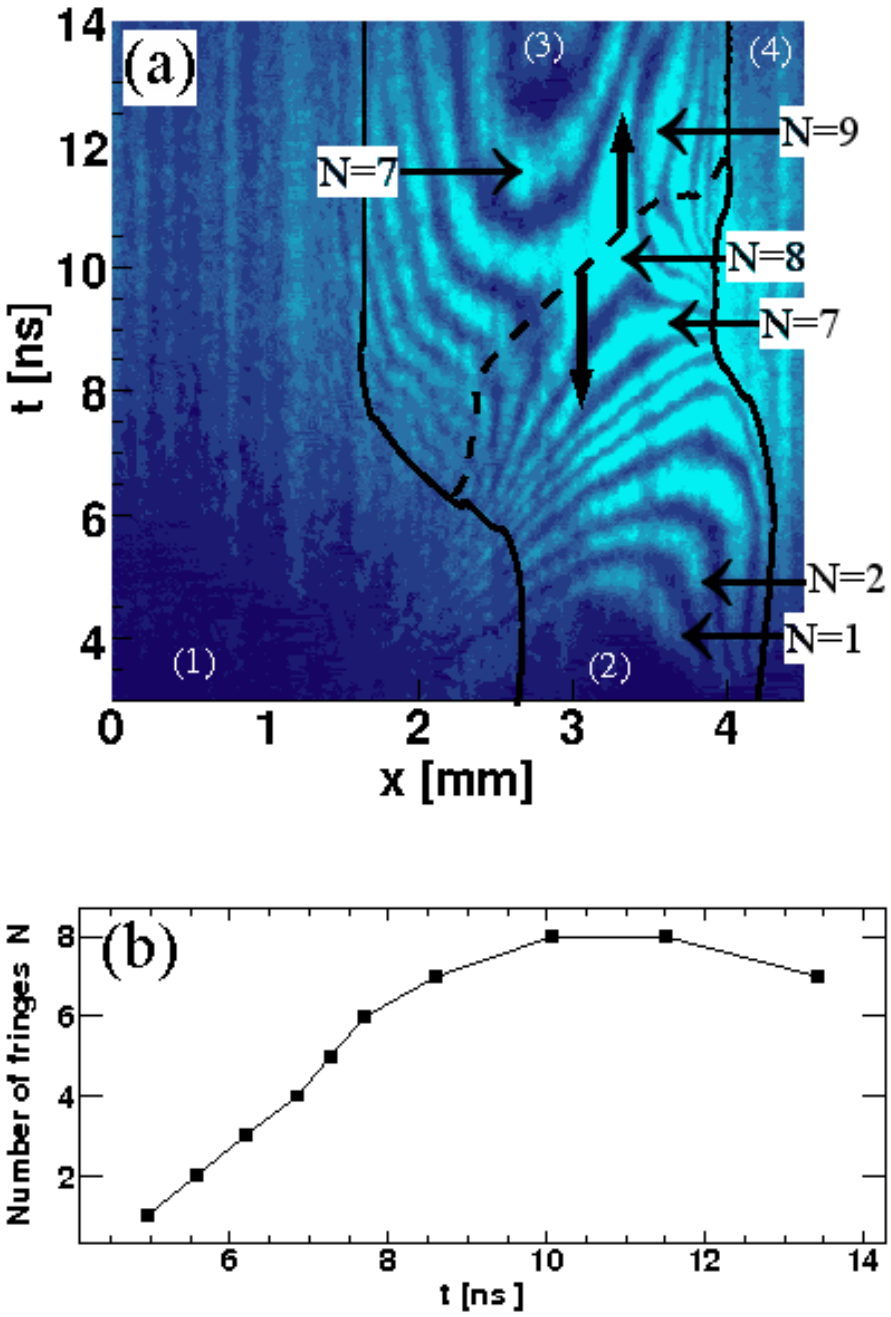

Figure 5.7: (a) The results of the SI. As time passes, interference fringes appear through the slit of the streak camera because the plasma density and/or size increases and the probe laser refracted in larger angles. (b) The number of fringes N which are observed at $x = 3.25$ mm.

first foil. The second foil is also ablated and plasmas are created by the radiation from the first foil at $t = 0$[67]. Figures 5.2(b), 5.2(c), and 5.2(d) show the profiles of the emission energy at $t = 2.0$, 11.0, and 12.1 ns, respectively. Values of the emission energy suddenly change at $x = 0.5$ mm in Fig. 5.2(b), $x = 3$ mm in Fig. 5.2(c), and $x = 3.3$ mm in Fig. 5.2(d). To evaluate the transition width of the emission energy ϵ, the profiles are fitted with the following equation:

$$\epsilon(x) = a + b \tanh(-\frac{x - x_{\rm s}}{W}), \tag{5.1}$$

where a, b, W, and $x_{\rm s}$ are fitting parameters. The parameter W represents the width of the transition region, and $x_{\rm s}$ is the position of the emission change. Figure 5.3(a) shows the temporal evaluation of the width W of the transition region (dots with error bars). The width gradually increases over 0.2 mm from $t = 1$ ns to $t = 12$ ns, and suddenly decreases to less than 0.1 mm after $t = 12$ ns. This indicates the shock formation. Figure 5.3(b) shows the position of the shock structure $x_{\rm s}$ observed by the SOP. The shock is created at $t = 12$ ns, and propagates toward the second foil. The shock velocity $v_{\rm s}$ is evaluated by a linear fitting as $v_{\rm s} = 220 \pm 8$ km/s.

Figure 5.4(a) shows the time variation of the emission energy for the single-plane target. The laser beams irradiate the foil at $x = 0$, and the plasmas are created and expand along the laser axis. In this case, there is no counter-streaming flows, and no jumps in the emission at the rear-side of the foil as is observed in the double-plane target. Figures 5.4(b) and 5.4(c) show the energy profiles at $t = 2.0$ and 7.4 ns, respectively. Time variation of the width W of the transition region is shown in Fig. 5.5. W is increasing with time monotonically.

Comparing the results of the double-plane and single-plane targets, the velocities of the plasmas from the first foil is different. The velocity of the plasma in double-plane is less than that of the single-plane target. The time variations of widths of these targets are

also different. The width in single-plane rapidly increases compare with the double-plane target. These two effects might be caused by the existence of the counter flows even early in time. The width becomes sharp only in counter-streaming plasmas, and this indicates the shock formation. On the other hand, no shock is created in expanding plasmas in vacuum.

Figures 5.6(a) and 5.6(b) show the IF data at $t = 3.5$ ns and $t = 5$ ns, respectively. Before the laser shot, the interference fringes lie in the horizontal direction. As the density increases, interference fringes are bended upward. The electron densities on the axis of the expanding plasma are calculated and shown in Figs. 5.6(c) and 5.6(d), respectively, assuming the axial symmetry. At the masked regions, the electron density is too high or the plasma size is too large to calculate the electron density because the interference fringes are disappeared. The maximum calculable electron density is less than $\sim 1 \times 10^{19}$ cm^{-3} in the detectable area. The electron densities at $x = 3.25$ mm are about $n_{\rm e} \sim 1 \times 10^{18}$ and 3×10^{18} at $t = 3.5$ and 5 ns, respectively.

Figure 5.7(a) shows the SI data which is the streaked images of the two-dimensional IF data. (Figs. 5.6(a) and 5.6(b)). The positions $x = 0$ and 4.5 mm show the target surfaces, and the vertical axis shows the time. Figure 5.7(b) shows the number of fringes N at $x = 3.25$ mm. The value N shown in the SI at $t = 10.1$ ns and $t = 11.5$ ns is the same value ($N = 8$) and it begins to decrease as the time passes. The phase begins to decrease at the dashed line in Fig. 5.7(a). It is difficult to calculate the correct values of the electron density using the SI because there is no information about the transverse profiles of the phase difference. However, the plasma should expand (l should increase) as time passes, the electron density $n_{\rm e}$ decreases after the timing of the dashed line because the phase difference $\delta\theta \propto n_{\rm e} l$ ($\simeq 4.2N \times 10^{17}$ cm^{-2}) decreases. The fringes disappeared at the outside of the solid lines (in the regions (1) and (4) in Fig. 5.7(a)) because the electron density and/or plasma size is large. The detectable electron density is $n_{\rm e} = (1\text{–}10) \times 10^{18}$ cm^{-3} for the IF, and the electron density in the regions (2) and (3) should be less than

$\sim 1 \times 10^{19}$ cm^{-3}.

Before the shock formation, time variation of the counter-streaming relative velocity $V(t)$ is estimated as $V(t) = |u_1(t,x) - u_2(t,x)|$, regardless of the position x, where $u_1(t,x) = x/t$ and $u_2(t,x) = -(4.5\,\mathrm{mm} - x)/t$ are the flow velocities from the first (left-side) foil and the second (right-side) foil, respectively, and is simply expressed as $V(t) = 4.5\,\mathrm{mm}/t$. Using the maximum ion density $n_\mathrm{i} = n_\mathrm{e}/Z$ for $n_\mathrm{e} = 1 \times 10^{19}$ cm^{-3} and Z = 3.5, and counter-streaming relative velocity $V(t)$, the ion–ion collision mean–free–path is calculated using the following definition: $\lambda_\mathrm{ii} = 2\pi\epsilon_0 m_\mathrm{i}^2 V^4/(e^4 Z^4 n_\mathrm{i} \ln\Lambda)$.[61] In Fig. 5.3(a), the evaluated λ_ii is shown with a red line. Before the shock formation, λ_ii is larger than the density transition width by more than one order of magnitude, and even after shock formation, this value is larger than shock width. Therefore, we conclude that the shock generated in counter-streaming plasmas are the collisionless shock.

Here, we estimate the plasma density and temperature at the upstream and downstream regions of the shock. The created plasmas were obviously optically thin at the position where the shock was generated, because the probe laser could penetrate them and was detected with SI as shown in Fig. 5.7. Radiation energy density from such plasmas is expressed with thermal bremsstrahlung emission[59] $\epsilon_\lambda(T_\mathrm{e}) \propto Z n_\mathrm{e}^2 \exp(-hc/\lambda T_\mathrm{e}) g^{ff}/\sqrt{T_\mathrm{e}}$, where h is the planck constant, Z is the degree of ionization, and g^{ff} is a velocity averaged Gaunt factor[77]. The ratio of ϵ_λ at the downstream to upstream region is calculated as

$$\frac{\epsilon_{\lambda 1}}{\epsilon_{\lambda 0}} = \left(\frac{n_1}{n_0}\right)^2 \left(\frac{T_1}{T_0}\right)^{-1/2} \left(\frac{g_1^{ff}}{g_0^{ff}}\right) \exp\left[-\frac{hc}{\lambda T_0}\left(\left(\frac{T_1}{T_0}\right)^{-1} - 1\right)\right], \tag{5.2}$$

where T_0 and T_1 are the electron temperatures at the upstream and downstream, respectively. On the other hand, from the shock condition, temperature and density ratios in a

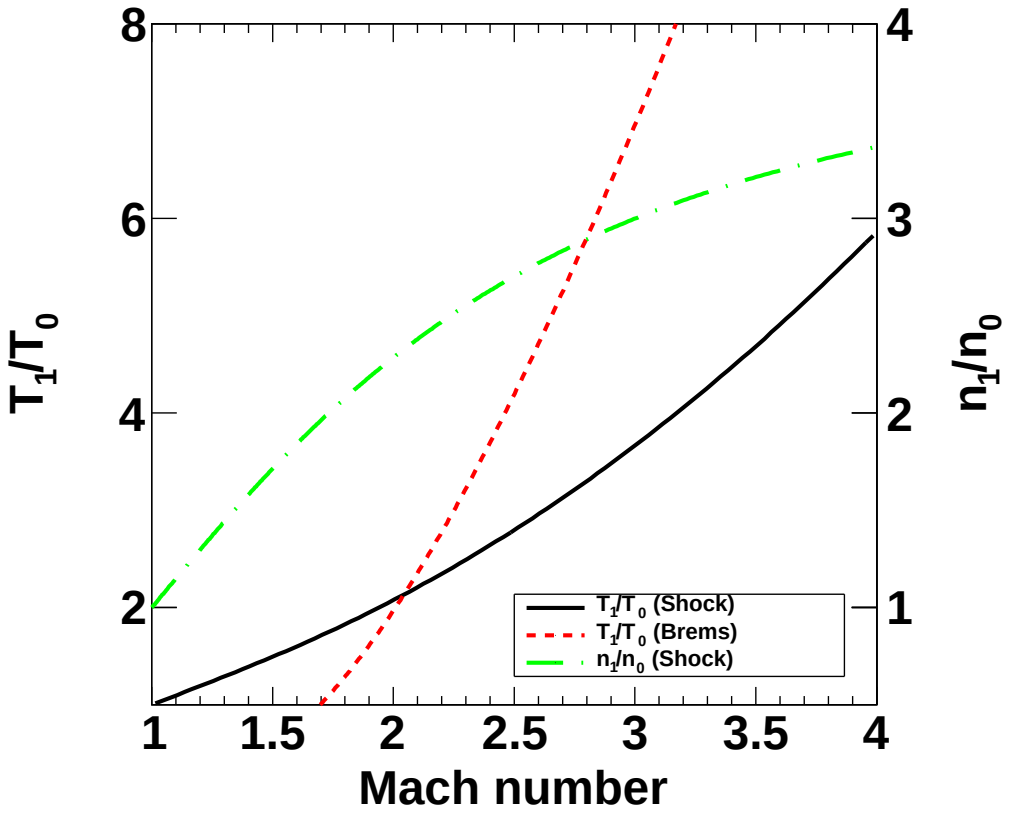

Figure 5.8: The temperature (T_1/T_0 (shock): solid line) and density (n_1/n_0 (shock): dash-dot line) ratios derived from equations (5.3) and (5.4), respectively, as a function of M. T_1/T_0 is also calculated from equation (B.1) (T_1/T_0 (brems)) as a function of M using T_1/T_0 (shock), n_1/n_0 (shock), T_0, and the measured emission ratio $\epsilon_{\lambda 1}/\epsilon_{\lambda 0}$.

perfect gas are expressed with a Mach-number $M = v_0/c_s$,

$$\frac{T_1}{T_0} = \frac{[2\gamma M^2 - (\gamma - 1)][(\gamma - 1)M^2 + 2]}{(\gamma + 1)^2 M^2}, \tag{5.3}$$

$$\frac{n_1}{n_0} = \frac{v_0}{v_1} = \frac{(\gamma + 1)M^2}{(\gamma - 1)M^2 + 2}, \tag{5.4}$$

where v_0 and v_1 are, respectively, the upstream and downstream flow velocities in the shock rest frame, c_s is the sound velocity, and γ is the adiabatic constant. In the upstream region, c_s is expressed as $c_s = \sqrt{(Z + \gamma)T_0/m_{\rm i}}$, where $m_{\rm i}$ is the ion mass, and we assume $T_0 = T_{\rm e} = T_{\rm i}$, electrons are isothermal and $\gamma = 5/3$. Figure 5.8 shows the temperature

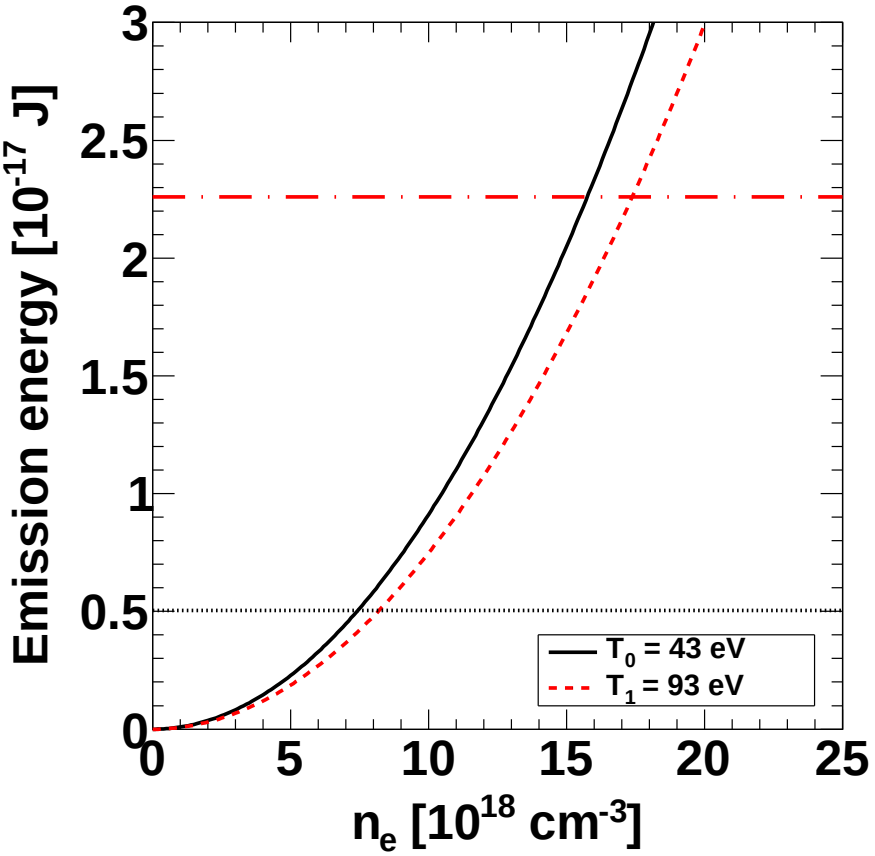

Figure 5.9: The thermal bremsstrahlung emission energies for the upstream ($T_{\rm e} \simeq 43$ eV: solid line) and the downstream ($T_{\rm e} \simeq 93$ eV: dash line) region assuming the vertical plasma size of $l = 3$ mm. The emission energy at the upstream ($\epsilon_{\lambda 0} \simeq 5.04 \times 10^{-18}$ J) and downstream ($\epsilon_{\lambda 1} \simeq 2.26 \times 10^{-17}$ J) regions are shown in a dot line and dash-dot line, respectively.

(T_1/T_0 (shock): solid line) and density (n_1/n_0 (shock): dash-dot line) ratios derived from equations (5.3) and (5.4), respectively, as a function of M. T_1/T_0 is also calculated from equation (B.1) (T_1/T_0 (brems)) as a function of M using T_1/T_0 (shock), n_1/n_0 (shock), T_0, g_1^{ff}/g_0^{ff}, and the measured emission ratio $\epsilon_{\lambda 1}/\epsilon_{\lambda 0}$. v_0 is calculated as $v_0 = u_1 + v_s$ ($v_s = 220$ km/s) for given time t. Therefore, T_0 is derived from $M = v_0/\sqrt{(Z+\gamma)T_0/m_{\rm i}}$ as a function of M and t. At $t = 13$ ns, $\epsilon_{\lambda 1}/\epsilon_{\lambda 0} \simeq 4.48$ is obtained from Fig. 5.2 and $v_0 = 299$ km/s. T_1/T_0 (brems) at $t = 13$ ns is also plotted in Fig. 5.8 (dash line) using the Gaunt factor ratio $g_1^{ff}/g_0^{ff} = 1.17$. The point of intersection between T_1/T_0 (shock) and

T_1/T_0 (brems) in Fig. 5.8 gives $M \simeq 2.1$, and therefore, $T_0 \simeq 43$ eV, $T_1 \simeq 93$ eV, and $n_1/n_0 \simeq 2.3$. Using above temperatures T_0 and T_1, the emission energies are calculated from the bremsstrahlung emission. Figure 5.9 shows the emission energies for the upstream ($T_{\rm e} \simeq 43$ eV: solid line) and the downstream ($T_{\rm e} \simeq 93$ eV: dash line) regions assuming the vertical plasma size of $l = 3$ mm. The Gaunt factors are evaluated using the above temperatures as[77] $g_0^{ff} \sim 1.8$ and $g_1^{ff} \sim 2.1$, and the ratio $g_1^{ff}/g_0^{ff} \sim 1.2$ is consistent with that used in the calculation of T_1/T_0 (brems) shown in Fig. 5.8. The positions of intersection between the measured emission energies at the upstream ($\epsilon_{\lambda 0} \simeq 5.04 \times 10^{-18}$ J: dot line) and downstream ($\epsilon_{\lambda 1} \simeq 2.26 \times 10^{-17}$ J: dash-dot line) regions give the electron densities as $n_0 \simeq 7.4 \times 10^{18}$ cm^{-3} for the upstream region and $n_1 \simeq 1.7 \times 10^{19}$ cm^{-3} for the downstream region.

The electron density can be estimated from the number of fringes $N = 7$–9 in the SI data at $x = 3.5$ mm (Fig. 5.7) where shock is observed at $t = 13$ ns in the SOP. Assuming the plasma size $l = 3$ mm, $n_{\rm e}$ is estimated as $4.2N \times 10^{17}/0.3$ cm^{-3} = (9.8–13)$\times 10^{18}$ cm^{-3}. These values are consistent to the densities estimated from Fig. 5.9.

Figures 5.10(a)–5.10(d) show the SG data obtained at $t = 9.5$, 11.5, 13.5, and 15.5 ns. The expanding plasma is collimated at $t = 13.5$ and 15.5 ns. The slit position that the SOP is observing is shown with solid lines at the center of the figures. The triangle marks show the positions of the shock front or the density changes evaluated by fitting the energy profiles with equation (5.1). The shock structures were observed by the SOP, however, they are not detected by the SG and IF, because the density jump associated with the shock is too small to resolve. The shock is created in front of the expanding plasmas. The jet collimation occurs after the shock formation ($t \sim 12$ ns), and it indicates that the shock formation plays an important role for the jet collimation. When the counter-streaming plasmas, which have different density and temperature profiles, interact each other, it can result in the formation of the two different shock structures: one is forward-reverse shocks,

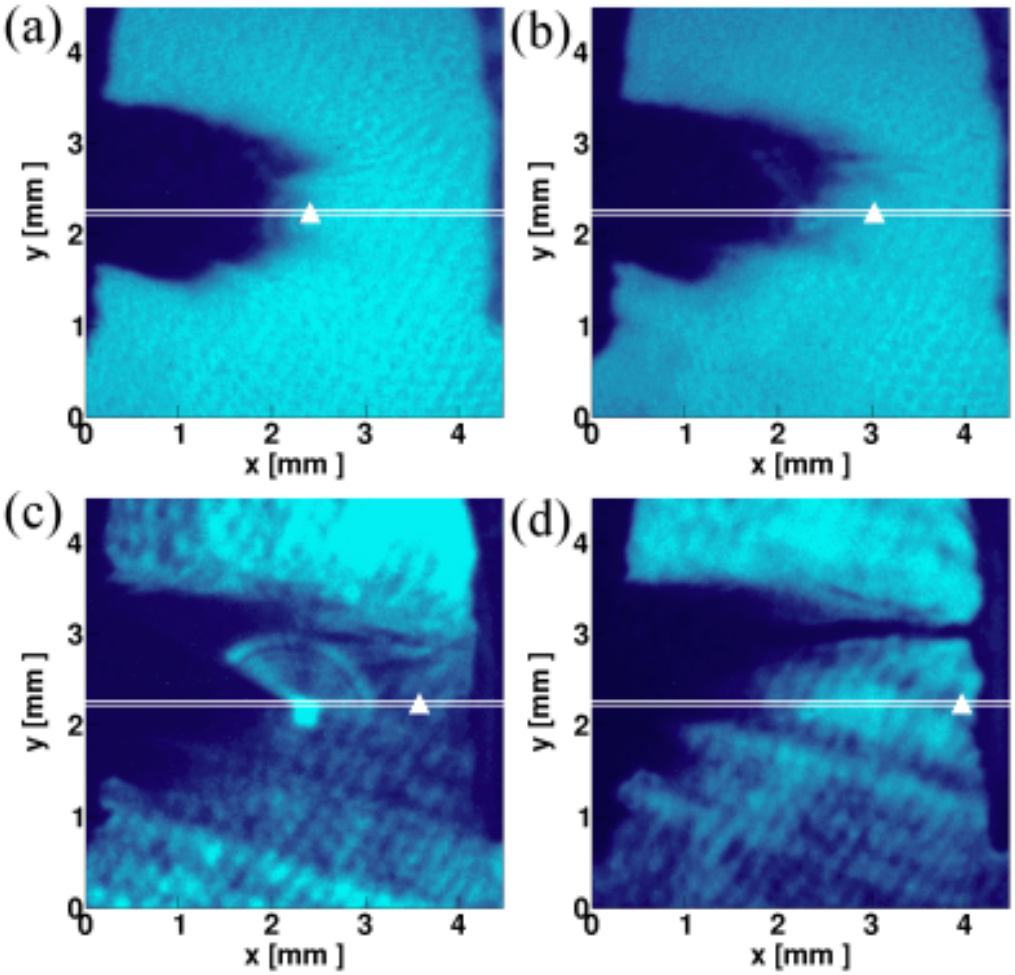

Figure 5.10: The SG data at (a) $t = 9.5$ ns, (b) 11.5 ns, (c) 13.5 ns, and (d) 15.5 ns. The positions $x = 0$ and 4.5 mm show the target surfaces. The vertical lines at $y = 2.2$ mm are the position that the SOP is observing. The triangle marks show the positions of the shock front or the density changes which are the results of fitting (Fig. 5.3(b)).

and the other is a forward shock in low-density plasma and a rarefaction wave in the dense plasma[66]. In the experimental data of the SOP, SG, and IF, there are no evidence of for the reverse-shock formation nor rarefaction wave. The rarefaction or reverse shock wave is hard to measure with the density or emission measurements, because they do not have enough resolution to analyze the structure of the wave: the density doesn't change too much at the rarefaction wave or reverse shock to detect the structure in the SOP, and is too high

above the detectable density in the SG. Hence, there can be a rarefaction or reverse shock wave in the dense region propagating to the opposite direction to the observed shock wave in the shock rest frame. The shock created in front of the jet should be bended as the jet propagates. As a result of the shock-rarefaction wave or forward-reverse shock formation, the dense plasma should be confined in a narrow space and that results in the jet formation.

5.4 Conclusion

We have reported the time evolution of plasma expansion and collisionless shock formation in counter-streaming plasmas with the streaked optical pyrometer in front of the propagating plasma jet which was observed by the shadowgraphy. Plasma density was measured with interferometry and streaked interferometry. The shock formation was confirmed with the streaked optical pyrometer as a sudden decrease in the transition width. The electron density was calculated by the interferometry early in time ($t = 3.5$ and 5 ns), and the time variation was observed by the streaked interferometry. The ion–ion collision mean–free–path was much larger than the evaluated shock width (< 100 μm) even with the maximum calculable electron density $\sim 1 \times 10^{19}$ cm^{-3}. The electron temperatures and densities are evaluated from the jump condition in a shock wave and the measured emission energy, which is dominated by thermal bremsstrahlung emission. The electron temperature and density jump from $T_{\rm e} = 43$ eV and $n_{\rm e} = 7.0 \times 10^{18}$ cm^{-3} at the upstream region to $T_{\rm e} = 93$ eV and $n_{\rm e} = 1.7 \times 10^{19}$ cm^{-3} at the downstream reagion of the shock. These densities are nearly consistent with the estimated values ($n_{\rm e} =$ (9.8–13)$\times 10^{18}$ cm^{-3}) from the SI.

This collisionless shock was generated in front of the jet[67] due to collisionless interaction in counter-streaming plasmas and no shocks and jets were observed in the single-plane target, in which no counter flow exists. In such a case, it is well known[75] that a reverse-shock or a rarefaction wave is, in general, generated in the opposite direction to

propagating jet. In the experiment, it was clearly observed that the jet and forward shock were generated in a same experimental configurations. This result shows that the shock can confine plasmas and collimate as a jet as argued by Kuramitsu *et al*.[67]

Chapter 6

Conclusion

We have observed electrostatic collisionless shock in high-speed counter-stremming plasmas without an external magnetic field.

In chapter 3, We reported strong electrostatic (ES) collisionless shock generation. A large density jump is observed both in the interferogram and shadowgraph at the same time and position. The width of the density jump is much shorter than the ion-ion mean-free-path, and hence the measured density jump is a collisionless shock. This shock is not an electromagnetic (EM) shock but an ES shock because the shock width is much shorter than the prediction for the EM shock obtained by the PIC simulation[30]. The PIC simulation shows that the high Mach-number ES shock is maintained by the balance between the pressure of upstream ions enhanced by reflected ions and that of the ES field stemming from high-temperature electrons in the downstream.

In chapter 4, we reported the calibration results of the gated optical imager (GOI) and the streaked optical pyrometer (SOP). These results are consistent within 30 % and are applicable to collisionless shock experiments as shown in chapter 5.

In chapter 5, we reported the time evolution of plasma expansion and collisionless shock formation with the SOP in front of the propagating plasma jet which was observed by the shadowgraphy. The shock formation was confirmed with the SOP as a sudden decrease

in the transition width. The ion–ion collision mean–free–path was much larger than the evaluated shock width even with the maximum detectable electron density $\sim 1\times10^{19}$ cm^{-3}. The electron temperatures and densities are evaluated from the jump conditions in a shock wave and the measured emission energy, which is dominated by thermal bremsstrahlung emission. In the experiment, it was clearly observed that the jet and forward shock were generated in the same experimental configurations. The formation of the collisionless shock is speculated to generate the effective pressure through the ES field to prevent the transverse expansion of the jet produced at the same time.

Appendix A

Collisionless shock

This section introduces a simple explanation and derive important relations concerning to shock waves. First, we explain the fluid shocks and derive the Rankine-Hugoniot relations and other useful formulas. Next, we introduce the collisionless shock and other subjects.

A.1 Rankine–Hugoniot relations

In the case of compressible fluids, shock waves are excited as a result of the development of fluctuations. For simplicity, we treat the shock which propagates perpendicular to its surface in this section. At the shock surface, physical quantities vary discontinuously, and this surface propagates steadily as a wave in fluids. At both sides of shock surface, the conservation laws of mass, momentum, and energy are satisfied. These conversation laws are written in a shock rest frame as follows[65, 66]:

$$\rho_0 u_0 = \rho_1 u_1, \tag{A.1}$$

$$p_0 + \rho_0 u_0^2 = p_1 + \rho_0 u_0^2, \tag{A.2}$$

$$h_0 + \frac{u_0^2}{2} = h_1 + \frac{u_1^2}{2}, \tag{A.3}$$

where the subscript 0 and 1 represents the upstream and downstream of the shock wave, and ρ, u, and h are the density, flow velocity, and the enthalpy in the perpendicular to the shock surface. In the case of an ideal gas, equation (A.3) becomes

$$\frac{u_0^2}{2} + \frac{\gamma}{\gamma - 1}\frac{p_0}{\rho_0} = \frac{u_1^2}{2} + \frac{\gamma}{\gamma - 1}\frac{p_1}{\rho_1}. \tag{A.4}$$

Equations (A.1), (A.2), and (A.4) are called Rankine–Hugoniot relations. These relations contain six parameters u_0, ρ_0, p_0, u_1, ρ_1, and p_1. If three parameters in upstream region (u_0, ρ_0, and p_0) are known, the parameters in downstream can be derived using these formula.

Using equations (A.1), (A.2), and (A.4), the compression ratio ρ_1/ρ_0 can be derived:

$$\frac{\rho_0}{\rho_1} = \frac{u_1}{u_0} = \frac{(\gamma + 1) + (\gamma - 1)p_2/p_1}{(\gamma - 1) + (\gamma + 1)p_2/p_1}. \tag{A.5}$$

The sound velocity c_s in an ideal gas is defined as

$$c_s \;=\; \sqrt{\left(\frac{\partial p}{\partial \rho}\right)_S} = \sqrt{\gamma p/\rho} = \sqrt{\gamma RT}, \tag{A.6}$$

where R is the gas constant, and Mach-number M_i ($i = 0$ or 1) is expressed with the ratio of flow velocity to the sound velocity:

$$M_i = u_i/c_{si}., \tag{A.7}$$

where i denotes the upstream ($i = 0$) or downstream ($i = 1$) region. From equations (A.5), (A.6), and (A.7), the density, pressure, and temperature ratios of the downstream to

upstream regions are expressed as

$$\frac{\rho_1}{\rho_0} = \frac{u_0}{u_1} = \frac{(\gamma+1){M_0}^2}{2+(\gamma-1){M_0}^2}, \tag{A.8}$$

$$\frac{p_1}{p_0} = \frac{2\gamma {M_0}^2}{\gamma+1} - \frac{\gamma-1}{\gamma+1}, \tag{A.9}$$

$$\frac{T_1}{T_0} = \frac{\left[2\gamma {M_0}^2-(\gamma-1)\right]\left[(\gamma-1){M_0}^2+2\right]}{(\gamma+1)^2 M_0^2}. \tag{A.10}$$

If the Mach-number is very large ($M_0 \to \infty$) and $\gamma = 5/3$, the compression ratio becomes $(\gamma+1)/(\gamma-1) \to 4$.

A.2 Collisionless shock

Fluid shocks have widths of the order of mean-free-path because collisions among particles are dominant. However, in low-density and high-temperature plasmas, the width of shock transition layer is much shorter than mean-free-path, for example, as observed in SNRs and Earth's bow shock. Therefore, in such cases, collision can not be responsible for the thiner structure. We use the terminology "collisionless shocks" for shocks in which the collisional effect is not dominant and other processes play an important role.

In this section, we explain ion acoustic shocks as an example of collisionless shocks.

A.2.1 Ion acoustic waves

One of the important differences between collisional and collisionless shocks is the physical mechanism in shock formation. The former is generated and maintained by convections and dissipations. On the other hand, in the latter case, the dispersive effect is important. In a neutral gas, the dispersion relation is expressed as

$$\frac{\omega}{k} = \sqrt{\frac{\gamma k_{\rm B} T}{m_{\rm i}}} = c_s, \tag{A.11}$$

where γ is the specific heat ratio, k_{B} is the Boltzmann constant, and T is the temperature, and c_s is a sound velocity.

Considering shorter wavelength, however, the dispersion relation is different from equation (A.11). The equations of ion and electron motion without external magnetic field are expressed as follows:

$$m_{\mathrm{i}} n_{\mathrm{i}} (\frac{\partial}{\partial t} + \mathbf{u_i} \cdot \nabla)\mathbf{u_i} = Z e n_{\mathrm{i}} \mathbf{E} - \nabla(n_{\mathrm{i}} k_{\mathrm{B}} T_{\mathrm{i}}) = -Z e n_{\mathrm{i}} \nabla\phi - \gamma_{\mathrm{i}} k_{\mathrm{B}} T_{\mathrm{i}} \nabla n_{\mathrm{i}}, \tag{A.12}$$

$$m_{\mathrm{e}} n_{\mathrm{e}} (\frac{\partial}{\partial t} + \mathbf{u_e} \cdot \nabla)\mathbf{u_e} = e n_{\mathrm{e}} \mathbf{E} - \nabla(n_{\mathrm{e}} k_{\mathrm{B}} T_{\mathrm{e}}) = -e n_{\mathrm{e}} \nabla\phi - \gamma_{\mathrm{e}} k_{\mathrm{B}} T_{\mathrm{e}} \nabla n_{\mathrm{e}}, \tag{A.13}$$

where m, n, $\mathbf{u}$, and T are the mass, density, velocity, and temperature, respectively, $\mathbf{E}$ is the electric field, and the subscripts e and i represent the electrons and ions, respectively. Here, assuming $m_{\mathrm{e}} = 0$ and one-dimensional motion, equation (A.13) becomes

$$e n_{\mathrm{e}} \frac{d\phi}{dx} + k_{\mathrm{B}} T_{\mathrm{e}} \frac{dn_{\mathrm{e}}}{dx}, \tag{A.14}$$

$$n_{\mathrm{e}} = n_0 \exp\left(\frac{e\phi}{k_{\mathrm{B}} T_{\mathrm{e}}}\right). \tag{A.15}$$

Poisson equation is expressed as

$$\nabla^2 \phi = -\frac{e}{\epsilon_0}(n_{\mathrm{i}} - n_{\mathrm{e}}). \tag{A.16}$$

The equation of continuity for ions is written as

$$\frac{\partial n_{\mathrm{i}}}{\partial t} + \nabla \cdot (n_{\mathrm{i}} \mathbf{v}_{\mathrm{i}}). \tag{A.17}$$

Linearizing equations (A.12), (A.15), (A.16), and (A.17), we obtain the dispersion relation

for the ion acoustic wave.

$$\omega = k\sqrt{\frac{\gamma_{\rm e} Z k_{\rm B} T_{\rm e}}{m_{\rm i}} \frac{1}{1+k^2\lambda_{\rm D}^2} + \frac{\gamma_{\rm i} k_{\rm B} T_{\rm i}}{m_{\rm i}}} \tag{A.18}$$

Figure A.1 shows a typical dispersion curve expressed by equation (A.18). In longer

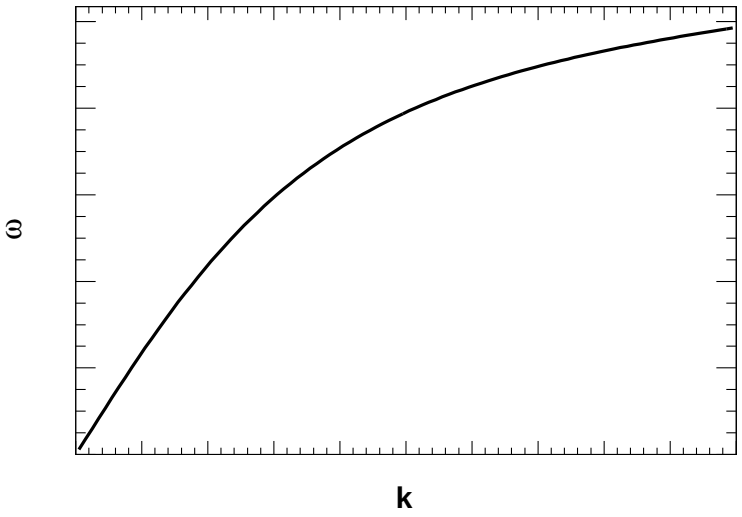

Figure A.1: A typical dispersion curve for the ion acoustic wave.

wavelength (smaller k), the dispersion relation is approximately linear (ω/k =const.). On the other hand, the phase velocity $v_\phi = \omega/k$ in shorter wavelength is smaller than that in longer wavelength. The shorter wavelength mode can be generated due to nonlinear coupling. Then, the shorter wavelength modes travel with slower phase speeds than the initial pulse, and this result in the oscillation behind the shock front.

A.2.2 Ion acoustic solitons and shocks

We simply explain the one-dimensional collisionless shocks which are generated from the ion acoustic waves. Here, we assume $T_{\rm i} = 0$, that is, all ions travel with the same speed, and electrons obey Maxwell distribution. The ion velocity in a potential ϕ is obtained from

the energy conservation:

$$u = \sqrt{u_0^2 - \frac{2e\phi}{m_\mathrm{i}}}. \tag{A.19}$$

Therefore, the ion density is expressed using the mass conservation's low

$$n_\mathrm{i} = \frac{n_0 u_0}{u} = \frac{n_0}{\sqrt{1 - \frac{2e\phi}{m_\mathrm{i} u_0^2}}}. \tag{A.20}$$

Using the electron density (equation (A.15)), the ion density (equation (A.20)), and the Poisson equation (equation (A.16)), we obtain the following one-dimensional relation.

$$\frac{d^2\phi}{dx^2} = \frac{en_0}{\epsilon_0}\left[\exp\left(\frac{e\phi}{kT_\mathrm{e}}\right) - \frac{1}{1 - \frac{2e\phi}{m_\mathrm{i} u_0^2}}\right] \tag{A.21}$$

The above formula is expressed with three dimensionless parameters $\chi = e\phi/k_\mathrm{B}T_\mathrm{e}$, $\xi = x/\lambda_\mathrm{D}$, and $M = u_0/\sqrt{k_\mathrm{B}T_\mathrm{e}/m_\mathrm{i}^2}$.

$$\frac{d^2\chi}{d\xi^2} = e^\chi - \frac{1}{\sqrt{1 - \frac{2\chi}{M^2}}} \tag{A.22}$$

If we assume the right-hand side of equation (A.22) as a derivative of a potential $V(\chi)$ with respect to χ, the Sagdeev potential V can be defined.

$$\frac{dV(\chi)}{d\chi} = -e^\chi + \frac{1}{\sqrt{1 - \frac{2\chi}{m^2}}}. \tag{A.23}$$

$V(\chi)$ is obtained by integrating equation (A.23) with an initial condition $V(\chi = 0) = 0$.

$$V(\chi) = 1 - e^\chi + M^2\left(1 - \sqrt{1 - \frac{2\chi}{M^2}}\right) \tag{A.24}$$

If M satisfies $1 < M < 1.6$, the potential $V(\chi)$ has a well in $0 < \chi < M^2/2$. Figure A.2

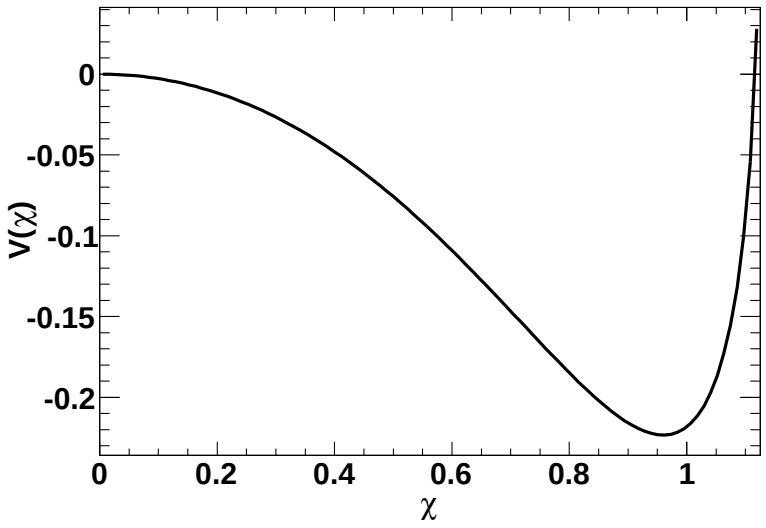

Figure A.2: Sagdeev potential $V(\chi)$ for $M = 1.5$.

shows the Sagdeev potential $V(\chi)$ for $M = 1.5$. In such cases, assuming a virtual particle in the potential $V(\chi)$ moving with a velocity of $d\chi/d\xi$ ($d\chi/d\xi|_{\xi=0} = 0$), it moves from $\chi = 0$ to $\chi > 0$, and reflected by a potential wall. As a result the potential $\phi(\xi)$ (i.e. $\tilde{\phi}(x)$) has a pulse-shape solution, which is called "soliton". However, if a real particle losses its energy in the potential $\phi(x)$, the virtual particle in $V(\chi)$ oscillates in a positive χ. This means that the potential $\phi(x)$ oscillates and the symmetry of solitary solution is distorted. This effect results in a shock-like structure formation. This wave is called "collisionless shock". The transition width of this shock wave is comparable to the Debye length $\lambda_{\rm D}$. The collisionless shock formation can be generated due to Landau damping and ion reflection at the shock front[78]. The ion acoustic shock waves have been investigated experimentally in laboratories using double-plasma device[44, 45, 46].

A.2.3 Two-stream instability

Collisionless shocks can be excited due to collisionless plasma instabilities. Now we consider a cold and unmagnetized plasma which has some velocity components $u_{0\alpha}$. The subscript α denotes components in the above plasmas. The linearized equations of continuity, motion and Poisson's equation are expressed as[79]

$$\frac{\partial n_1}{\partial t} + \nabla \cdot (n_0 \, \mathbf{u_1} + n_1 \, \mathbf{u_0}) = 0, \tag{A.25}$$

$$\frac{\partial \mathbf{u_1}}{\partial t} + (\mathbf{u_0} \cdot \nabla)\mathbf{u_1} = \frac{Ze}{m}(\mathbf{E_1} + \mathbf{u_0} \times \mathbf{B_1}), \tag{A.26}$$

$$\nabla \cdot \mathbf{E_1} = \frac{1}{\epsilon_0} \sum Zen_1. \tag{A.27}$$

Using above formulas, we obtain the velocity and density perturbations

$$\mathbf{u_1} = \frac{iZe\mathbf{E_1}}{m(\omega - \mathbf{k} \cdot \mathbf{u_0})}, \tag{A.28}$$

$$n_1 = \frac{iZen_0\mathbf{k} \cdot \mathbf{E_1}}{m(\omega - \mathbf{k} \cdot \mathbf{u_0})^2}. \tag{A.29}$$

The Poisson equation (equation (A.27)) has a non-trivial solution ($\mathbf{E_1} \neq 0$) when the following equation is satisfied.

$$\sum_{\alpha} \frac{\omega_{p\alpha}^2}{(\omega - \mathbf{k} \cdot \mathbf{u}_\alpha)^2} = 1 \tag{A.30}$$

If there are two components which have velocities $\mathbf{u_0}$ and $-\mathbf{u_0}$ in opposite directions, the dispersion relation can be written as

$$\frac{\omega_p^2}{(\omega - ku_0)^2} + \frac{\omega_p^2}{(\omega + ku_0)^2} = 1, \tag{A.31}$$

which has a solution of

$$\omega^2 = (ku_0)^2 + \omega_p^2 \pm \omega_p\sqrt{\omega_p^2 + 4k^2u_0^2}. \tag{A.32}$$

Equation (A.32) has 4 roots. In the rage of $0 < k < \sqrt{2}\omega_p/k$, two of them are complex numbers, and instability can be occur.

A.3 Collision mean–free–path

In plasmas, the electrostatic forces between particles have much longer ranges than the forces between neutral atoms. To evaluate collision mean–free–paths, the effects of such distant collisions should be considered. In this section, we show collisional effects in collisionless plasmas.

A.3.1 Coulomb scattering

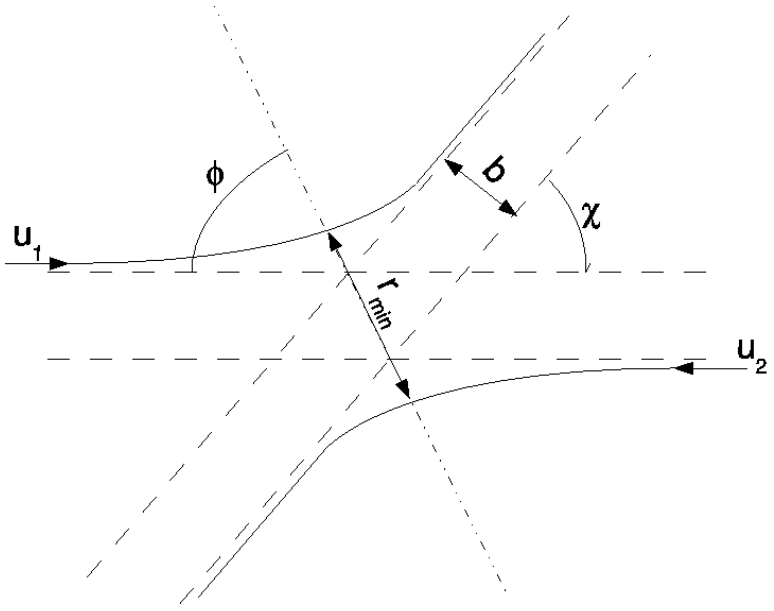

Figure A.3: Trajectories of a charged particle interaction.

When two charged particles interact with each other, the particles move on two hyperbolas as shown in Figure A.3. The energy and angular momentum conservations are expressed $\mu = m_1 m_2/(m_1 + m_2)$ is a reduced mass, the vector between two particles $\mathbf{r} = \mathbf{r_2} - \mathbf{r_1}$, relative velocity $\mathbf{u} = \mathbf{u_1} - \mathbf{u_2}$, initial velocity $\mathbf{u}_0$, and deflected angle χ

$$E = \frac{\mu}{2}u^2 = \frac{\mu}{2}(\dot{r}^2 + r^2\dot{\phi}^2) + \frac{Z_1 Z_2 e^2}{4\pi\epsilon_0 r}, \tag{A.33}$$

$$L = \mu u b = \mu r^2 \dot{\phi}^2 \tag{A.34}$$

where $\phi = \pi/2 - \chi$, and b is the impact parameter, Z is the degree of charge, and ϵ_0 is the dielectric constant. Using above equations we obtain

$$\dot{\phi}^2 = \frac{u_0 b}{r^2} \tag{A.35}$$

$$\dot{r}^2 = u_0^2 - \frac{Z_1 Z_2 e^2}{2\pi\epsilon_0 \mu r} - \frac{u_0^2 b^2}{r^2}, \tag{A.36}$$

and therefore we obtain $\dot{r}$ for approaching particles,

$$\dot{r} = \frac{dr}{dt} = -\sqrt{u_0^2 - \frac{Z_1 Z_2 e^2}{2\pi\epsilon_0 \mu r} - \frac{u_0^2 b^2}{r^2}} \tag{A.37}$$

and the angle when two particles have closest approach

$$\phi_0 = \int d\phi = \int_{\infty}^{r_{min}} \frac{\dot{\phi}}{\dot{r}} dr \tag{A.38}$$

$$= -\int_{\infty}^{r_{min}} \frac{u_0 b dr}{r^2\sqrt{u_0^2 - \frac{Z_1 Z_2 e^2}{2\pi\epsilon_0 \mu r} - \frac{u_0^2 b^2}{r^2}}}. \tag{A.39}$$

Integrating the above equation, we obtain ϕ_0 as follows:

$$\tan\left(\frac{\pi}{2} - \phi_0\right) = \tan\frac{\chi}{2} = \frac{Z_1 Z_2 e^2}{4\pi\epsilon_0 \mu b u_0^2}. \tag{A.40}$$

If the particles are deflected with $\pi/2$ (i.e. $\chi = \pi/2$), the impact parameter b_0 is written as below:

$$b_0 = \frac{Z_1 Z_2 e^2}{4\pi\epsilon_0 \mu u_0^2}. \tag{A.41}$$

A.3.2 Mean–free–path for counter-streaming plasmas

If we define "close collision" as particle scattering with the angle of $\pi/2$ or more, the collision time can be defined as an average time between each close collision.

$$t_{\rm c} = \frac{1}{\pi b_0^2 u_0 n} \tag{A.42}$$

This evaluation is very poor because charged particles can be scattered not only by a close collision but also by multi distant collisions with small deflection angles. The average deflection of a velocity in a unit time perpendicular to the initial velocity is expressed as [61]

$$\left\langle (\Delta u_\perp)^2 \right\rangle = 8\pi n_{\rm i} u_0^3 b_0^2 \ln\Lambda, \tag{A.43}$$

where $n_{\rm i}$ is an ion density, $\ln\Lambda = \lambda_{\rm D}/b_0$ is the Coulomb logarithm, and $\lambda_{\rm D}$ is the Debye length. Here, we define relaxation time $t_{\rm D}$ in which particles are deflected over $\pi/2$ using following formula

$$\left\langle (\Delta u_\perp)^2 \right\rangle t_{\rm D} = u_0^2, \tag{A.44}$$

and therefore,

$$t_{\rm D} = \frac{1}{8\pi n_{\rm i} u_0 b_0^2 \ln\Lambda}. \tag{A.45}$$

Using $t_{\rm D}$, the collision mean–free–path $\lambda_{\rm ii}$ is calculated multiplying $t_{\rm D}$ by the initial velocity u_0, and using equation (A.41):

$$\lambda_{\rm ii} = t_{\rm D} u_0 = \frac{2\pi\epsilon_0^2 \mu^2 u_0^4}{n_{\rm i} Z_1^2 Z_2^2 e^4 \ln\Lambda}. \tag{A.46}$$

In the case of collisions between particles with same masses and charges, $\mu = m/2$, and $Z_1 = Z_2 = Z$, and then

$$\lambda_{\rm ii} = \frac{\pi\epsilon_0^2 m^2 u_0^4}{2 n_{\rm i} Z^4 e^4 \ln\Lambda}. \tag{A.47}$$

A.4 Particle acceleration at shock wave

Cosmic rays are accelerated to extremely high energy in the universe. The mechanisms for the acceleration have been investigated theoretically and experimentally. E. Fermi proposed the theory in which particles are accelerated statistically by the reflection with interstellar clouds. This theory is called "Second order" Fermi acceleration[].

A.4.1 Second order Fermi acceleration

In the universe, interstellar clouds move randomly with the velocity of ~ 10 km/s. Interstellar clouds have larger magnetic field than interstellar gas. If cosmic rays which have relativistic velocities approach the interstellar clouds, they are reflected by a strong magnetic field. Here, we assume a particle which has relativistic velocity $\sim c$, mass m, and energy E_1, and an interstellar cloud which has velocity V and mass M ($M \gg m$) in a laboratory frame. In a rest frame of the interstellar cloud, the energy of the particle $E_1^{'}$ is calculated with the Lorentz factor $\gamma = 1/\sqrt{1-\beta^2}$ and $\beta = V/c$,

$$E_1^{'} = E_1 \gamma (1+\beta). \tag{A.48}$$

When the particle collides head-on with the cloud, the reflected particle have the same energy E_1. The energy in the laboratory frame is calculated by the Lorentz transformation.

$$E_2 = E_1^{'}\gamma(1+\beta) = E_1\gamma^2(1+\beta)^2 = E_1\frac{(1+\beta)^2}{1-\beta^2} \tag{A.49}$$

$$\frac{E_2}{E_1} = 1 + \frac{2\beta(\beta+1)}{1-\beta^2} \simeq 1 + 2\frac{V}{c} \qquad (\beta \ll 1). \tag{A.50}$$

In the case of rear-end collision, the above relation becomes

$$\frac{E_2}{E_1} \simeq 1 - 2\frac{V}{c}. \tag{A.51}$$

Because the collision frequencies of head-on and rear-end collisions are proportional to $c+V$ and $c-V$, respectively, the average energy increase is evaluated as

$$\Delta E = \frac{(c+V)2V/c + (c-V)(-2V/c)}{c+V+c-V} = 2\left(\frac{V}{c}\right)^2. \tag{A.52}$$

In three-dimensional case, ΔE becomes

$$\Delta E = \frac{4}{3}\left(\frac{V}{c}\right)^2, \tag{A.53}$$

and the energy obeys the following relation.

$$\frac{dE}{dt} = \frac{1}{t_{\rm col}}\frac{4}{3}\left(\frac{V}{c}\right)^2 E, \tag{A.54}$$

where $t_{\rm col} = l/(3c)$ is average collision time and l is the average distance between each interstellar clouds. Solving the equation, we obtain the energy with $t_{\rm col}$.

$$E = E_0 \exp\left(\frac{t}{t_{\rm acc}}\right), \tag{A.55}$$

$$t_{\rm acc} = \frac{3}{4}\left(\frac{c}{V}\right)^2 t_{\rm col}, \tag{A.56}$$

where E_0 is the initial particle energy. Using average escape time $t_{\rm esc}$ in which particles escape from the galaxy, the probability of particle escape and the energy spectrum can be obtained.

$$P(t) = \exp\left(-\frac{t}{t_{\rm esc}}\right) \tag{A.57}$$

$$\frac{dN}{dE} \propto \frac{dP/dt}{dE/dt} \tag{A.58}$$

$$\propto \exp\left(-\frac{t}{t_{\rm acc}} - \frac{t}{t_{\rm esc}}\right) \tag{A.59}$$

$$\propto E^{-1-t_{\rm acc}/t_{\rm esc}} \tag{A.60}$$

From observations, the energy spectrum is measured as $dN/dE \sim E^{-(2.0-2.2)}$. Therefore,

$$\frac{t_{\rm acc}}{t_{\rm esc}} \sim 1, \tag{A.61}$$

$$t_{\rm acc} \sim t_{\rm esc}. \tag{A.62}$$

Using typical values $V = 10^4$ m s^{-1} and $t_{\rm col} = 10^9$ s, $t_{\rm acc}$ is estimated as $t_{\rm acc} \sim 10^{17}$ s. This value is too long to accelerate particles in our galaxy.

A.4.2 First order Fermi acceleration

When a particle goes back and forth between the upstream and downstream of a collisionless shock, the particle can be accelerated due to the reflection by reflectors such as a magnetic fields which is moving with fluids. If a particle goes back and forth once through a shock surface, the energy increases $E_1 = E_0 + \Delta E$.

$$\frac{E_1}{E_0} = 1 + \frac{4}{3}\frac{V_1 - V_2}{c}, \tag{A.63}$$

where V_1 and V_2 are the flow velocities at the upstream and downstream of the shock. After n times of reflection, the energy E_n is written as

$$\frac{E_n}{E_0} = \left(1 + \frac{4}{3}\frac{V_1 - V_2}{c}\right)^n \simeq \exp\left(\frac{4n}{3}\frac{V_1 - V_2}{c}\right). \tag{A.64}$$

$$n \simeq \frac{3}{4}\frac{c}{V_1 - V_2}\ln\left(\frac{E_n}{E_0}\right) \tag{A.65}$$

The number of particles which escape from the shock surface is expressed as

$$n_{\rm esc} = nV_2. \tag{A.66}$$

On the other hand, the particles moving from the upstream to the downstream is written as

$$n_{\rm inc} = \int_0^{\pi/2} d\theta \int_0^{2\pi} d\phi \frac{nc}{4\pi}\cos\theta = \frac{nc}{4}. \tag{A.67}$$

Here, we use the particle velocity $v \simeq c$. Using equations (A.66) and (A.67), we obtain the probability that the particles escape from the shock region.

$$P_{\rm esc} = \frac{n_{\rm esc}}{n_{\rm inc}} = \frac{4V_2}{c} \tag{A.68}$$

As a result, the probability that particles survive after n-time reflections at the shock region is written using equation (A.68).

$$P_n = (1 - P_{\rm esc})^n = \left(1 - \frac{4V_2}{c}\right)^n \simeq \exp\left(-\frac{4V_2 n}{c}\right) \tag{A.69}$$

The energy spectrum $N(E)$ is derived using equations (A.65) and (A.69):

$$N(E > E_n) \propto P_n \simeq \exp\left[-\frac{3V_2}{V_1 - V_2}\ln\left(\frac{E_n}{E_0}\right)\right] = \left(\frac{E_n}{E_0}\right)^{-\frac{3V_2}{V_1 - V_2}} \tag{A.70}$$

$$\tag{A.71}$$

Therefore,

$$N(E) \propto E^{-\alpha} \tag{A.72}$$

$$\alpha = \frac{3V_2}{V_1 - V_2} + 1 = \frac{V_1/V_2 + 2}{V_1/V_2 - 1}. \tag{A.73}$$

From equation (A.8), the velocity ratio V_1/V_2 becomes 4 if the Mach-number of the shock is large. Substituting $V_1/V_2 = 4$ in equation (A.73), the power index becomes 2. In fact, the energy spectra observed in a lot of astronomical objects show like the power function of E^{-2}, and this first order Fermi acceleration is now the standard theory for particle acceleration in the universe.

Appendix B

Material dependence for shock formation

B.1 Laser experiment with different target materials

We performed collisionless shock experiment to study the dependence on the target materials. As reported by Kuramitsu *et al*., shocks were observed in counter-streaming CH plasmas in a same experimental setup as shown in Figure B.1[80]. In this chapter, we show the difference for shock formation between CH and Cu plasmas.

B.2 Experimental setup

Targets used are different from those shown in chapter 3 and chapter 5, however, the experimental setup is similar to that in chapter 5. Targets consists of two foils with thicknesses of 100–200 μm. To irradiate the inner surface of the foil, targets are tilted 30 degrees from incident laser axis as shown in Figure B.1. We used two types of targets: one is CH-CH double-foil, and the other is Cu-Cu double-foil target. In this section we show the results of the shock generation observed with the SOP in both targets. One beam of GXII HIPER

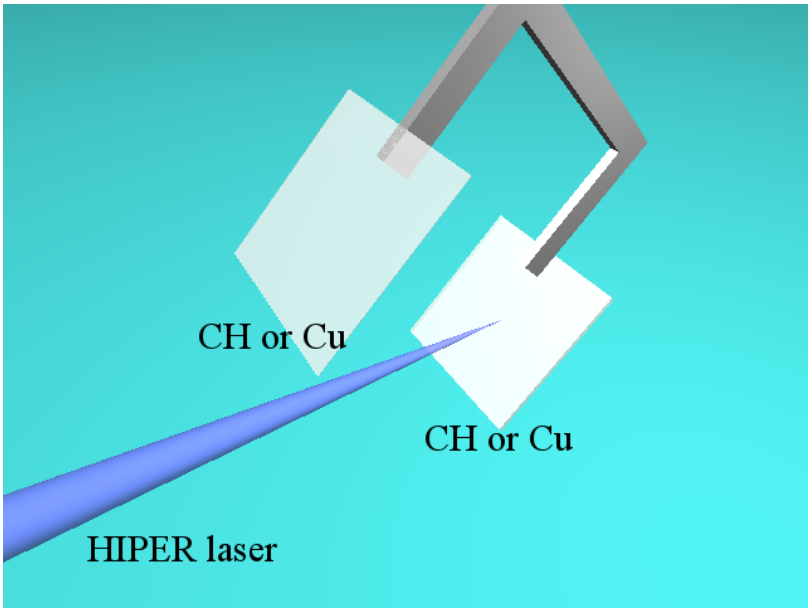

Figure B.1: Target design and the arrangement of laser beams. A laser beam is focused on the inner surface of the target.

laser systems is focused on the inner surface of the foil. Other laser conditions are almost the same as those in chapter 5.

B.3 Result and discussion

Figures B.2(a) and B.2(b) show the time evolution of self-emission from CH and Cu double-plane targets, respectively. The horizontal axis x is the distance from the left foil and the vertical axis t shows the time from the laser peak. The color levels show the digital output counts of the SOP. The laser beam is focused on the surface of the right-side foil at $x = 4.5$ mm, and the foil is ablated to produce a plasma (first plasma) which propagates from right to left. The left-side foil is also ablated by the radiation from the laser-produced first plasma, and the produced plasma (second plasma) propagates from left to right. The counter-streaming plasmas begin to interact with each other at t ∼15–20 ns, and a sharp brightness jump is observed.

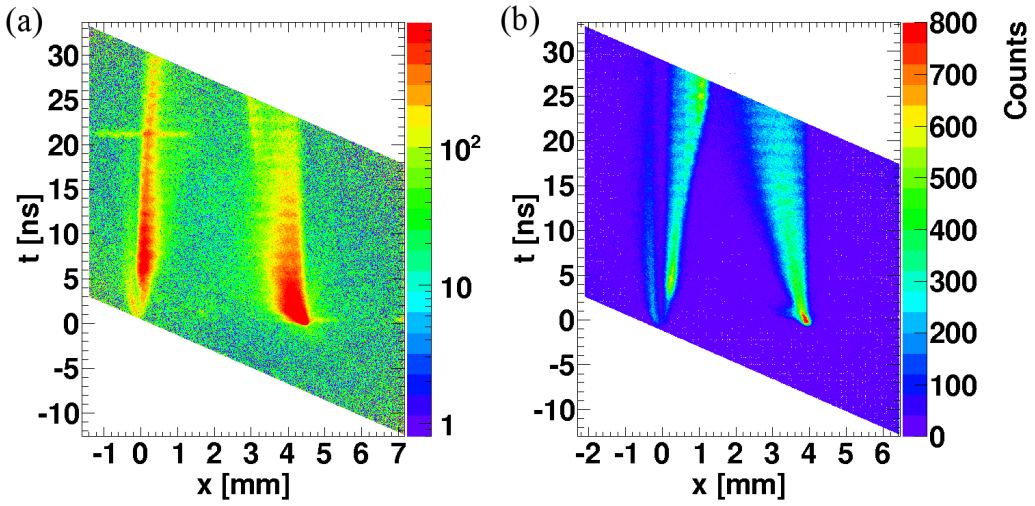

Figure B.2: Time evolution of the self-emission

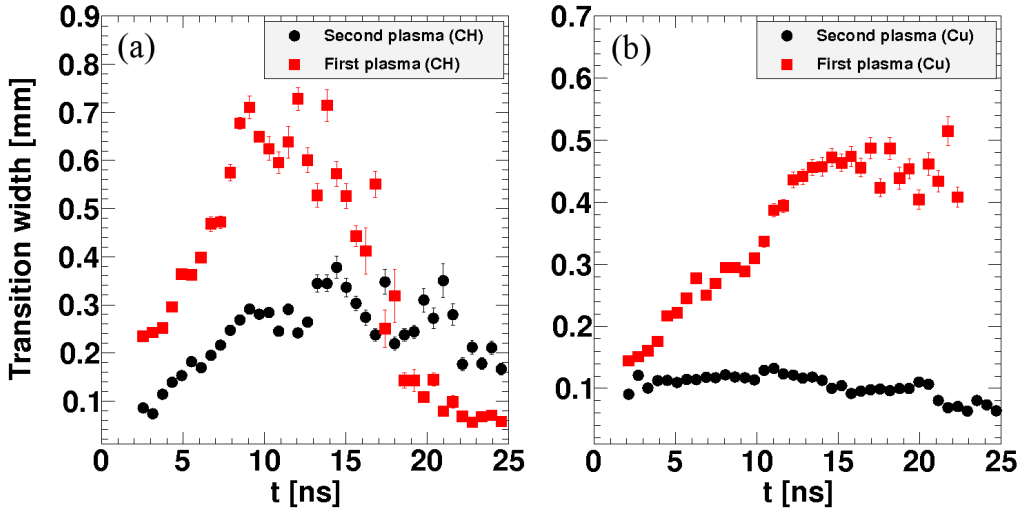

Figure B.3: Time evolution of the transition widths of the first plasma (red) and the second plasma (black) with the target materials of (a) CH and (b) Cu.

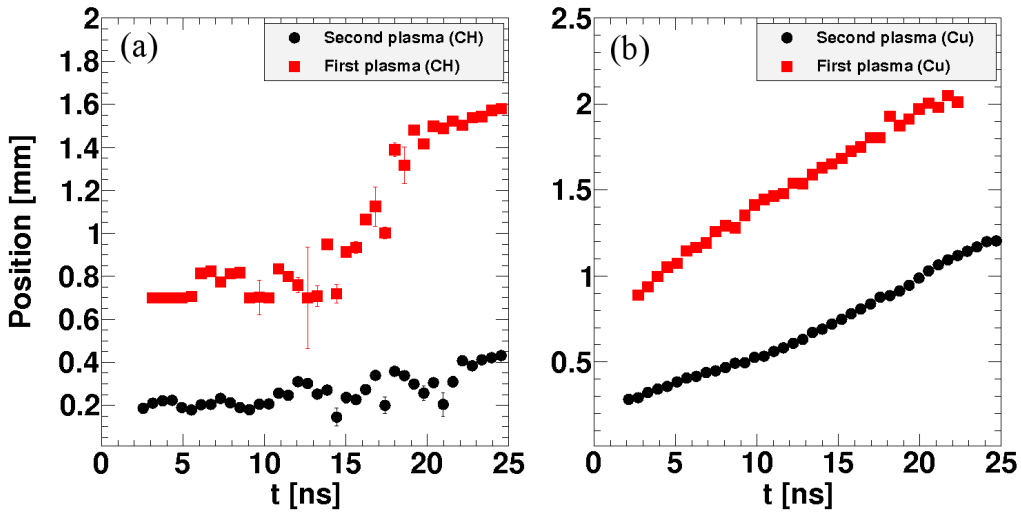

Figure B.4: Time evolution of the transition positions of first plasma (red) and second plasma (black) with the target materials of (a) CH and (b) Cu.

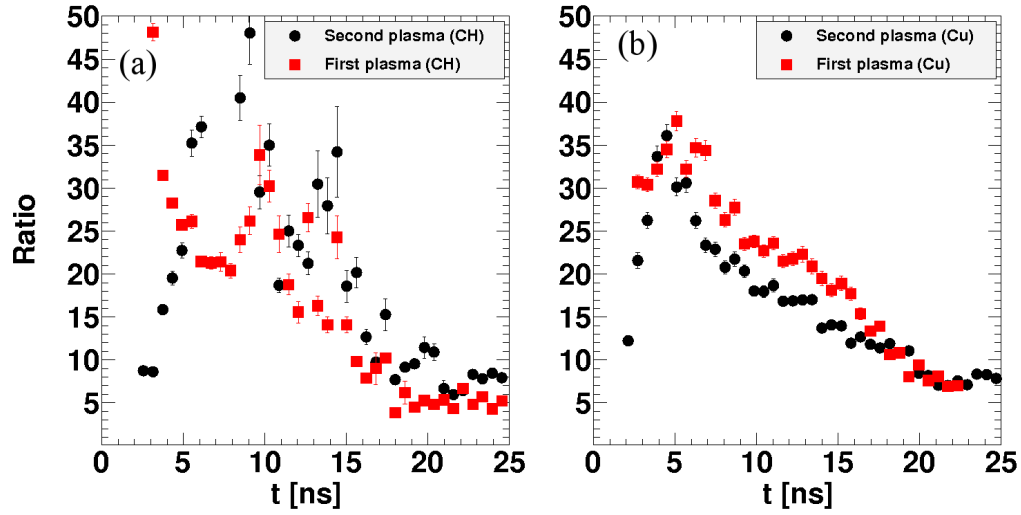

Figure B.5: Time evolution of the ratio of the downstream to upstream at the shock-like structure of first plasma (red) and second plasma (black) with the target materials of (a) CH and (b) Cu.

Figures B.3(a) and B.3(b) show the time evolution of the evaluated transition widths using equation (5.1) as argued in the chapter 5. In Fig. B.3(a), the transition width of the first plasma suddenly decreases at t =15–20 ns while that of the second plasma keeps increasing. This sudden decrease in the transition width is explained by the shock formation in counter-streaming plasmas. On the other hand, in Fig. B.3(b), the transition width of the second plasma propagates keeping sharp structure while that of the first plasma increases as time passes. It indicates that the shock is produced in front of the second plasma not of the first plasma.

Figures B.4(a) and B.4(b) show the time evolution of the distances between the transition point and the target surface. The velocity of the shock produced in CH plasmas is evaluated as $\sim$ 33 km/s from Fig. B.4(a) shown with square marks after $t = 20$ ns. On the other hand, if the generated structure in the second plasma of Cu is a shock, the shock velocity is evaluated from Fig. B.4(b) as $\sim$ 41 km/s.

Figures B.5(a) and B.5(b) show the brightness ratios of the higher region to lower region at the transition point. The ratio of the first plasma in CH decreases from $t = 5$ ns to 20 ns as shown with square marks in Fig. B.5(a), and after shock formation, the ratio takes a constant value ~ 5. The ratio of the first plasma in Cu also decreases from $t = 5$ ns to 20 ns as shown with circle marks in Fig. B.5(b), however, the value ~ 8 after 20 ns is relatively larger than that in CH plasma.

The brightness ratio of the downstream to upstream region is expressed as equation (B.1) as argued in the chapter 5. If the degrees of ionization is not constant, however, the formula becomes

$$\frac{\epsilon_{\lambda 1}}{\epsilon_{\lambda 0}} = \left(\frac{n_1}{n_0}\right)^2 \left(\frac{Z_1}{Z_0}\right) \left(\frac{T_1}{T_0}\right)^{-1/2} \left(\frac{g_1^{ff}}{g_0^{ff}}\right) \exp\left[-\frac{hc}{\lambda T_0}\left(\left(\frac{T_1}{T_0}\right)^{-1} - 1\right)\right], \qquad \text{(B.1)}$$

where Z_0 and Z_1 are the degrees of ionization at the upstream and downstream regions, respectively. The difference in the ratios between CH and Cu may be attributed to the

density ratio n_1/n_0 or Z ratio Z_1/Z_0 because the temperature (T) dependence of equation (B.1) is small compared with n or Z. If the density ratio in Cu plasma is larger then CH, the Mach-number of the shock in Cu is larger than that of the shock in CH. On the other hand, if Z ratio in Cu is larger than CH, the Cu plasma may be ionized in the downstream region due to the compression by the generated shock. It is difficult to conclude that the difference between CH and Cu plasmas comes from the above reasons, therefore, the precise density measurements in the downstream and upstream regions are needed.

Appendix C

NIF experiment for "Weibel-mediated" shock generation

C.1 Introduction

The objective of this experiment is to demonstrate the formation of high Mach-number collisionless shocks without an external magnetic field, and to prove that collisionless shocks are universally produced through the formation of self-generated magnetic fields due to nonlinearity in the growth of the Weibel instability. This can be direct evidence for the formation of collisionless shocks observed in the universe such as in supernova remnants (SNRs), and bow shocks produced by protostellar jets and cosmological jets. National Ignition Facility (NIF) is the only laser system in the world that can produce large-scale, high-velocity, and long-duration ablating plasmas to allow sufficient time for the formation of a collisionless shock, based on the scaling laws derived from simulations[32]. If we can observe, at the same time, a power-law spectrum of accelerated electrons and protons, this would be the first experimental evidence for the origin of cosmic rays by collisionless shocks.

Recently, a new theory has been proposed that suggests a very strong electrostatic (ES)

shock (that is, a shock that does not generate a magnetic field) can be generated, when counter-streaming plasma flows with different temperatures and densities interact with each other[30].

But an ES shock wave cannot accelerate charged particles up to extremely high energies. We have to demonstrate experimentally Weibel-mediated shock waves, which are more consistent with particle acceleration physics. Scaling laws[32] indicate that a NIF-class huge laser is necessary to demonstrate the formation of such collisionless shocks.

The objective of this experiment is to study collisionless shocks mediated by the self-organization of Weibel instability in counter-streaming plasmas produced by the NIF laser system. In the laboratory, we can measure the electromagnetic field directly by monoenergetic protons produced by (D, ^{3}He) implosions. Hence, laboratory astrophysics experiments on high-power lasers can be of great benefit towards furthering our understanding of astrophysical phenomena.

C.2 NIF laser facility

NIF is the world's largest and highest-energy laser system which aims to conduct laser fusion ignition experiments focusing 192 beams on a small target filled with tritium-deuterium fuel. NIF can provide up to the energy of 1.8 MJ with 192 beams with the wave length of 3ω (351 nm), which is about 1000 times larger than the energy that can be generated with Shenguang-II and Gekko GXII laser system. Such high-energy laser beams generate extreme plasma temperatures and pressures, and they enable us to study high-energy-density plasma physics. We will perform the collisionless shock experiment with NIF to produce high-density, high-velocity, large-scale, and long-duration plasmas. High-speed and high-density counter-streaming plasmas can generate Weibel-instabilities and they develop to produce a shock wave. In high-speed plasmas, counter-streaming plasmas are collisionless, and the produced shock wave is a collisionless shock.

C.3 Target design

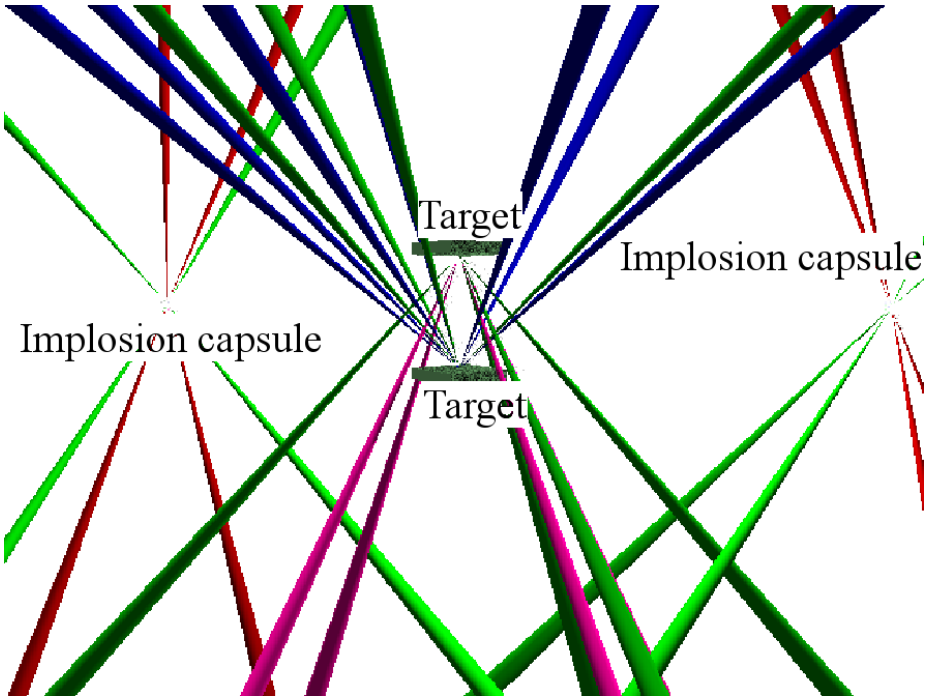

Figure C.1: Double-foil target and implosion capsules. The inner surfaces of the foils are irradiated to create counter-streaming plasmas. The capsules are irradiated to produce protons by (D, ^{3}He) implosions.

Double-plane targets with a separation of 10 mm are to be used in NIF experiments. Two implosion capsules are located near the target to generate protons from (D, ^{3}He) implosions. In the first stage of this experiment, we use plastic (CH) target. The thickness of CH plane is simulated by one-dimensional simulation ILESTA in various laser intensities. Figures C.2(a), C.2(b), and C.2(c) show the density profiles in various timings with the laser spot diameters of 1 mm, 600 μm, and 250 μm, respectively, with the energy of 384 kJ (64×6 kJ/beam) and the pulse width of 10 ns. The wavelength of the laser is 3ω (351 nm) and the critical density is $n_c = 9.0 \times 10^{21}$ cm^{-3}. In three results, the electron densities are lower than critical density, and are higher than 10^{21} cm^{-3} at the regions a few mm apart from target surfaces until $t = 20$ ns. Lower densities than the critical density are required

for laser absorption at the critical surfaces, and higher densities are required for shorter shock width.

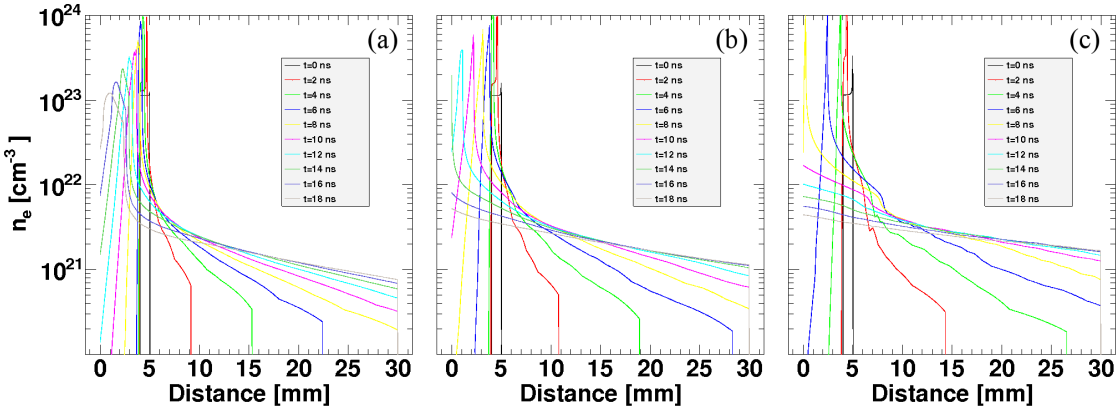

Figure C.2: Electron densities obtained by one-dimensional simulation "ILESTA" in a laser spot size of (a) 1 mm, (b) 600 μm, and (c) 250 μm. The target surface is at $x = 5$ mm.

Figure C.3(a)–C.3(f) show the time evolutions of the electron density, degree of ionization, ion velocity, electron temperature, ion temperature, and evaluated mean-free-path (black line) and expected shock width $\sim 100c/\omega_{\rm pi}$ (red line) in the case of the spot size of 250μm at $x = 10$ mm (5 mm fron the target surfaces) as shown in Fig. C.2. The electron density is larger than 1×10^{21} cm^{-3} and the ion velocity is larger than 1000 km/s until $t = 20$ ns. These conditions are appropriate for detection of shock structures. The expected shock width $\sim 100c/\omega_{\rm pi}$ is shorter than ion-ion mean-free-path as shown in Fig. C.3(f). The shock generated in such conditions represents a collisionless shock.

C.4 Experimental setup

Figure C.1 shows a schematic view of the experimental setup. By irradiating the inner-surfaces of a double-foil target (3 mm $\times$ 3 mm $\times$ 1 mm thick) with a separation of $L = 10$ mm using NIF beams, supersonic counter-streaming plasmas will be created. Choosing a low Z material for the target, we can create counter-streaming plasmas with the velocity of

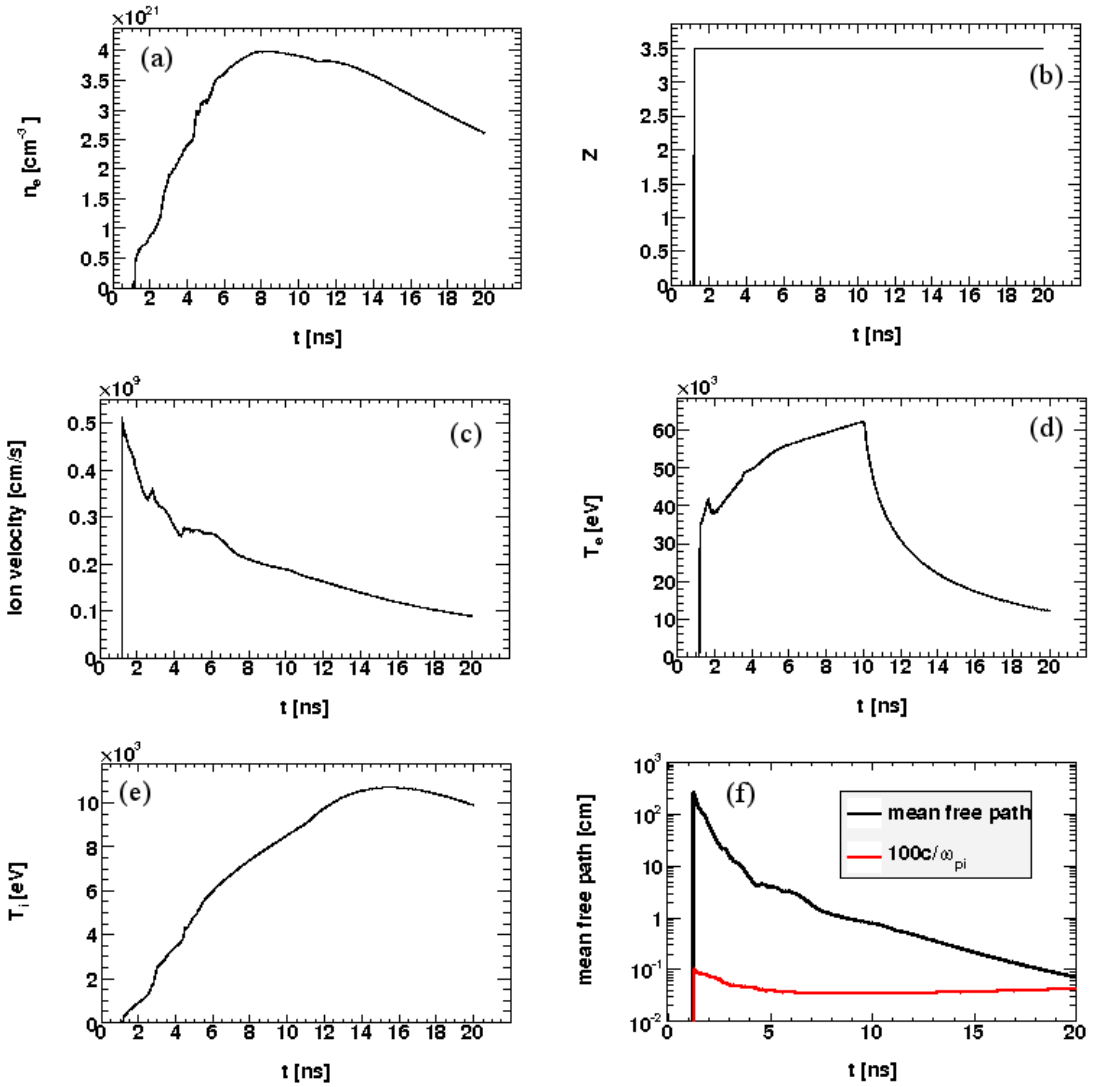

Figure C.3: The time evolution of (a) electron density, (b) the degree of ionization, (c) ion velocity, (d) electron temperature, (e) ion temperature, and (f) evaluated mean–free–path and expected shock width.

each plasma $\sim$ 1000 km/s or more, and with an ion–ion mean–free–path of order several centiimeters, which is much larger than the system size of our experiment. We use three kinds of double-foil targets with low Z materials, as follows;

1. CH–CD or CD–CD

2. LiH–LiD or LiD–LiD

3. Cryo-H_2–Cryo-D_2 or Cryo-D_2–Cryo–D_2

We emphasize that by design, when the plasmas interpenetrate, the coulomb collision mean–free–path is several cm, ie significantly larger than the size of the entire experimental system. In the absence of a collisionless shock, the two plasmas should just interpenetrate without interacting. For the first targets (CH - CD or CD - CD), the collisionality between counter-streaming plasma flows can be evaluated by observing the interaction of the two flows and the resultant neutron production due to D-D reactions. If the neutrons are produced at the time the two plasmas start to interpenetrate, this would be evidence of the formation of a collisionless shock. On the other hand, if neutrons are not observed until the plasma flow impacts the foil target at the opposite side, then no collisionless shock was formed. Alternatively, the two foils could be oriented so that the interpenetrating plasma flows are perpendicular to each other, in which case no neutrons would be observed at any time unless a collisionless shock were created, since the flows would not impact a foil on the side opposite it. The second and third targets have advantages for creation of collisionless flows because of the lower–Z material. In our previous experiments, we already have obtained suggestive results in collisionless shock formation with CH double-foil targets, and hence CH–CD or CD–CD targets should be the first step in this NIF experiment.

The time evolution of the counter-streaming collisionless plasmas and the formation properties of Weibel-mediated shock waves will be observed by visible self-emission and probe measurements (interferometry, shadowgraphy, polarimetry, and proton radiography).

Features of interest are the growth from small electron current filaments to larger filaments by coalescence, formation of self-generated magnetic fields, and steady-state shock wave generation, we will also obtain the plasma velocities and the effective temperature from self-emission and the interferometry using both visible streak cameras and fast-gate ICCD cameras. The following parameters will be measured in the experiment.

1. The temporal evolution of the plasma flows and the shock formation will be observed from visible self-emission using SOP and GOI, and from x-ray self-emission using a x-ray streak camera and x-ray framing camera in the direction transverse to the plasma flows.

2. Plasma density and density gradient can be measured by Nomarski interferometry and shadowgraphy or Schlieren method using a 4ω probe in the transverse direction. We can obtain the electron density up to ne $\sim 1.6 \times 10^{22}$ cm^{-3}, which corresponds to the critical density for the 4ω laser.

3. Self-generated magnetic fields can be measured with proton radiography[81] or polarimetry [82, 83]. Several D-^{3}He implosions (with $\sim$50 kJ / implosion) can be used to create monoenegetic proton sources with various delay and different line of sight as shown in Fig. C.1. In general, protons can be deflected by electric and magnetic fields, and we will obtain the proton image including both effects. Faraday rotation can also be used to measure the magnetic field in laser-produced plasmas. In this case, the variation of polarization angle depends on the plasma density and magnetic field. Combining with the density profile obtained by interferometry, the distribution of magnetic field can be calculated.

4. Electron temperatures ($T_{\rm e}$) can be obtained by Thomson scattering using a 4ω probe and time-resolved extreme-ultraviolet (EUV) or soft x-ray spectrograph. Temporal evolution of the radiation temperature will be measured using a visible spectrometer

and a streak camera in the transverse direction.

5. High-energy electrons and resultant emissions are detected by an electron spectrometer and the time-resolved Filter Fluorescer (FFLEX) Spectrometer, respectively. High-energy ions accelerated by a collisionless shock will be measured by a Thomson parabola.

List of Figures

Acknowledgments

I would like to express my thanks to my adviser, Prof. Hideaki Takabe for the realization of international experiments with large-scale laser systems and dedicated guidance in the past three years. I would like to express my gratitude to Associate Prof. Youichi Sakawa for his continuous encouragement and valuable discussions, comments, and advices. I also thank to Dr. Yasuhiro Kuramitsu and Tsunehiko Kato for many useful discussions. I would like to acknowledge Prof. Hiroshi Azechi, the director of the Institute of Laser Engineering (ILE), and Prof. Kunioki Mima, the former director of ILE for the encouragements of this study.

I would like to thank Prof. Hiroshi Tsunemi, Prof. Hiroshi Shibai, and Associate Prof. Yutaka Fujita for their useful comments on the thesis.

I acknowledge Dr. Jie Zhang, Dr. Yutong Li, Dr. Quanli Dong, Shoujun Wang, and technical staffs at Shenguang-II laser facility for the collaborations and the realization of the experiment in Shanghai, China.

I acknowledge Dr. Nigel Woolsey, Dr. Christpher Gregory, and Jonathan Waugh for their helpful discussions and collaborations, and I also thank technical engineers in Rutherford Appleton Laboratory for the preparation of grateful laser shots.

I would like to thank Dr. Michael Koenig, Dr. Bérénice Loupias, Dr. Alessandra Ravasio, Alexandra Diziere, and technical engineers for the collaboration and realization of the experiment with LULI2000 laser system.

I would like to thank Seiichi Dono, Hidenori Aoki, Hiroki Tanji, Takao Ide, Kento Nishio, Associate Prof. Naofumi Onishi, and Dr. Akira Mizuta for their help for the analysis and various discussions. I appreciate Associate Prof. Keisuke Shigemori, Assistant Prof. Norimasa Ozaki, Assistant Prof. Takayoshi Sano, Assistant Prof. Shinsuke Fujioka, Tomoaki Kimura, Akinori Nishida, Kohei Miyanishi, and Akiyuki Shiroshita for their collaborations and discussions about experimental data and diagnostic systems. I also thank Prof. Takayoshi Norimatsu, Assistant Prof. Hirofumi Homma and target fabrication group and technical staffs at ILE for grateful laser shots.

At last, I would like to express my appreciation to my family. I have been able to concentrate on the study for three years with their help and support.

Bibliography

[1] K. Asakimori, T. H. Burnett, M. L. Cherry, K. Chevli, M. J. Christ, S. Dake, J. H. Derrickson, W. F. Fountain, M. Fuki, J. C. Gregory, T. Hayashi, R. Holynski, J. Iwai, A. Iyono, J. Johnson, M. Kobayashi, J. Lord, O. Miyamura, K. H. Moon, B. S. Nilsen, H. Oda, T. Ogata, E. D. Olson, T. A. Parnell, F. E. Roberts, K. Sengupta, T. Shiina, S. C. Strausz, T. Sugitate, Y. Takahashi, T. Tominaga, J. W. Watts, J. P. Wefel, B. Wilczynska, H. Wilczynski, R. J. Wilkes, W. Wolter, H. Yokomi, and E. Zager. Cosmic-ray proton and helium spectra: Results from the jacee experiment. *The Astrophysical Journal*, 502(1):278, 1998.

[2] E. S. Seo, H. S. Ahn, J. J. Beatty, S. Coutu, M. J. Choi, M. A. DuVernois, O. Ganel, T. G. Kang, K. C. Kim, M. H. Lee, L. Lutz, P. S. Marrocchesi, S. Minnick, K. W. Min, S. Nutter, H. Park, I. H. Park, E. Schindhelm, R. Sina, S. Swordy, J. Wu, and J. Yang. Cosmic-ray energetics and mass (cream) balloon project. *Advances in Space Research*, 33(10):1777 – 1785, 2004. The Next Generation in Scientific Ballooning.

[3] E. T. Sarris, S. M. Krigmigis, T. Iijima, C. O. Bostrom, and T. P. Armstrong. Location of the source of magnetospheric energetic particle bursts by multispacecraft observations. *Geophys. Res. Lett.*, 3(8):437, 1976.

[4] T. Terasawa and A. Nishida. Simultaneous observations of relativistic electron bursts and neutral-line signatures in the magnetotail. *Planetary and Space Science*, 24(9):855 – 866, 1976.

[5] M A Lawrence, R J O Reid, and A A Watson. The cosmic ray energy spectrum above 4*10 17 ev as measured by the haverah park array. *Journal of Physics G: Nuclear and Particle Physics*, 17(5):733, 1991.

[6] S. Yoshida, N. Hayashida, K. Honda, M. Honda, S. Imaizumi, N. Inoue, K. Kadota, F. Kakimoto, K. Kamata, S. Kawaguchi, N. Kawasumi, Y. Matsubara, K. Murakami, M. Nagano, H. Ohoka, M. Teshima, I. Tsushima, and H. Yoshii. The cosmic ray energy spectrum above 3 鐓 1018 ev measured by the akeno giant air shower array. *Astroparticle Physics*, 3(2):105 – 123, 1995.

[7] D. J. Bird, H. Y. Dai, B. R. Dawson, J. W. Elbert, M. A. Huang, D. B. Kieda, S. Ko, E. C. Loh, M. Luo, J. D. Smith, P. Sokolsky, P. Sommers, and S. B. Thomas. Study of broad-scale anisotropy of cosmic-ray arrival directions from 2 x 1017 to 1020 electron volts from fly's eye data. *The Astrophysical Journal*, 511(2):739, 1999.

[8] James W. Cronin. Cosmic rays: the most energetic particles in the universe. *Rev. Mod. Phys.*, 71(2):S165–S172, Mar 1999.

[9] Kenneth Greisen. End to the cosmic-ray spectrum? *Phys. Rev. Lett.*, 16(17):748–750, Apr 1966.

[10] G. T. Zatsepin and V. A. Kuz'min. Upper limit of the spectrum of cosmic rays. *Journal of Experimental and Theoretical Physics Letters*, 4:78–80, 1966.

[11] L O'C Drury. An introduction to the theory of diffusive shock acceleration of energetic particles in tenuous plasmas. *Reports on Progress in Physics*, 46(8):973, 1983.

[12] S. Imada, M. Hoshino, and T. Mukai. Average profiles of energetic and thermal electrons in the magnetotail reconnection regions. *Geophys. Res. Lett.*, 32:L09101, 2005.

[13] E. Sarris, G. Anagnostopoulos, and S. Krimigis. Simultaneous measurements of energetic ion ($\geq$50 kev) and electron ($\geq$220 kev) activity upstream of earth's bow shock and inside the plasma sheet: Magnetospheric source for the november 3 and december 3, 1977 upstream events. *Journal of Geophysical Research*, 90(A1):12–18, 1985.

[14] K.-P. Wenzel, R. Reinhard, T. Sanderson, and E. Sarris. Characteristics of energetic particle events associated with interplanetary shocks. *Journal of Geophysical Research*, 90(A1):12–18, 1985.

[15] N. Shimada, T. Terasawa, M. Hoshino, T. Naito, H. Matsui, T. Koi, and K. Maezawa. Diffusive shock acceleration of electrons at an interplanetary shock observed on 21 feb 1994. *Astrophysics and Space Science*, 264:481–488, 1998. 10.1023/A:1002499513777.

[16] R. W. Klebesadel, I. B. Strong, and R. A. Olson. Observations of gamma-ray bursts of cosmic origin. *The Astrophysical Journal*, 182:L85–L88, 1973.

[17] D. H. Clark and F. R. Stephenson. *The Historical Supernovae*. Pergamon press, Oxford, 1977.

[18] Frederick D. Seward and Philip A. Charles. *Exploring the X-ray Universe*. Cambridge University Press, second edition, 2010.

[19] K. Hirata, T. Kajita, M. Koshiba, M. Nakahata, Y. Oyama, N. Sato, A. Suzuki, M. Takita, Y. Totsuka, T. Kifune, T. Suda, K. Takahashi, T. Tanimori, K. Miyano, M. Yamada, E. W. Beier, L. R. Feldscher, S. B. Kim, A. K. Mann, F. M. Newcomer, R. Van, W. Zhang, and B. G. Cortez. Observation of a neutrino burst from the supernova sn1987a. *Phys. Rev. Lett.*, 58(14):1490–1493, Apr 1987.

[20] R. M. Bionta, G. Blewitt, C. B. Bratton, D. Casper, A. Ciocio, R. Claus, B. Cortez, M. Crouch, S. T. Dye, S. Errede, G. W. Foster, W. Gajewski, K. S. Ganezer, M. Goldhaber, T. J. Haines, T. W. Jones, D. Kielczewska, W. R. Kropp, J. G. Learned, J. M.

LoSecco, J. Matthews, R. Miller, M. S. Mudan, H. S. Park, L. R. Price, F. Reines, J. Schultz, S. Seidel, E. Shumard, D. Sinclair, H. W. Sobel, J. L. Stone, L. R. Sulak, R. Svoboda, G. Thornton, J. C. van der Velde, and C. Wuest. Observation of a neutrino burst in coincidence with supernova 1987a in the large magellanic cloud. *Phys. Rev. Lett.*, 58(14):1494–1496, Apr 1987.

[21] Alekseev E. N., Alekseeva L. N., Volchenko V. I., and Krivosheina I. V. Possible detection of a neutrino signal on 23 february 1987 at the baksan underground scintillation telescope of the institute of nuclear research. *JETP Lett.*, 45:589, 1987.

[22] R. A. Chevalier. Self-similar solutions for the interaction of stellar ejecta with an external medium. *The Astrophysical Journal*, 258:790–797, July 1982.

[23] Aya Bamba, Ryo Yamazaki, Masaru Ueno, and Katsuji Koyama. Small-scale structure of the sn 1006 shock with chandra observations. *The Astrophysical Journal*, 589(2):827, 2003.

[24] R. Rothenflug, J. Ballet, G. Dubner, E. Giacani, A. Decourchelle, and P. Ferrando. Geometry of the non-thermal emission in sn 1006. *A&A*, 425(1):121–131, 2004.

[25] Stephan Rosswog and Marcus Brueggen. *Introduction to High-Energy Astrophysics*. Cambridge University Press, 2007.

[26] Yasunobu Uchiyama, Felix A. Aharonian, Takaaki Tanaka, Tadayuki Takahashi, and Yoshitomo Maeda. Extremely fast acceleration of cosmic rays in a supernova remnant. *Nature*, 449(7162):576–578, Oct 2007.

[27] F. A. Aharonian, A. G. Akhperjanian, K.-M. Aye, A. R. Bazer-Bachi, M. Beilicke, W. Benbow, D. Berge, P. Berghaus, K. Bernlohr, O. Bolz, C. Boisson, C. Borgmeier, F. Breitling, A. M. Brown, J. Bussons Gordo, P. M. Chadwick, V. R. Chitnis, L.-M. Chounet, R. Cornils, L. Costamante, B. Degrange, A. Djannati-Atai, L. O. '. C. Drury, T. Ergin, P. Espigat, F. Feinstein, P. Fleury, G. Fontaine, S. Funk, Y. A. Gallant, B. Giebels, S. Gillessen, P. Goret, J. Guy, C. Hadjichristidis, M. Hauser, G. Heinzelmann, G. Henri, G. Hermann, J. A. Hinton, W. Hofmann, M. Holleran, D. Horns, O. C. de Jager, I. Jung, B. Khelifi, Nu Komin, A. Konopelko, I. J. Latham, R. Le Gallou, M. Lemoine, A. Lemiere, N. Leroy, T. Lohse, A. Marcowith, C. Masterson, T. J. L. McComb, M. de Naurois, S. J. Nolan, A. Noutsos, K. J. Orford, J. L. Osborne, M. Ouchrif, M. Panter, G. Pelletier, S. Pita, M. Pohl, G. Puhlhofer, M. Punch, B. C. Raubenheimer, M. Raue, J. Raux, S. M. Rayner, I. Redondo, A. Reimer, O. Reimer, J. Ripken, M. Rivoal, L. Rob, L. Rolland, G. Rowell, V. Sahakian, L. Sauge, S. Schlenker, R. Schlickeiser, C. Schuster, U. Schwanke, M. Siewert, H. Sol, R. Steenkamp, C. Stegmann, J.-P. Tavernet, C. G. Theoret, M. Tluczykont, D. J. van der Walt, G. Vasileiadis, P. Vincent, B. Visser, H. J. Volk, and S. J. Wagner. High-energy particle acceleration in the shell of a supernova remnant. *Nature*, 432(7013):75–77, Nov 2004.

[28] Tsunehiko N. Kato and Hideaki Takabe. Relativistic collisionless shocks in unmagnetized electron-positron plasmas. *The Astrophysical Journal*, 668:974, 2007.

[29] Philip Chang, Anatoly Spitkovsky, and Jonathan Arons. Long-term evolution of magnetic turbulence in relativistic collisionless shocks: Electron-positron plasmas. *The Astrophysical Journal*, 674(1):378, 2008.

[30] Tsunehiko N. Kato and Hideaki Takabe. Nonrelativistic collisionless shocks in unmagnetized electron-ion plasmas. *The Astrophysical Journal Letters*, 681(2):L93, 2008.

[31] G. Sorasio, M. Marti, R. Fonseca, and L. O. Silva. Very high mach-number electrostatic shocks in collisionless plasmas. *Phys. Rev. Lett.*, 96(4):045005, Feb 2006.

[32] H Takabe, T N Kato, Y Sakawa, Y Kuramitsu, T Morita, T Kadono, K Shigemori, K Otani, H Nagatomo, T Norimatsu, S Dono, T Endo, K Miyanishi, T Kimura, A Shiroshita, N Ozaki, R Kodama, S Fujioka, H Nishimura, D Salzman, B Loupias, C Gregory, M Koenig, J N Waugh, N C Woolsey, D Kato, Y-T Li, Q-L Dong, S-J Wang, Y Zhang, J Zhao, F-L Wang, H-G Wei, J-R Shi, G Zhao, J-Y Zhang, T-S Wen, W-H Zhang, X Hu, S-Y Liu, Y K Ding, L Zhang, Y-J Tang, B-H Zhang, Z-J Zheng, Z-M Sheng, and J Zhang. High-mach number collisionless shock and photo-ionized non-lte plasma for laboratory astrophysics with intense lasers. *Plasma Physics and Controlled Fusion*, 50(12):124057, 2008.

[33] Erich S. Weibel. Spontaneously growing transverse waves in a plasma due to an anisotropic velocity distribution. *Phys. Rev. Lett.*, 2(3):83–84, Feb 1959.

[34] Tsunehiko N. Kato and Hideaki Takabe. Electrostatic and electromagnetic instabilities associated with electrostatic shocks: Two-dimensional particle-in-cell simulation. *Physics of Plasmas*, 17(3):032114, 2010.

[35] Bruce A. Remington, R. Paul Drake, and Dmitri D. Ryutov. Experimental astrophysics with high power lasers and z pinches. *Rev. Mod. Phys.*, 78(3):755–807, Aug 2006.

[36] A. J. Mackinnon, P. K. Patel, R. P. Town, M. J. Edwards, T. Phillips, S. C. Lerner, D. W. Price, D. Hicks, M. H. Key, S. Hatchett, S. C. Wilks, M. Borghesi, L. Romagnani, S. Kar, T. Toncian, G. Pretzler, O. Willi, M. Koenig, E. Martinolli, S. Lepape, A. Benuzzi-Mounaix, P. Audebert, J. C. Gauthier, J. King, R. Snavely, R. R. Freeman, and T. Boehlly. Proton radiography as an electromagnetic field and density perturbation diagnostic (invited). *Review of Scientific Instruments*, 75(10):3531–3536, 2004.

[37] D. A. Tidman. Turbulent shock waves in plasmas. *Physics of Fluids*, 10(3):547–564, 1967.

[38] D. W. Forslund and C. R. Shonk. Formation and structure of electrostatic collisionless shocks. *Phys. Rev. Lett.*, 25(25):1699–1702, Dec 1970.

[39] P. H. Sakanaka, C. K. Chu, and T. C. Marshall. Formation of ion-acoustic collisionless shocks. *Physics of Fluids*, 14(3):611–614, 1971.

[40] B. Lembege and J. M. Dawson. Formation of double layers within an oblique collisionless shock. *Phys. Rev. Lett.*, 62(23):2683–2686, Jun 1989.

[41] J. Denavit. Absorption of high-intensity subpicosecond lasers on solid density targets. *Phys. Rev. Lett.*, 69(21):3052–3055, Nov 1992.

[42] Luís O. Silva, Michael Marti, Jonathan R. Davies, Ricardo A. Fonseca, Chuang Ren, Frank S. Tsung, and Warren B. Mori. Proton shock acceleration in laser-plasma interactions. *Phys. Rev. Lett.*, 92(1):015002, Jan 2004.

[43] Min Chen, Zheng-Ming Sheng, Quan-Li Dong, Min-Qing He, Yu-Tong Li, Muhammad Abbas Bari, and Jie Zhang. Collisionless electrostatic shock generation and ion acceleration by ultraintense laser pulses in overdense plasmas. *Physics of Plasmas*, 14(5):053102, 2007.

[44] R. J. Taylor, D. R. Baker, and H. Ikezi. Observation of collisionless electrostatic shocks. *Phys. Rev. Lett.*, 24(5):206–209, Feb 1970.

[45] H. Ikezi, T. Kamimura, M. Kako, and K. E. Lonngren. Laminar electrostatic shock waves generated by an ion beam. *Physics of Fluids*, 16(12):2167–2175, 1973.

[46] H. Ikezi, K. Mima, Kyoji Nishikawa, and Masaaki Inutake. Shock waves generated by an oscillating electric field in an expanding plasma. *Phys. Rev. Lett.*, 36(14):794–797, Apr 1976.

[47] R. J. Taylor, K. R. MacKenzie, and H. Ikezi. A large double plasma device for plasma beam and wave studies. *Review of Scientific Instruments*, 43(11):1675–1678, 1972.

[48] A. R. Bell, P. Choi, A. E. Dangor, O. Willi, D. A. Bassett, and C. J. Hooker. Collisionless shock in a laser-produced ablating plasma. *Phys. Rev. A*, 38(3):1363–1369, Aug 1988.

[49] C. Courtois, R. A. D. Grundy, A. D. Ash, D. M. Chambers, N. C. Woolsey, R. O. Dendy, , and K. G. McClements. Experiment on collisionless plasma interaction with applications to supernova remnant physics. *Phys. Plasmas*, 11(7):3386, May 2004.

[50] L. Romagnani, S. V. Bulanov, M. Borghesi, P. Audebert, J. C. Gauthier, K. Löwenbrück, A. J. Mackinnon, P. Patel, G. Pretzler, T. Toncian, and O. Willi. Observation of collisionless shocks in laser-plasma experiments. *Phys. Rev. Lett.*, 101(2):025004, Jul 2008.

[51] N C Woolsey, C Courtois, and R O Dendy. Laboratory plasma astrophysics simulation experiments using lasers. *Plasma Physics and Controlled Fusion*, 46(12B):B397, 2004.

[52] P. M. Nilson, S. P. D. Mangles, L. Willingale, M. C. Kaluza, A. G. R. Thomas, M. Tatarakis, Z. Najmudin, R. J. Clarke, K. L. Lancaster, S. Karsch, J. Schreiber, R. G. Evans, A. E. Dangor, and K. Krushelnick. Generation of ultrahigh-velocity ionizing shocks with petawatt-class laser pulses. *Phys. Rev. Lett.*, 103(25):255001, Dec 2009.

[53] N. Izumi, Y. Sentoku, H. Habara, K. Takahashi, F. Ohtani, T. Sonomoto, R. Kodama, T. Norimatsu, H. Fujita, Y. Kitagawa, K. Mima, K. A. Tanaka, and T. Yamanaka. Observation of neutron spectrum produced by fast deuterons via ultraintense laser plasma interactions. *Phys. Rev. E*, 65(3):036413, Mar 2002.

[54] M. S. Wei, S. P. D. Mangles, Z. Najmudin, B. Walton, A. Gopal, M. Tatarakis, A. E. Dangor, E. L. Clark, R. G. Evans, S. Fritzler, R. J. Clarke, C. Hernandez-Gomez, D. Neely, W. Mori, M. Tzoufras, and K. Krushelnick. Ion acceleration by collisionless shocks in high-intensity-laser–underdense-plasma interaction. *Phys. Rev. Lett.*, 93(15):155003, Oct 2004.

[55] H. Habara, K. L. Lancaster, S. Karsch, C. D. Murphy, P. A. Norreys, R. G. Evans, M. Borghesi, L. Romagnani, M. Zepf, T. Norimatsu, Y. Toyama, R. Kodama, J. A. King, R. Snavely, K. Akli, B. Zhang, R. Freeman, S. Hatchett, A. J. MacKinnon, P. Patel, M. H. Key, C. Stoeckl, R. B. Stephens, R. A. Fonseca, and L. O. Silva. Ion acceleration from the shock front induced by hole boring in ultraintense laser-plasma interactions. *Phys. Rev. E*, 70(4):046414, Oct 2004.

[56] Moshe Deutsch and Israel Beniaminy. Derivative-free inversion of abel's integral equation. *Applied Physics Letters*, 41(1):27–28, July 1982.

[57] K. Bockasten. Transformation of observed radiances into radial distribution of the emission of a plasma. *J. Opt. Soc. Am.*, 51:943, 1961.

[58] R Illingworth and R K Thareja. Generaiised coefficients for abel inversion. *Journal of Physics E: Scientific Instruments*, 14(2):147, 1981.

[59] George B. Rybicki and Alan P. Lightman. *Radiative Processes in Astrophysics*. Wiley InterScience, 1985. ISBN-10: 0471827592 ISBN-13: 978-0471827597.

[60] G. S. Settles. *Schlieren and Shadowgraph Techniques: Visualizing Phenomena in Transport Media*. Springer, New York, 2009.

[61] L. Spitzer. *Physics of Fully Ionized Gases*. Interscience, New York, second edition, 1962. ISBN-10: 0486449823 ISBN-13: 978-0486449821.

[62] H. Takabe, M. Yamanaka, K. Mima, C. Yamanaka, H. Azechi, N. Miyanaga, M. Nakatsuka, T. Jitsuno, T. Norimatsu, M. Takagi, H. Nishimura, M. Nakai, T. Yabe, T. Sasaki, K. Yoshida, K. Nishihara, Y. Kato, Y. Izawa, T. Yamanaka, and S. Nakai. Scalings of implosion experiments for high neutron yield. *Physics of Fluids*, 31(10):2884–2893, 1988.

[63] *Andor iStar DH734 specification*.

[64] R. J. Mason. Computer simulation of ion-acoustic shocks. ii. slug and piston problems. *Physics of Fluids*, 15(5):845–853, 1972.

[65] L. D. Landau and E. M. Lifshitz. *Fluid Mechanics*. Butterworth-Heinemann, Oxford, second edition, 1987.

[66] Ya. B. Zel'dovich and Yu. P. Raizer. *Physics of Shock Waves and High-Temperature Hydrodynamic Phenomena*. Academic Press, New York, 1966.

[67] Y. Kuramitsu, Y. Sakawa, J. N. Waugh, C. D. Gregory, T. Morita, S. Dono, H. Aoki, H. Tanji, B. Loupias, M. Koenig, N. Woolsey, and H. Takabe. Jet formation in counterstreaming collisionless plasmas. *The Astrophysical Journal Letters*, 707(2):L137, 2009.

[68] J. E. Miller, T. R. Boehly, A. Melchior, D. D. Meyerhofer, P. M. Celliers, J. H. Eggert, D. G. Hicks, C. M. Sorce, J. A. Oertel, and P. M. Emmel. Streaked optical pyrometer system for laser-driven shock-wave experiments on omega. *Rev. Sci. Instrum.*, 78(3):034903, March 2007.

[69] T Morita, Y Sakawa, Y Kuramitsu, S Dono, H Aoki, H Tanji, T Kato, Y T Li, Y Zhang, X Liu, J Y Zhong, N Woolsey, H Takabe, and J Zhang. Collisionless shock generation by a high-power laser. *Journal of Physics: Conference Series*, 244(4):042010, 2010.

[70] T. Morita, Y. Sakawa, Y. Kuramitsu, S. Dono, H. Aoki, H. Tanji, T. N. Kato, Y. T. Li, Y. Zhang, X. Liu, J. Y. Zhong, H. Takabe, and J. Zhang. Collisionless shock generation in high-speed counter-streaming plasma flows by a high-power laser. *Physics of Plasmas*, 17:122702, 2010.

[71] T. Morita, Y. Sakawa, Y. Kuramitsu, S. Dono, H. Aoki, H. Tanji, J. Waugh, C. Gregory, B. Loupias, M. Koenig, N. Woolsey, and H. Takabe. Collisionless shock formation accompanied by a jet in counter-streaming plasmas. *submitted to Phys. Plasmas*, 2010.

[72] T. A. Movsessian, T. Yu. Magakian, J. Bally, M. D. Smith, A. V. Moiseev, and S. N. Dodonov. Herbig-haro jets in 3d: the hl/xz tauri region. *A&A*, 470(2):605–614, 2007.

[73] J. M. Blondin, B. A. Fryxell, and A. Konigl. The structure and evolution of radiatively cooling jets. *The Astrophysical Journal*, 360:370–386, September 1990.

[74] K. Tsinganos, N. Vlahakis, S. Bogovalov, C. Sauty, E. Trussoni, and J.J.G. Lima. Collimation of astrophysical mhd outflows. *Astrophysics and Space Science*, 287:103–108, 2003. 10.1023/B:ASTR.0000006208.62633.d0.

[75] Akira Mizuta, Shoichi Yamada, and Hideaki Takabe. Propagation and dynamics of relativistic jets. *The Astrophysical Journal*, 606(2):804, 2004.

[76] T. Morita, Y. Sakawa, Y. Kuramitsu, H. Tanji, H. Aoki, T. Ide, S. Shibata, N. Onishi, C. Gregory, A. Diziere, J. Waugh, N. Woolsey, Y. Sano, A. Shiroshita, K. Shigemori, N. Ozaki, T. Kimura, K. Miyanishi, R. Kodama, M. Koenig, and H. Takabe. Temperature measurements of electrostatic shocks in laser-produced counter-streaming plasmas. *Astrophysics and Space Science, in press*, 2010.

[77] W. J. Karzas and R. Latter. Electron radiative transitions in a coulomb field. *The Astrophysical Journal Supplement Series*, 6:167, 1961.

[78] D. A. Tidman and N. A. Krall. *Shock Waves in Collisionless Plasmas*. Wiley-Interscience, New York, 1987.

[79] Francis F. Chen. *Introduction to Plasma Physics*. Plenum Press, New York, 1974.

[80] Y. Kuramitsu, Y. Sakawa, T. Morita, S. Dono, H. Aoki, H. Tanji, C. D. Gregory, M. Koenig, J. N. Waugh, N. Woolseyg, and H. Takabe. Time evolution of a collisionless shock in counterstreaming laser produced plasmas. *Phys. Rev. Lett.*, 2010 submitted.

[81] C. K. Li, F. H. Séguin, J. A. Frenje, M. Rosenberg, R. D. Petrasso, P. A. Amendt, J. A. Koch, O. L. Landen, H. S. Park, H. F. Robey, R. P. J. Town, A. Casner, F. Philippe, R. Betti, J. P. Knauer, D. D. Meyerhofer, C. A. Back, J. D. Kilkenny, and A. Nikroo. Charged-Particle Probing of X-ray-Driven Inertial-Fusion Implosions. 327(5970):1231–1235, 2010.

[82] J. A. Stamper and B. H. Ripin. Faraday-Rotation measurements of megagauss magnetic fields in Laser-Produced plasmas. *Physical Review Letters*, 34(3):138, January 1975.

[83] M. Borghesi, A. J. MacKinnon, L. Barringer, R. Gaillard, L. A. Gizzi, C. Meyer, O. Willi, A. Pukhov, and J. Meyer-ter-Vehn. Relativistic channeling of a picosecond laser pulse in a Near-Critical preformed plasma. *Physical Review Letters*, 78(5):879, February 1997.

Publication List

[1] H. Takabe, T. N. Kato, Y. Sakawa, Y. Kuramitsu, T Morita, T. Kadono, K. Shigemori, K. Otani, H. Nagatomo, T. Norimatsu, S. Dono, T. Endo, K. Miyanishi, T. Kimura, A. Shiroshita, N. Ozaki, R. Kodama, S. Fujioka, H. Nishimura, D. Salzman, B. Loupias, C. Gregory, M. Koenig, J. N. Waugh, N. C. Woolsey, D. Kato, Y.-T. Li, Q.-L. Dong, S.-J. Wang, Y. Zhang, J. Zhao, F.-L. Wang, H.-G. Wei, J.-R. Shi, G. Zhao, J.-Y. Zhang, T.-S. Wen, W.-H. Zhang, X. Hu, S.-Y. Liu, Y. K. Ding, L. Zhang, Y.-J. Tang, B.-H. Zhang, Z.-J. Zheng, Z.-M. Sheng, and J. Zhang. High-Mach number collisionless shock and photo-ionized non-LTE plasma for laboratory astrophysics with intense lasers. *Plasma Physics and Controlled Fusion*, 50(12):124057, 2008.

[2] T. Morita, Y. Sakawa, Y. Kuramitsu, S. Shibata, H. Tanji, H. Aoki, C. Gregory, J. Waugh, N. Woolsey, T. Sano, A. Shiroshita, K. Shigemori, N. Ozaki, T. Kimura, K. Miyanishi, R. Kodama, M. Koenig, and H. Takabe. Optical pyrometer system for shock experiment using a high-power laser. **高速度イメージングとフォトニクスに関する総合シンポジウム論文集**, page 82, 2009.

[3] Y. Kuramitsu, Y. Sakawa, J. N. Waugh, C. D. Gregory, T. Morita, S. Dono, H. Aoki, H. Tanji, B. Loupias, M. Koenig, N. Woolsey, and H. Takabe. Jet Formation in Counterstreaming Collisionless Plasmas. *The Astrophysical Journal Letters*, 707(2):L137, 2009.

[4] T. Morita, Y. Sakawa, Y. Kuramitsu, S. Dono, H. Aoki, H. Tanji, T. Kato, Y. T. Li, Y. Zhang, X. Liu, J. Y. Zhong, N. Woolsey, J. Zhang, and H. Takabe. Collisionless shock generation by high speed plasma

flow using high intensity laser "Shenguang-II". *Annual Progress Report 2008*, 7:95–97, 2009.

[5] Y. Kuramitsu, Y. Sakawa, T. Morita, H. Aoki, H. Tanji, S. Dono, J. N. Waugh, C. D. Gregory, M. Koenig, N. Woolsey, and H. Takabe. Laboratory experiment to study collisionless shock. *Journal of Physics: Conference Series*, 244(4):042008, 2010.

[6] T. Morita, Y. Sakawa, Y. Kuramitsu, S. Dono, H. Aoki, H. Tanji, T. Kato, Y. T. Li, Y. Zhang, X. Liu, J. Y. Zhong, N. Woolsey, H. Takabe, and J. Zhang. Collisionless shock generation by a high-power laser. *Journal of Physics: Conference Series*, 244(4):042010, 2010.

[7] T. Morita, Y. Sakawa, Y. Kuramitsu, S. Dono, H. Aoki, H. Tanji, T. N. Kato, Y. T. Li, Y. Zhang, X. Liu, J. Y. Zhong, H. Takabe, and J. Zhang. Collisionless shock generation in high-speed counter-streaming plasma flows by a high-power laser. *Physics of Plasmas*, 17:122702, 2010.

[8] T. Morita, Y. Sakawa, Y. Kuramitsu, H. Tanji, H. Aoki, T. Ide, S. Shibata, N. Onishi, C. Gregory, A. Diziere, J. Waugh, N. Woolsey, Y. Sano, A. Shiroshita, K. Shigemori, N. Ozaki, T. Kimura, K. Miyanishi, R. Kodama, M. Koenig, and H. Takabe. Temperature measurements of Electrostatic Shocks in laser-produced counter-streaming plasmas. *Astrophysics and Space Science, in press*, 2010.

[9] T. Morita, Y. Sakawa, Y. Kuramitsu, S. Dono, H. Aoki, H. Tanji, J. Waugh, C. Gregory, B. Loupias, M. Koenig, N. Woolsey, and H. Takabe. Collisionless shock formation accompanied by a jet in counter-streaming plasmas. *submitted to Physics of Plasmas*, 2010.

[10] 坂和洋一, 蔵満康浩, 森田太智, 加藤恒彦, and 高部英明. 高出力レーザーを用いた実験室宇宙物理実験 (小特集大型レーザー装置を用いた科学研究の新展開). **プラズマ・核融合学会誌**, 86:578, 2010.

[11] 坂和洋一, 蔵満康浩, 森田太智, 加藤恒彦, and 高部英明. 高強度レーザーを用いた宇宙物理実験 (宇宙科学におけるレーザー利用特集). **レーザー研究**, 39:5, 2011.